From Cell Lines to Pseudo-Islets:

Unraveling the Influence of Hormones on Growth and Fragmentation

By

Kaya Margareta Keutler

A DISSERTATION

Presented to the Department of Physiology & Pharmacology

and the Oregon Health & Science University

School of Medicine

in partial fulfillment of

the requirements for the degree of

Doctor of Philosophy

November 2025

For my daughters, Karoline and Ryoko

May this be your sign that you, too, can achieve anything in life.

Your dad and I will always have your back!

"Don't let anyone rob you of your imagination, your creativity, or your curiosity. It's your place in the world; it's your life. Go on and do all you can with it, and make it the life you want to live."

— Mae Jemison, Engineer, Physician, and Former NASA Astronaut

Table of Contents

Table of Figures

Table of Abbreviations

Abbreviation	Definition
15N-TA	15N-trace amine
3PL	three-parameter logistic
5-HT	serotonin
AADC	aromatic amino acid decarboxylase
ADRA2	α_2-adrenergic receptor
AUC	area under the curve
BD	Becton-Dickinson
BMI	body mass index
cAMP	cyclic adenosine monophosphate
CNS	central nervous system
CTRL	control
Cx36	connexin 36
CyTOF	mass cytometry
DAT	dopamine transporter
DBH	β-hydroxylase
DEX	dexmedetomidine

DMEM	dulbecco's modified eagle's medium
DMSO	dimethyl sulfoxide
DPBS	dulbecco's phosphate-buffered saline
DTZ	dithizone
EBSS	earle's balanced salt solution
EC	effective concentration
ECM	extracellular matrix
EDTA	trypsin-ethylenediaminetetraacetic acid
EIA	enzyme immunoassay
ELISA	enzyme-linked immunosorbent assay
EMBL	european molecular biology laboratory
Epac	exchange proteins directly activated by cAMP
EPPTB	N-(3-ethoxyphenyl)-4-pyrrolidin-1-yl-3-trifluoromethylbenzamide
ERK	extracellular signal-regulated kinase
ESI-MS	electrospray ionization
EtOH	ethanol
FACS	fluorescence-activated cell sorting
FGF21	fibroblast growth factor 21
FMO	fluorescence minus one

GCG	glucagon
GCGR	glucagon receptor
Gi-coupled	inhibitory G-protein coupled
GIPR	glucose-dependent insulinotropic polypeptide receptor
GIRK	G-protein gated inwardly rectifying potassium (channel)
GLP-1R	glucagon-like peptid-1 receptor
GPCR	G-protein-coupled receptor
GSIS	glucose stimulated insulin secretion
GTT	glucose tolerance tests
HbA1c/A1c	donor hemoglobin A1c
HEPES	4-(2-hydroxyethyl)-1-piperazineethanesulfonic acid
HGF	hepatocyte growth factor
hiPSC	human induced pluripotent stem cell
HOPE	human organ procurement and exchange
HRMS	high-resolution mass spectrometry
IDA	idazoxan
IEQ	islet equivalent
IIDP	integrated islet distribution program
INS	insulin

INS1	mouse insulinoma cells 1
IR	insulin receptor
ITT	insulin tolerance tests
ITT	insulin tolerance tests
iv/OGTT	intravenous and oral glucose tolerance tests
KGF	Keratinocyte Growth Factor
KI	knock-in/overexpression
KO	knockout
lacZ	β-galactosidase reporter
LC-MS/MS	tandem mass spectrometry
LUT	look up table
MAO	monoamine oxidase
MAPK	mitogen-activated protein kinase
MeOH	methanol
mGFP	monomeric green fluorescent protein
MIN6	mouse insulinoma cells 6
MOA-A	monoamine oxidase isoform A
MOA-B	monoamine oxidase isoform B
MS	mass spectrometry

MS1	mile sven 1
NnT	nicotinamide nucleotide transhydrogenase
O/N	overnight
OCT	octopamine
oGTT	oral glucose tolerance test
PAA	phenylacetic acid
PBS	phosphate buffered saline
PDX, NKX6.1+	β-cell-specific transcriptions factors
PEA	β-phenylethylamine
PFA	paraformaldehyde
PHE	phenylalanine
PI	propidium iodine
PI3K	phosphoinositide 3-kinase
PKA	protein kinase A
PM	plasma membrane
PP	pancreatic polypeptide-secreting
RA	retinoic acid
RIPA	radioimmunoprecipitation assay buffer
ROI	region of interest

RPMI	roswell park memorial institute
RT	room temperature
RT-PCR	reverse-transcription PCR
Sant-1	Smoothened Antagonist
SD	standadrd deviation
SEM	Standard Error or the Mean
SN	supernatant
SSC	side scatter
SST	somatostatin
SSTR2	SST receptor 2
SSTR5	SST receptor 5
Stbl2	strain of competent E. coli bacteria
SYN	synephrine
T_1AM	3-iodothyronamine
T1D	Type 1 Diabetes
T2D	Type 2 Diabetes
TA	trace amine
TAAR1-KO	TAAR1 knock out
TAARs	trace amine-associated receptors

TCA	trichloroacetic acid
TGLN	trillium gift of life network
TRYP	tryptamine
TYR	p-tyramine
VA	Veteran Affairs
VEGFR2	vascular endothelial growth factor receptor 2
VGCC	voltage-gated Ca2+ channels
WT	wild type

Acknowledgements

I know this is not usually done, but I'd like to acknowledge myself for making it this far. For working through the hard parts, for standing back up, although I kept falling. This is not just a piece of academic writing; this, to me, is a symbol of persistence and stubbornness to a great extent. I have thought of walking away many times, I've shed many tears, and I know, if the situation had been different, I probably would've quit altogether.

Quitting, however, was not an option because my work as a graduate student allowed my partner (Raphael Kirchgaessner) to work as a graduate student (thanks to our dependent visa). Our legal status and our day-to-day life depended on my being successful and working on my PhD. So, I kept going. We kept going. Every step I took, I did with Raphael having my back. Even more so when we became a family of three and eventually four. Every hour in the lab was an hour he spent solo parenting while also working on his PhD. I don't know where we took the strength from; I guess we were empowering each other (?). I'm thankful for the partner you are, for the dad you are, for the science colleague you are! This is my dissertation, but in many ways it's also yours.

Becoming a parent made me a better scientist, a more efficient one, and a more creative one. I spent less time in the lab but more time mulling over my scientific questions. It made me realize that how often you are at the bench does not determine how successful you are. Being physically present does not necessarily mean you are hardworking, and being physically absent doesn't mean you are not. My children fueled me and made me show up, for myself and for them. They made me more daring, more willing to try because things needed to get done. There was no time to be wasted.

Becoming a parent also made me more appreciative of my own parents, who supported me in realizing my dream of becoming a scientist while others questioned whether that was the right choice. I even questioned it myself many times. But you reminded me of the pursuit, of the motivation that comes from within and is fueled by the rare success moments when we can truly witness something unfold that we hypothesized, and indeed it turns out to be true. Papa, you don't live to read this, and this is one of the saddest truths about my choice to come here! It meant being away, far away from home. It sacrificed my ability to easily get home, and hence I saw you once in health and the next time taking your last breath. Not being able to be more present for the in-between is something I will always deeply regret.

A PhD is a journey, and in my case, it had many ups and downs. I've met a lot of different people, some in passing and some who stayed. I realized that it's not about the lab that you join but about the people you meet along the way, the ones that are driven by common ideas, beliefs, and goals. They are your people, and they keep you going.

Deborah Hegarty is one such person. She went above and beyond to make me feel comfortable working with mice and spent many hours on my side in the mouse room. We often had a good laugh, and I

feel it was time well spent that I think of dearly. Having a family of my own now, I realize how hard it must've been to carve that time out for me, so I'm beyond grateful!

My former lab-mate and dear friend, Julia Huey, who did so many mouse surgeries for me, listened to me complain and has always been fun to be around!

My co-author Craig Dorrell, absolutely, is one of those people. I came to Craig with an idea, and he helped me bring it to life, make it possible. He has helped with every aspect of experiment planning, analysis, and troubleshooting, as well as answering many short-notice texts and handing out reagents – thank you. The same goes for Pamela Canaday. Without Pamela, sorting would've been such a pain. She, however, finds a way to make it fun and engaging, not only because Spock is her favorite machine but because science is something that excites her. She and Craig have worked together for many years, and both welcomed me and helped me tremendously. Frankly, they brought my joy for science back. I'm still not the person who will spend her life at the bench, but I do feel the spark. Also, each sort day was long and tiring, but spending two hours with Pamela and Craig while Spock made his way through my controls and eventually my samples was such a welcome break and something that I've missed. Although Pamela claims to love sorting my samples, she also has been unavailable at times, so I had the pleasure of meeting Christina Matea and Reshma Purohit, who are two very sweet humans that I'm so glad I met along the way!

I would not be writing this if it weren't for Victoria and Marco, who have been colleagues and friends since the very beginning of this journey. Thank you for making sure I (and we) find my (our) place here, for connecting us with valuable resources, and for lending an ear or sometimes even a shoulder when needed. Thank you for believing in both of us, not only as scientists but as people, and for having our back whenever you could.

Larry David is one of those people Victoria and Marco connected me to, and I'm so glad I had the pleasure of meeting him. You are such a kind soul! Thank you for taking us on trips and showing us this beautiful state we've got to call home for many years. Thanks to you, we have many fond memories and a couple of very funny stories that we can share repeatedly.

The Schultz lab: I've known you in many forms and have seen many people come and go, and it's been fun to meet all of you! I will always remember my very first group meeting when I joined the lab back in Heidelberg. The very first presentation was given by Rainer Müller, the resident chemist/molecule wizard at the time, and it was a slide full of structures, numbers, and reagents. Seeing this, I just thought I had made the biggest mistake in my life because I did not understand a single thing! Turns out, I didn't have to, to get where I am today. However, that's always been the fun part of the lab, the mixing between two disciplines (chemistry and biology) that often don't understand each other, but when they do and work on solutions together, great things happen. Special thanks go to Berit Blume, who has been the speedy Gonzalez in terms of giving me feedback on my thesis (!), and Varik Harris for being my go-to person when I had to handle fixatives during my second pregnancy.

Carsten, you've changed the trajectory of my life by offering me the opportunity to join your moving lab as a PhD student. I've often felt lost, overwhelmed, and regretted this choice, but other times I've come to see that my life would be very different had I not agreed to do this. I'm thankful that you have made

it possible for me to combine a PhD and being a mother twice, and the first time while the world was in chaos. Thank you for trusting me to do my work, although maybe not the way you wanted me to, but getting it done, nonetheless.

Show-Ling, thank you for being an invaluable member of my DAC! Your advice and critical but always helpful feedback have helped me many times. Thank you for believing in my abilities and giving me the necessary push to try new approaches.

Thank you to my whole DAC team, Show-Ling Shyng, Larry David, Tom Scanlan, John Williams, and Carsten Schultz, for your support, feedback, and guidance throughout this long and effortful journey.

Chapter 1 Introduction

1.1 Background and Rationale

1.2.1 Glucose Homeostasis and its Disruption in Diabetes

In healthy organisms, blood glucose levels are maintained within a narrow physiological range, typically 70–100 mg/dL in the fasting state and not exceeding ~140 mg/dL postprandially (1) (Fig. 1a). This steady state, referred to as euglycemia, is essential to ensure adequate glucose supply to vital organs, particularly the brain, while avoiding the deleterious consequences of chronic hyperglycemia or hypoglycemia (2). Achieving euglycemia depends on the integrated action of multiple endocrine cell types within the pancreatic islet of Langerhans, most prominently insulin-secreting β-cells and glucagon-secreting α-cells (Fig. 1b). Insulin acts as the principal glucose-lowering hormone by stimulating glucose uptake in peripheral tissues such as muscle and adipose tissue and by inhibiting hepatic glucose production (3) (Fig. 1a). Conversely, glucagon functions as the primary blood glucose-elevating hormone by promoting hepatic glycogenolysis and gluconeogenesis (4). The opposite actions of insulin and glucagon form the cornerstone of glucose homeostasis, requiring dynamic and context-dependent regulation in response to nutrient intake and energy demands.

When this finely tuned balance is perturbed, pathological states arise. Diabetes mellitus represents the most common and clinically significant disruption of glucose homeostasis. In type 1 diabetes (T1D), autoimmune-mediated destruction of β-cells leads to absolute insulin deficiency (5). In type 2 diabetes (T2D), a combination of impaired insulin secretion, insulin resistance in peripheral tissues, and inappropriate glucagon secretion contributes to chronic hyperglycemia (6). Both forms of the disease are associated with progressive islet dysfunction and result in increased risk for microvascular and

macrovascular complications (7). Understanding how glucose homeostasis is normally achieved, and how these processes fail in diabetes, is therefore fundamental to identifying new therapeutic strategies.

1.2.2 Intercellular Communication Shaping Islet Hormone Secretion

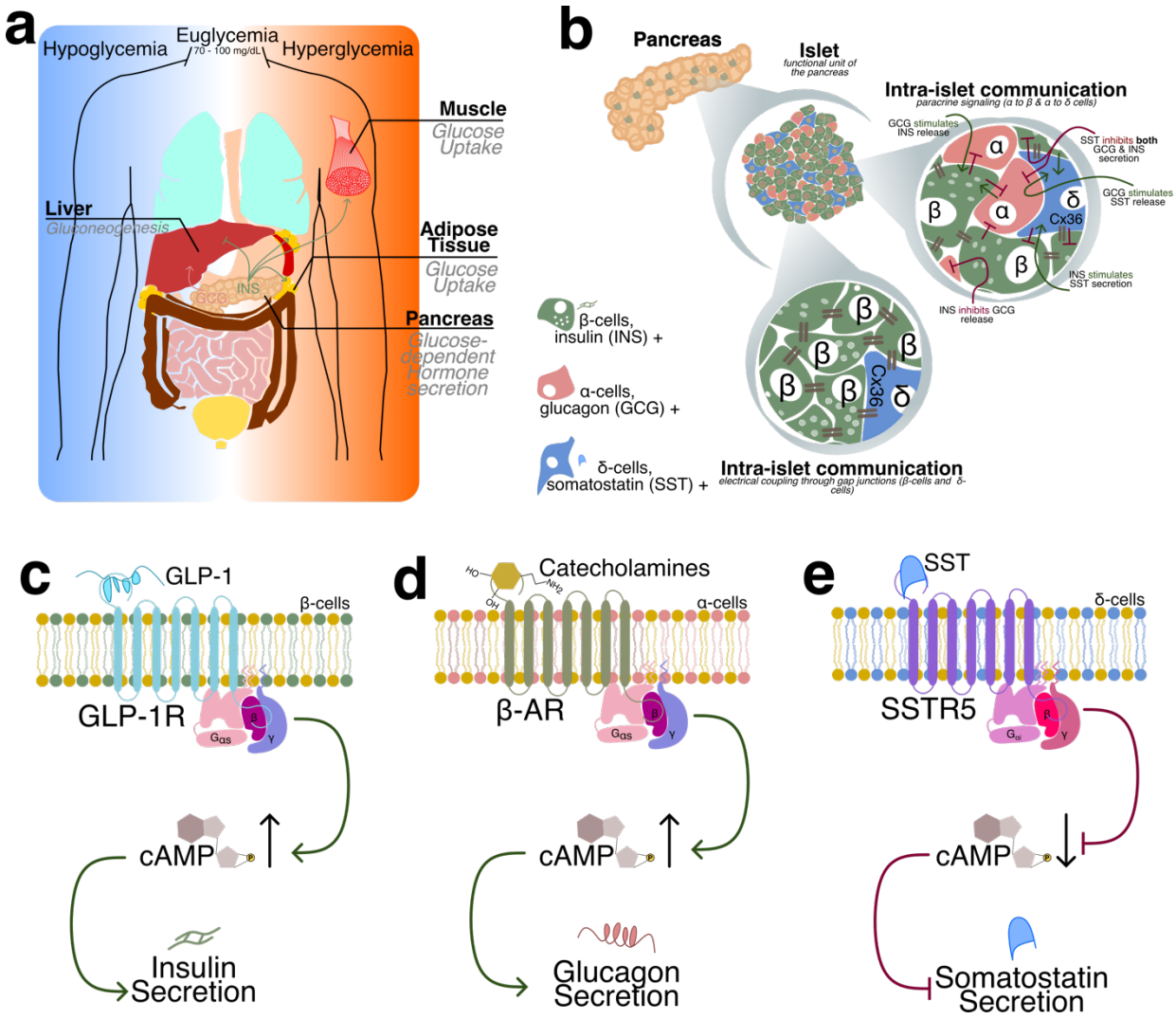

Figure 1: Overview of the core concepts explored in this thesis. (**a**) Systemic glucose homeostasis. Glucose homeostasis (euglycemia) is essential for maintaining whole-body metabolic balance. Both extremes, hypoglycemia (blue), when blood glucose falls too low, and hyperglycemia (orange), when it rises excessively, are conditions the body strives to avoid. The pancreas plays a central regulatory role by secreting the key hormones insulin (INS, green) and glucagon (GCG, pink), whose balanced action maintains euglycemia. INS facilitates glucose uptake into adipose tissue (yellow) and skeletal muscle (red) while simultaneously inhibiting hepatic (red) gluconeogenesis, thereby preventing additional glucose release into circulation. Conversely, GCG promotes hepatic gluconeogenesis and glycogenolysis, particularly during hypoglycemia, to restore normoglycemia. (**b**) The islet microenvironment. INS and GCG are produced and secreted by endocrine cells within the pancreatic islets of Langerhans, which function as miniature organs coordinating local hormone release. In addition to INS-producing β-cells (green) and GCG-producing α-cells (pink), the islet contains somatostatin (SST)-secreting δ-cells (blue). For simplicity, minor endocrine cell types have been omitted. β-cells are electrically coupled via connexin 36 (Cx36) gap junctions, enabling synchronized insulin secretion, whereas α-cells are not electrically connected to other endocrine cell types. Consequently, two major forms of intra-islet communication coexist: electrical coupling among β-cells and paracrine signaling between α-, β-, and δ-cells. Paracrine regulation is crucial for coordinated hormone output and glucose control: SST from δ-cells inhibits both NS and GCG secretion; INS inhibits GCG but stimulates SST release; and GCG promotes INS secretion. (**c–e**) GPCR-mediated control of islet hormone secretion. At the molecular level, endocrine cells express numerous G protein–coupled receptors (GPCRs) that act as molecular "antennas" sensing hormonal, neuronal, and metabolic cues. (**c**) In β-cells, activation of the glucagon-like peptide-1 receptor (GLP-1R, cyan) by its ligand GLP-1 increases intracellular cyclic adenosine monophosphate (cAMP, brown), promoting INS secretion. (**d**) In α-cells, β-adrenergic receptor (β-AR, olive) stimulation by catecholamines (khaki) elevates cAMP, thereby enhancing glucagon release. (**e**) In δ-cells, somatostatin exerts autocrine feedback via SSTR5 (purple), which is Gαi-coupled and reduces intracellular cAMP, leading to inhibition of somatostatin secretion. Cartoons are intentionally simplified to highlight key signaling principles and intercellular relationships relevant to the regulation of glucose homeostasis.

The islet operates as a multicellular micro-organ in which endocrine cell types: α-, β-, δ- (somatostatin-secreting), PP- (pancreatic polypeptide)-secreting, and ε-cells (ghrelin-secreting), coordinate their

activities through both direct and indirect modes of communication (8). Cell–cell contact via gap junctions (such as Connexin 36) and adhesion molecules allows for electrical and metabolic coupling among β-cells, facilitating synchronous insulin release in response to rising glucose levels (9) (Fig. 1b). In parallel, paracrine signaling within the islet enables one hormone-secreting cell type to modulate the activity of another: *e.g.*, somatostatin released from δ-cells exerts inhibitory effects on both insulin and glucagon secretion, thereby acting as a local “brake” to fine-tune hormone output (10–12) (Fig. 1b and Fig. 2).

Beyond intra-islet signaling, endocrine cells integrate systemic cues delivered through circulating nutrients, hormones, and neural inputs. Nutrients such as glucose, fatty acids, and amino acids act as direct metabolic signals, modulating hormone secretion by serving as substrates for intracellular metabolism and signaling pathways (13,14). Neural input, mediated primarily via the autonomic nervous system, provides rapid communication between central nervous system (CNS) energy-sensing pathways and the islet: parasympathetic cholinergic stimulation promotes insulin release during feeding, whereas sympathetic adrenergic signals enhance glucagon secretion under conditions of stress or hypoglycemia (15,16). This convergence of paracrine, endocrine, and neuronal signals positions the islet as a highly dynamic signaling hub, continuously sensing and responding to the metabolic state of the organism.

1.2.3 GPCRs as Molecular Antennas: Integrating Diverse Signals to Maintain Glucose Homeostasis

The ability of pancreatic islet cells to interpret and respond to the many local and systemic signals depends largely on the activity of cell-surface receptors, particularly G protein–coupled receptors (GPCRs) (Fig. 1c-e). GPCRs constitute the largest family of membrane receptors in mammals and function as molecular “antennas” that detect extracellular ligands, such as neurotransmitters,

hormones, metabolites, and trace amines, and translate these signals into intracellular responses via heterotrimeric G proteins (17).

In the islet, GPCRs are expressed across all major endocrine cell types and play essential roles in regulating hormone secretion. β-cell GPCRs such as the glucagon-like peptide-1 receptor (GLP-1R) and the glucose-dependent insulinotropic polypeptide receptor (GIPR) enhance glucose-stimulated insulin secretion through cAMP- and Ca^{2+}-dependent signaling cascades (18–20) (Fig. 1c). Similarly, α-cell GPCRs, including adrenergic receptors, enable rapid mobilization of glucagon release during sympathetic activation (21,22) (Fig. 1d). Other GPCRs mediate autocrine and paracrine communication within the islet, as seen with somatostatin receptors that mediate δ-cell–derived inhibition of β- and α-cells (11) (Fig. 1e).

Importantly, GPCR signaling within the islet is characterized by redundancy and crosstalk. Multiple GPCR subtypes converge on overlapping intracellular pathways, ensuring robustness of glucose regulation even when one signaling pathway is impaired (17,23). This redundancy underscores the resilience of the system but also highlights the complexity that must be navigated when targeting GPCRs pharmacologically. Given their central role in regulating islet communication, GPCRs represent attractive therapeutic targets for diabetes, as suggested by the clinical success of GLP-1R agonists (24,25). Nonetheless, many GPCRs expressed in islets remain incompletely characterized, and identifying how they contribute to glucose homeostasis represents an important frontier in diabetes research.

1.2 The pancreatic islet and its internal organization

The pancreatic islet, also known as the islet of Langerhans, is the endocrine compartment of the pancreas, embedded within the surrounding exocrine tissue. Endocrine cells are the hormone-secreting cells (*e.g.,* insulin and glucagon) of the pancreas, whereas exocrine cells, comprising acinar and ductal epithelial cells, are primarily responsible for supplying digestive enzymes (26–28). Within the endocrine

pancreas, the pancreatic islet cell types collectively regulate glucose homeostasis through the hormones they secrete (Fig. 2). The most abundant endocrine cell type in the islet is the β-cell, which secretes insulin, the sole hormone in the body capable of lowering blood glucose levels (29). Insulin promotes glucose uptake and storage, playing a central role in maintaining euglycemia (30). Counterbalancing insulin's effects is glucagon, a hormone secreted by α-cells. Glucagon raises blood glucose levels by stimulating hepatic gluconeogenesis and glycogenolysis. The release of both insulin and glucagon is modulated by δ-cells, which secrete somatostatin (Fig. 2). Somatostatin acts as a paracrine inhibitor of both β- and α-cell function, positioning δ-cells as critical local regulators of islet hormone secretion (11,31,32).

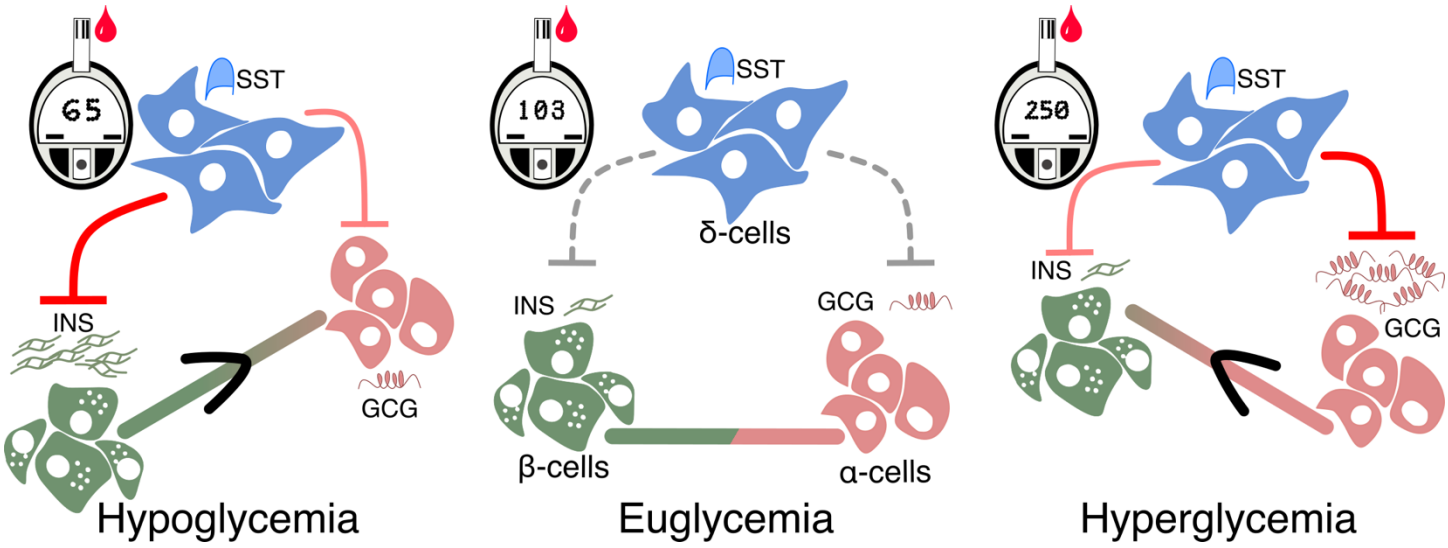

Figure 2: Schematic representation of paracrine regulation among islet endocrine cells under varying glycemic states. Glucose homeostasis (euglycemia) is maintained through the coordinated actions of insulin (INS), secreted by β-cells (green), and glucagon (GCG), secreted by α-cells (red). This balance is modulated by somatostatin (SST), released from δ-cells (blue), which exerts inhibitory control over both INS and GCG secretion in a glucose-dependent manner. During hypoglycemia, δ-cell activity and SST release are diminished, permitting GCG secretion from α-cells and suppressing INS release from β-cells. Conversely, during hyperglycemia, δ-cell activity and SST output increase, leading to inhibition of GCG secretion and modulation of INS release to prevent excessive glucose lowering, thereby stabilizing glycemic homeostasis.

Each pancreatic cell type is necessary to achieve euglycemia in the organism (Fig. 2). Insulin (INS) is the hormone that lowers blood glucose, glucagon (GCG) is the hormone that increases blood glucose, and somatostatin (SST), at least within the islet, controls the secretion of both hormones (33). The synergy between those three cell types has been extensively described and recognized as key to secreting sufficient concentration of each of the hormones, as clusters made from single cell types or

immortalized cell lines of each of the populations do not produce nearly enough of the respective hormone compared to what is observed within the organism (34).

In human islets, β-cells comprise approximately 60 % of the endocrine population, α-cells about 30 %, and δ-cells around 2 % (35–37). The remaining fraction consists of less abundant cell types such as pancreatic polypeptide (PP) cells and ε-cells, the latter of which secrete ghrelin (38,39). Although these populations are less well characterized, they are thought to contribute to broader regulatory networks within the islet microenvironment (38,40).

Islet architecture varies notably between species. In rodents, endocrine cells are arranged in a core-mantle structure, with β-cells occupying the core and α-cells forming a peripheral mantle interspersed with δ-cells (26). δ-cells appear to be randomly distributed but exhibit cytoplasmic extensions that allow them to contact multiple cell types across the islet, facilitating widespread paracrine regulation (12,41–43). Human islet architecture is less defined by a core-mantle pattern and more frequently presents as a heterogeneous mix of α-, β-, and δ-cells (Fig. 4, native islet). Nonetheless, some evidence indicates that during early development, and within smaller islets, human islets also display a localized core–mantle organization, with α-cells forming a mantle around β-cell cores, like rodent islets. This pattern is most evident in islets measuring 40–60 μm in diameter and tends to diminish as islet size increases and postnatal remodeling occurs (44).

Human islets also display substantial heterogeneity in size and morphology. Smaller islets are enriched in β-cells and are believed to disproportionately contribute to the insulin-secreting capacity of the pancreas (45). In contrast, larger islets exhibit distinct patterns of vascularization, which may influence nutrient and hormone exchange. Despite their clinical relevance, detailed knowledge of human islet cytoarchitecture remains limited (27,46,47). This is largely due to the restricted availability of donor tissue and the terminal nature of human islet isolation procedures. Furthermore, the islet is a highly

complex micro-organ, comprising not only multiple endocrine cell types but also vascular endothelial cells, pericytes, and neuronal inputs, all of which contribute to its functional integrity (27,48,49).

1.2.4 How to study the pancreatic islet – the need for reverse (bio)engineering

The pancreatic islet can be regarded as a micro-organ whose study requires diverse experimental systems. Reductionist approaches employ immortalized endocrine cell lines, which are accessible and scalable but lack the multicellular complexity of intact islets (50–52). *In vivo* studies in mouse models enable investigation of islet physiology within the context of whole-organism homeostasis (53,54), whereas donor-derived human islets provide the most translationally relevant material for studying human-specific biology (55–57). Organoid systems allow reverse-engineered assembly of islet-like structures, offering a platform to dissect developmental and structural principles. In addition, stem cell–derived β-like cells or islet-like clusters provide renewable sources of endocrine tissue for disease modeling and therapeutic exploration (58). Computational modeling offers an *in silico* approach to study islet electrophysiology, Ca^{2+} dynamics, and insulin secretion at multiple scales (59,60). Finally, emerging microfluidic 'islet-on-a-chip' systems integrate controlled perfusion and environmental cues, enabling detailed study of islet function under physiologically relevant conditions (61–63).

Organoids are 3D-tissue constructs generated *in vitro* from a small number of progenitor cells, most often pluripotent stem cells, under conditions that recapitulate organ formation (62,64) (exemplary workflow depicted in Fig. 3). In practice, progenitor cells are embedded within an extracellular matrix scaffold (commonly Matrigel) and exposed to a defined sequence of growth factors, hormones, and signaling molecules that guide self-organization into structures resembling the native organ. Organoid protocols have been established for the cerebral cortex (65), gastrointestinal tract (66–68), kidney (69), and pancreas (62,70–73). In the pancreatic model, $PDX1^+$/$NKX6.1^+$ progenitor cells undergo scaffold-supported morphogenesis in the presence of specific cues to form islet-like clusters that mirror both the architecture and endocrine function of the native islet of Langerhans (71,72).

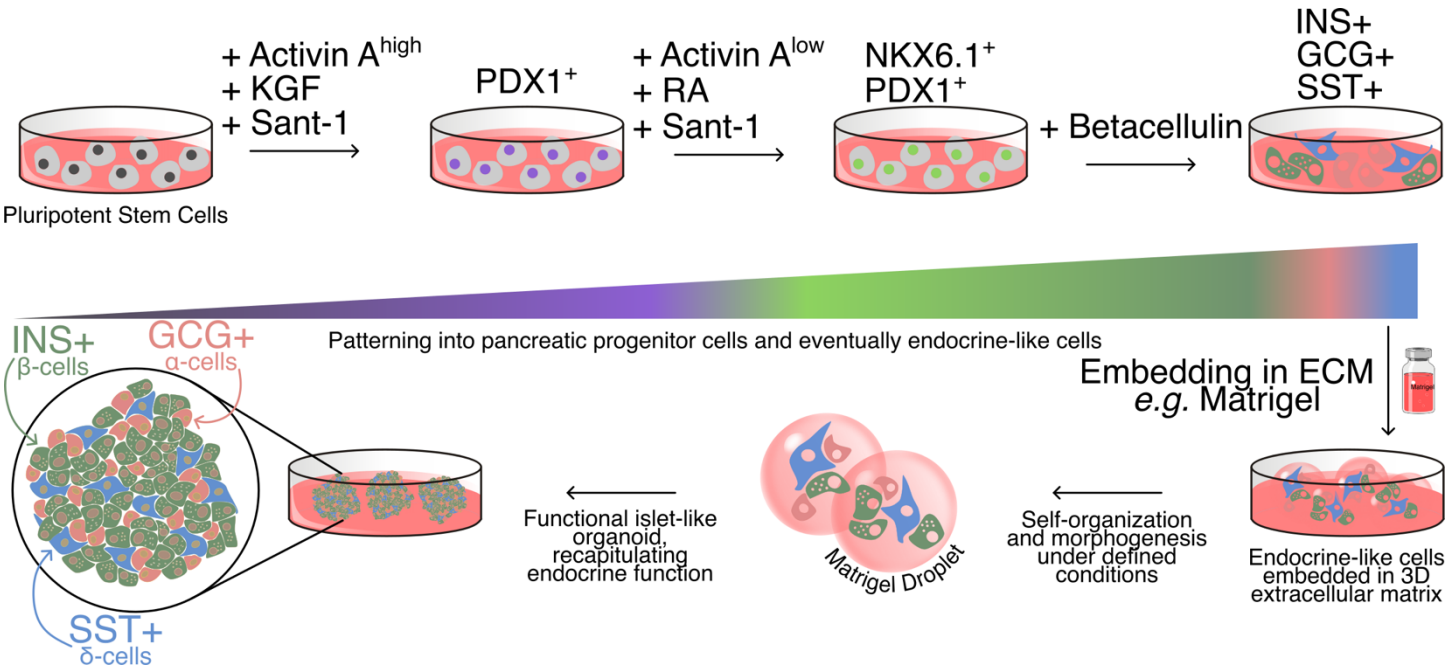

Figure 3: Stepwise directed differentiation of human pluripotent stem cells into islet-like organoids. Human pluripotent stem cells are sequentially exposed to stage-specific morphogens to promote stepwise lineage commitment toward the pancreatic endocrine lineage. For clarity, only representative additives are depicted, including Activin A, Keratinocyte Growth Factor (KGF), Smoothened Antagonist (Sant-1), Retinoic Acid (RA), and Betacellulin. These factors collectively guide patterning from definitive endoderm to pancreatic progenitor (PDX1$^+$/NKX6.1$^+$) and subsequent endocrine-like cell states, which express insulin (INS$^+$, green; β-cells), glucagon (GCG$^+$, pink; α-cells), or somatostatin (SST$^+$, blue; δ-cells). Embedding differentiated cells in an extracellular matrix scaffold (*e.g.,* Matrigel) supports three-dimensional self-organization and morphogenesis, yielding functional islet-like organoids that recapitulate key structural and endocrine features of the native islet of Langerhans.

The inherent complexity of intercellular interactions within the islet renders 2D culture systems insufficient for studying endocrine function. Intact islets and 3D cell clusters exhibit distinct insulin-secretion dynamics compared to isolated endocrine cells or pancreatic cell lines, reflecting the importance of specialized cell–cell and cell–matrix communication. Endocrine cells use gap junctions, cadherins, integrins, and ephrin signaling to coordinate their activity with neighboring cells, while paracrine factors provide additional layers of regulation. Disruption of these networks profoundly impairs glucose-stimulated insulin secretion, underscoring the need for models that preserve native microarchitectural cues (35,42,44,74,75).

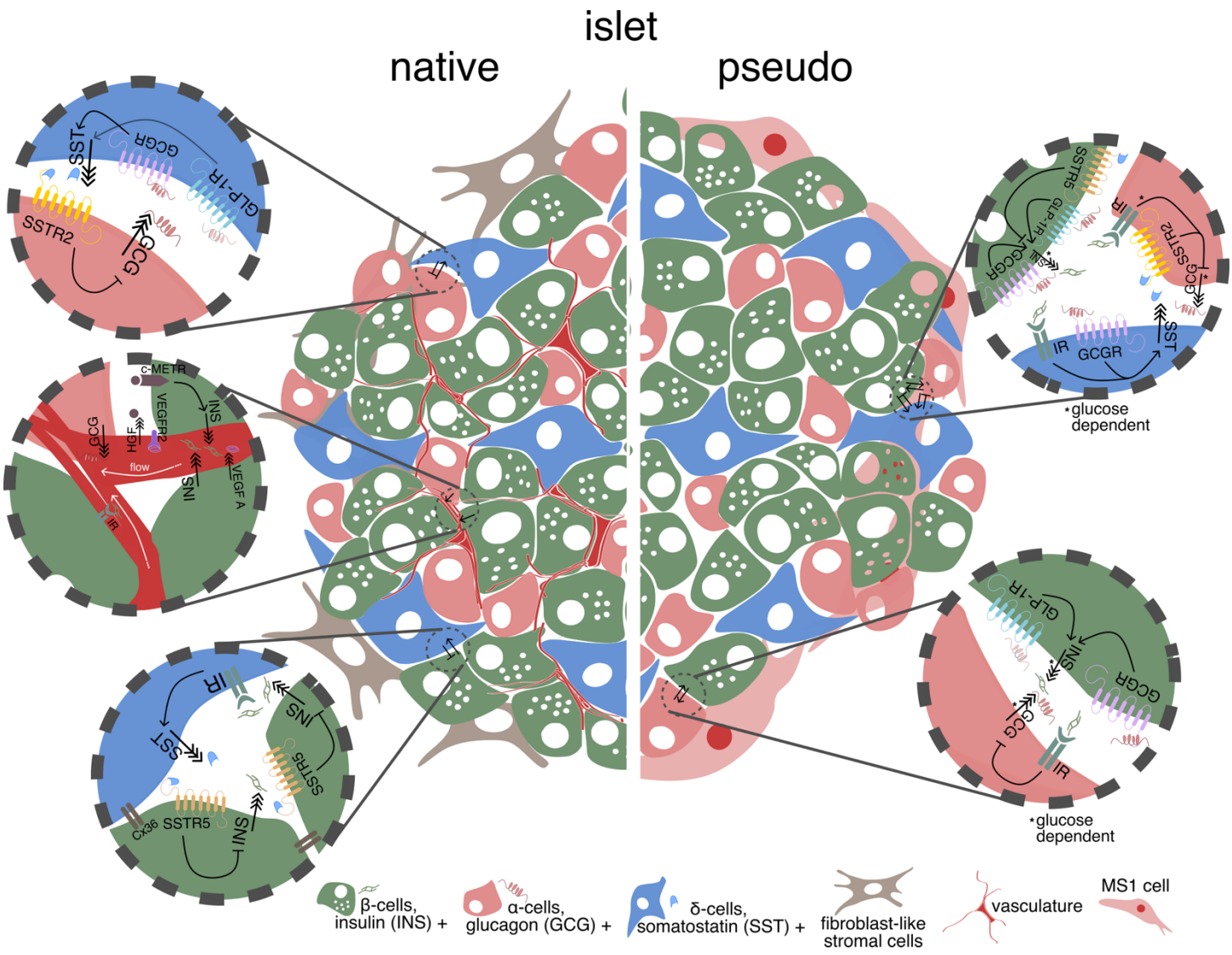

Figure 4: Simplified schematic comparing a native human islet (left) with a pseudo-islet (right). The native islet is composed of β-cells (green), α-cells (pink), δ-cells (blue), and fibroblast-like stromal cells (brown), while the pseudo-islet contains the same endocrine cell types but is reconstituted with Mile Seven 1 (MS1) cells, which mimic fibroblast-like stromal cells. The most notable difference between the two structures is the presence of a vascular network in native islets (red), which is absent in pseudo-islets. Zoom-in panels highlight representative cell–cell interactions. In the native islet, δ-cells express glucagon receptor (GCGR) and GLP-1 receptor (GLP-1R), and activation by GCG or GLP-1 potentiates SST release, which in turn suppresses GCG secretion from α-cells through SST receptor 2 (SSTR2). α- and β-cells are polarized such that their hormone release is directed toward the vasculature, with signaling flow organized as β-cell → α-cell → δ-cell. β-cells secrete vascular endothelial growth factor A (VEGF-A) to activate vascular endothelial growth factor receptor 2 (VEGFR2) on endothelial cells, thereby promoting vascular stability and tone, while endothelial cells reciprocally secrete hepatocyte growth factor (HGF), which binds c-MET on β-cells to enhance insulin secretion. β-cells are further electrically coupled through Connexin 36 (Cx36) gap junctions and interact in a paracrine fashion with δ-cells. Insulin secreted from β-cells activates the insulin receptor (IR) on δ-cells to boost SST release, which in turn suppresses insulin secretion via SST receptor 5 (SSTR5). In the pseudo-islet, both INS and GCG stimulate δ-cells to secrete SST, which inhibits further GCG and INS secretion through SSTR2 on α-cells and SSTR5 on β-cells, respectively. In addition, β-cells sense GCG primarily through GCGR and, with lower affinity, through GLP-1R, both of which enhance insulin secretion, while insulin binding to IR on α-cells inhibits GCG release.

Reverse (bio)engineering involves reconstructing functional islets by sequentially assembling defined cellular and extracellular components, thereby enabling systematic dissection of the factors that influence islet formation and function. Weitz, Menegaz, and Caicedo have proposed this strategy as a

powerful way to study islet biology (34). However, in practice, this process is time-consuming and costly. From start to finish, organoid formation spans roughly 19 days, or 8 days when counted from the pluripotent stage (when human induced pluripotent stem cells (hiPSCs) have fully differentiated into pancreatic progenitor cells) (71) (exemplary workflow in Fig. 3).

Despite their promise, organoid systems have significant limitations (64,73,76). The absence of a perifusable vasculature restricts oxygen and nutrient diffusion to the organoid core, resulting in hypoxia-induced necrosis that limits both size and long-term viability. Standard cultures also omit key microenvironmental constituents, *e.g.*, resident immune cells, endothelial networks, neural innervation, and dynamically regulated extracellular matrix components. All of these are essential for accurate modeling of cell–cell and cell–matrix interactions *in vivo*. Moreover, organoids often remain at fetal or neonatal stages of differentiation, failing to recapitulate mature tissue physiology and thus constraining their relevance for modeling adult-onset diseases. Finally, substantial batch-to-batch variability in organoid size, cellular composition, and architecture hampers reproducibility and scalability (64,73,76).

1.2.5 Pseudo-islets: a modular system to study the pancreatic islet

In the literature, the term “pseudo-islets” has been applied to a variety of constructs, sometimes to clusters formed from a single pancreatic cell line, and other times to mixed aggregates of different pancreatic cell lines. In this thesis, however, pseudo-islets are defined as three-dimensional cell clusters generated from distinct populations generated by fluorescent-activated cell sorting (FACS). These human-donor endocrine cells were then combined with mouse Mile Sven 1 (MS1) endothelial cells at a 1:10 endocrine-to-endothelial ratio in suspension (Fig. 4, pseudo islet). This system follows a reverse-engineering paradigm: complexity is built stepwise by adding defined “building blocks” (each pancreatic cell type) to the assembly (34). Because it remains fully modular, allowing omission or addition of specific cell types, it is both more adaptable than native islets and suited for dissecting how each “building block” contributes to overall islet organization and function. A direct comparison between native and

pseudo-islets, as well as simplified interactions between the main islet cell types, are visualized in Fig. 4.

Due to the complex interplay among the islets' diverse endocrine constituents, the specific role of each pancreatic cell type in islet function remains incompletely understood. To date, insulin-producing β-cells have been studied most extensively (30). Over the past two decades, however, α-cells have received growing attention (39,77,78), whereas δ-cells (11), PP-cells (40), and ε-cells (38) remain relatively understudied. To dissect individual contributions, we isolated fully mature endocrine cells from healthy human donors. We reassembled them into pseudo-islets, treating each cell type, α, β, and δ, as a discrete "building block." This reverse-engineering strategy allowed for real-time monitoring of islet formation and precise control over composition. For example, by omitting α-cells and supplementing with exogenous glucagon, one can probe the hormones' specific influence on cluster assembly without confounding paracrine or cell-cell contact effects.

This thesis describes the very first steps of what should be considered an ever-evolving model for the pancreatic islet. Here, we generate rather “primitive” pseudo-islets consisting, in full form, only of α-, β-, δ-cells, and MS1 cells to support islet formation and structure. However, PP-cells and ε-cells could be added. Additionally, neuronal cells, immune cells, engineered reporter lines, or any cell type one is interested in studying can be applied to the system, and their effect on islet formation and functionality can be investigated (Fig. 5).

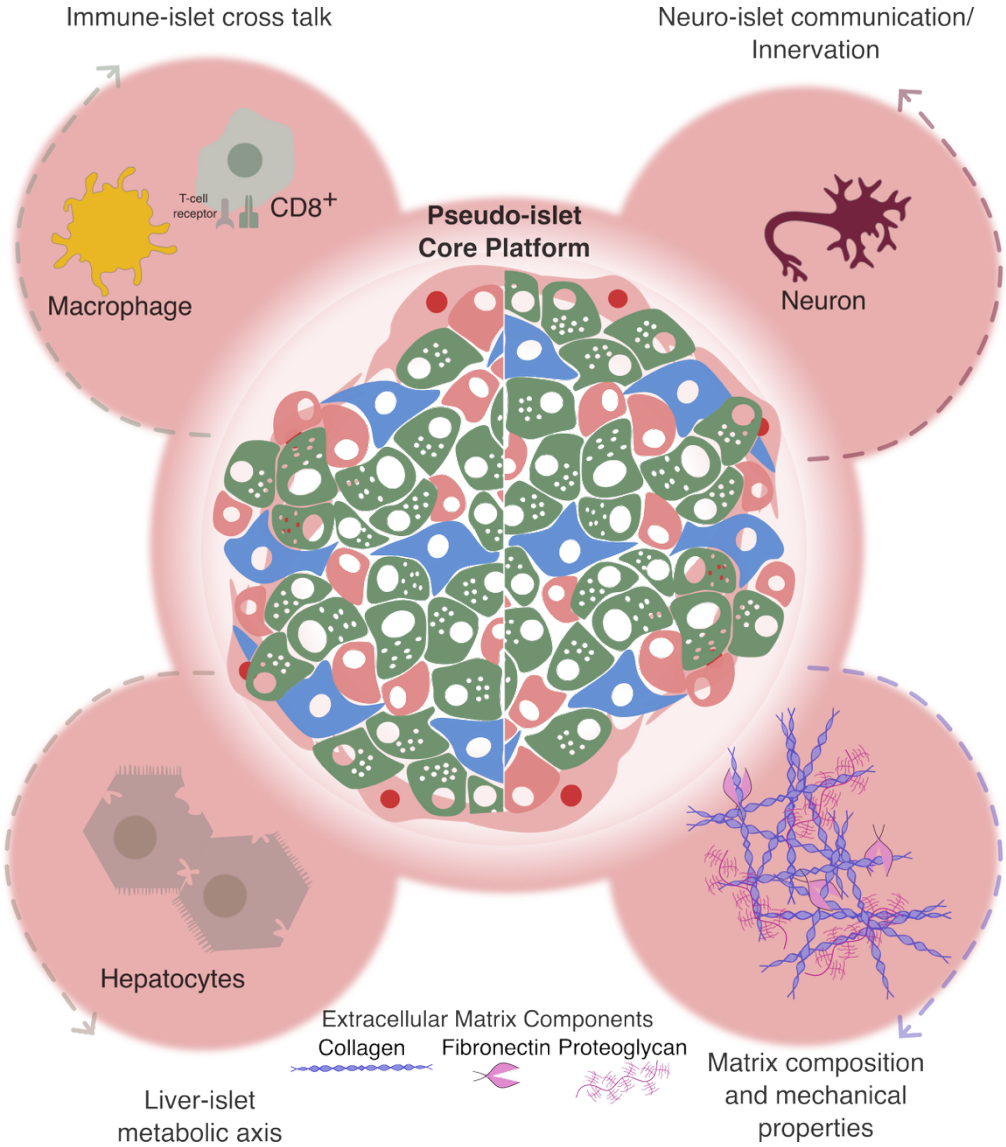

Figure 5: The pseudo-islet platform. The pseudo-islet core represents a self-organized, multicellular construct recapitulating native endocrine organization. Surrounding modules illustrate possible extensions to study specific physiological interactions: immune–islet crosstalk (macrophages (yellow), $CD8^+$ T cells (green)), neuro–islet communication and innervation (red), liver–islet metabolic coupling (grey), and extracellular matrix composition and mechanics. These possible additions, highlight the versatility of the pseudo-islet platform to be used in answering a variety of research questions.

1.2.6 Challenges in working with human donor islets

Human donor islets remain the most physiologically relevant model system for investigating β-cell biology, intercellular communication, and human-specific regulatory mechanisms of hormone secretion (79). However, the use of donor islets is accompanied by inherent challenges that complicate experimental design, data interpretation, and reproducibility. These limitations arise both from biological variability among donors and technical differences in islet procurement and preparation.

A central challenge is donor-to-donor variability (79). Unlike standardized *in vitro* or animal models, human islets are obtained from organ donors with highly diverse genetic, metabolic, and environmental backgrounds. Such variability can strongly influence islet yield, composition, and function. For example, measures of glucose-stimulated insulin secretion (GSIS) differ considerably across donors, often independently of the quality of isolation, underscoring the heterogeneity of intrinsic β-cell responsiveness (79,80).

This biological variation is further compounded by technical inconsistencies in islet isolation, which further limit reproducibility (79). Donor islets are typically obtained through collaborative isolation centers, each employing distinct enzymatic digestion protocols, purification gradients, and handling practices. These factors directly affect islet integrity, purity, and viability, resulting in substantial site-to-site differences in preparation quality (79,81,82). Consequently, even well-matched donor cohorts may yield preparations of unequal experimental value, emphasizing the need to carefully control for the isolation center as a variable in multi-donor studies.

Donor characteristics add another layer of influence on islet quality and functional performance. Age is negatively associated with β-cell proliferative capacity and may impair functional reserve, as older donor islets often exhibit diminished GSIS compared to younger ones (83). Body mass index (BMI) is also a critical determinant: while moderate excess weight may enhance islet mass due to compensatory β-

cell expansion, obesity is frequently linked to insulin resistance, altered paracrine signaling, and impaired β-cell function (84). Glycemic status, as reflected in donor hemoglobin A1c (HbA1c or A1c), directly correlates with β-cell dysfunction. Islets from donors with elevated A1c values display blunted insulin secretion and increased susceptibility to glucotoxicity (85–87).

Donor sex has emerged as another particularly relevant but historically underexplored determinant of islet physiology. Evidence suggests that sex hormones shape both β- and α-cell function. Estrogen signaling in female islets enhances insulin biosynthesis, promotes β-cell survival, and modulates glucagon secretion, contributing to improved glucose homeostasis under metabolic stress (88,89). Conversely, male islets often exhibit lower insulin secretory capacity under equivalent glucose stimulation, and men appear more prone to β-cell dysfunction in the context of obesity and T2D (90,91).

In women, fluctuations of sex hormone levels across the reproductive cycle further influence islet function. Estradiol and progesterone levels vary substantially throughout the menstrual cycle, with estradiol peaking in the late follicular phase and progesterone predominating in the luteal phase. These cyclical changes have been shown to modulate insulin sensitivity, insulin secretion, and glucagon regulation, resulting in dynamic alterations of glucose homeostasis across the cycle (92,93). Pregnancy represents a more extreme state of endocrine adaptation, where placental hormones, including human placental lactogen, progesterone, and estrogens, drive profound insulin resistance. To compensate, maternal β-cells undergo expansion and functional enhancement, leading to increased insulin secretory capacity (94–96). Failure of these adaptive mechanisms contributes directly to the development of gestational diabetes mellitus, highlighting the sensitivity of islets to the hormonal environment during reproductive states. Later in life, menopause is associated with a marked decline in circulating estrogens, accompanied by a reduction in insulin sensitivity and β-cell protective signaling. Postmenopausal women consequently display increased risk of T2D, a risk that is partly mitigated by estrogen replacement therapy, which restores aspects of β-cell function and insulin sensitivity (89,97,98).

These observations underscore that sex is not a neutral biological variable, but a determinant of endocrine function shaped by hormonal state across the lifespan. Donor islet studies that fail to account for female reproductive status, pregnancy history, or menopausal state risk overlooking critical contributors to variability in islet function and hormone secretion. In summary, while human donor islets provide unmatched relevance for translational diabetes research, experimental outcomes are strongly influenced by inter-donor variability, technical preparation factors, and donor characteristics such as age, BMI, A1c, and sex. Careful cohort selection, rigorous reporting of donor metadata, and stratified analyses are therefore essential to maximize reproducibility and interpretability when working with this valuable but complex biological material.

1.3 Manipulation of hormone secretion by trace amines through trace amine-associated receptor 1

1.3.1 Trace amine-associated receptors (TAARs)

TAARs constitute a family of G protein–coupled receptors (GPCRs) first described in the early 2000s, with several subtypes (TAAR1–TAAR9) identified in mammals (99,100). Among these, TAAR1 was the first to be discovered and is the best-studied subtype (99,100). Early work demonstrated its presence in several cell types, including rat pancreatic tumor cells (ARJ42), one of the first cell lines from which it was isolated (100). As a GPCR, it is unique in that it is primarily intracellularly localized, in contrast to many other GPCRs, which act at the plasma membrane (101). TAAR1 expression has been reported in multiple tissues, including the CNS, gastrointestinal tract (GI), and endocrine pancreas (102). Within the pancreas, TAAR1 is enriched in β-cells (103), whereas other TAAR subtypes (*e.g.,* TAAR2–TAAR9) are more prominently associated with the olfactory epithelium and are implicated in chemosensory signaling (104).

The distinct distribution of TAAR1 underscores its potential to act as a metabolic regulator. Functionally, TAAR1 couples to $G_{\alpha s}$ proteins, leading to the activation of adenylyl cyclase and subsequent elevation of cAMP. This cAMP signal can, in turn, activate protein kinase A (PKA) and exchange protein directly activated by cAMP (EPAC), pathways both known to regulate insulin granule mobilization and exocytosis (105). Thus, TAAR1 links the sensing of endogenous monoamines to well-established second messenger systems within β-cells (simplified visualization in Fig. 6).

In the context of diabetes, TAAR1 has attracted interest as a potential therapeutic target (106). Its pharmacological drugability, demonstrated by the development of highly selective ligands such as RO5166017, RO5256390, and RO5263397 (all by Roche), supports this concept (107). Moreover, the receptors' restricted expression within the islet endocrine compartment positions it at the interface of neurotransmitter-like signaling and hormone regulation. Despite these promising features, current knowledge is largely based on rodent studies and synthetic agonists, while the role of endogenous ligands in human islet physiology remains incompletely understood (108).

1.3.2 Trace Amines (TAs)

TAs are a class of endogenous monoamines structurally related to classical neurotransmitters like dopamine, serotonin, and norepinephrine, but typically present at much lower concentrations (109,110). The most studied TAs include β-phenylethylamine (PEA), p-tyramine (TYR), tryptamine (TRYP), octopamine (OCT), and synephrine (SYN). Historically dismissed as metabolic byproducts, they have since been recognized as physiologically relevant signaling molecules with functional roles mediated primarily through TAAR1 (111).

The link between TAs and diabetes arises from limited evidence on hormone secretion and glucose metabolism. In pancreatic β-cells, TAAR1 activation by TAs enhances insulin secretion by increasing cAMP and Ca^{2+} influx, both of which are central to exocytotic machinery (105,112) (Fig. 6, cell B). The

notion that amines regulate insulin secretion is well established. Beyond TAs, several other biogenic amines influence insulin secretion and broader aspects of diabetes pathophysiology. Serotonin (5-HT) regulates β-cell proliferation and insulin granule release, particularly during pregnancy, where increased islet serotonin synthesis supports adaptive β-cell expansion (113). Dopamine, synthesized from L-3,4-dihydroxyphenylalanine (L-DOPA) within β-cells, acts in an autocrine/paracrine manner through D2-like receptors to inhibit glucose-stimulated insulin secretion (114). Norepinephrine and epinephrine, secreted by sympathetic nerves, strongly inhibit insulin release via α2-adrenergic receptor

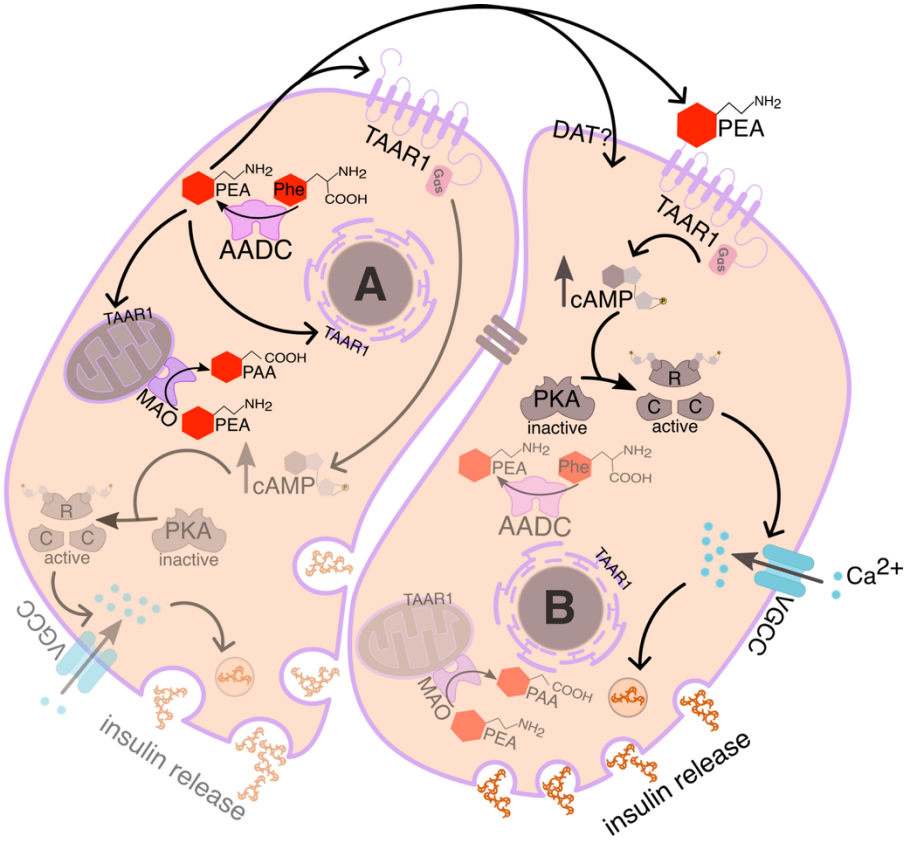

Figure 6: Possible mechanism of TAAR1 signaling in pancreatic β-cells. TAAR1 is known to reside on endomembranes and likely the plasma membrane (PM) (possible sites are marked in mauve). It is stimulated by endogenous TAs such as PEA in an autocrine (β-cell A) or paracrine (β-cell B) manner. Cell A highlights the biosynthetic machinery for the synthesis and degradation of TAs within β-cells. Aromatic amino acid decarboxylase (AADC) catalyzes the conversion of aromatic amino acids to TAs (exemplary shown is the conversion of phenylalanine (Phe) to PEA). PEA might activate TAAR1 of the same cell (autocrine) or on neighboring cells (paracrine). TAs are quickly degraded by monoamine oxidase (MAO), converting PEA to phenylacetic acid (PAA). Cell B highlights the signaling cascade initiated once TAs have activated TAAR1 and subsequently G_{as}, leading to the generation of cAMP, which binds to and activates PKA (grey, regulatory subunit R). The liberated catalytic (C) subunit phosphorylates voltage-gated Ca^{2+} channels (VGCC, blue) and hence increases the influx of Ca^{2+} ions (cyan). Increased intracellular levels of Ca^{2+} trigger the fusion of insulin granules with the PM and insulin secretion. For simplicity, glucose as the main stimulus for insulin release, as well as the ER as an internal Ca^{2+} source, have been omitted. β-cells are electrically coupled by gap junctions (brown bars).

signaling (15). Histamine, though less extensively studied, has been implicated in glucose tolerance and insulin release through histamine 3 (H3) receptor signaling (115).

Taken together, these findings highlight a complex regulatory network in which multiple biogenic amines converge on the endocrine pancreas to fine-tune hormone secretion. Within this network, TAAR1 and its TA ligands represent a relatively underexplored but mechanistically compelling component.

1.3.3 Challenges in studying TAAR1 and trace amine signaling

Despite the growing evidence that TAAR1 contributes to neuroendocrine and metabolic regulation, experimental investigation of this receptor remains challenging. A key obstacle comes from its suspected subcellular localization (116). Unlike most GPCRs, which are inserted in the plasma membrane (PM) and readily accessible to circulating ligands, TAAR1 predominantly resides in intracellular membranes, including the endoplasmic reticulum and potentially mitochondria (100,116–118). This localization implies that ligands must cross the PM to access the receptor. Early binding studies consistently failed to detect ligand interactions at the cell surface, reinforcing the notion that TAAR1 activation is contingent on intracellular access (100). Subsequent work suggested that PM transporters may facilitate this process. The dopamine transporter (DAT) was proposed as one such mechanism, given observations that DAT expression enhanced cellular responsiveness to TAs, such as PEA and amphetamine (118) (Fig. 6, cell B). However, this dependency complicates experimental systems, as receptor activation is likely influenced not only by ligand availability but also by the transporter repertoire of the cell type being studied.

An additional layer of complexity stems from the properties of TAs themselves. Endogenously, TAs are present at low concentrations, generally in the nanomolar to low micromolar range in mammalian tissues (110). Additionally, TAs are rapidly metabolized by monoamine oxidases (MAO-A and MAO-B), leading to short half-lives and making their detection and quantification *in vivo* difficult (109,116). Similar challenges extend to the endocrine pancreas, where TA turnover complicates assessments of their functional impact on insulin secretion.

Together, these barriers underscore the methodological hurdles in investigating TAAR1 and TA signaling. The receptor's intracellular localization necessitates consideration of transporter-mediated entry, while the low abundance and rapid enzymatic degradation of ligands obscure their physiological roles. These challenges have historically led to inconsistent experimental results and complicate efforts to translate TAAR1 biology into therapeutic applications.

1.4 Methodological Framework for Studying Pancreatic Islets

The experimental work in this dissertation relied on a set of complementary biological tools that together enabled the dissection of islet cell function and organization at multiple levels, from single-cell identity to integrated hormone secretion. These approaches were selected to overcome limitations inherent in using either highly simplified *in vitro* systems or fully intact human islets, and they provide both mechanistic insights and physiologically relevant outcomes.

1.4.1 Pseudo-islets

The foundation of this work was the pseudo-islet platform, which allows reaggregation of dissociated primary human islet cells into defined, 3D clusters. Unlike native islets, which are already structurally assembled, pseudo-islets form *de novo* from mature endocrine cells. This approach creates a system in which cell-type composition can be experimentally defined and the process of islet assembly can be directly observed. Moreover, pseudo-islets preserve the maturity of the primary cells from which they are derived, while offering an experimentally tractable platform for manipulations such as culture supplementation or pharmacological perturbation.

1.4.2 Fluorescent-activated cell sorting

To generate cell-type–specific pseudo-islets, FACS was employed. Dissociated human islet preparations were stained with validated surface markers that distinguish α-cells, β-cells, and δ-cells, thereby allowing purification of each population. This ensured the ability to construct pseudo-islets of defined composition as well as to study pure endocrine cell fractions. FACS additionally provided quantitative information about the relative abundance of cell types in human donor islets, enabling comparisons across donors and experimental conditions.

1.4.3 EPI-fluorescence imaging of live native and pseudo-islets in culture

To monitor pseudo-islet formation in real time, EPI-fluorescence imaging was applied. This allowed over-time observation of cell growth, clustering, and reorganization during the aggregation process under culture conditions. Imaging allowed monitoring of qualitative parameters such as cluster size, morphology, and stability. This method was essential for establishing time courses of pseudo-islet maturation and for assessing how experimental manipulations influenced structural outcomes.

1.4.4 Immunohistochemistry of fixed native and pseudo-islets

For endpoint analyses, immunohistochemistry of fixed tissue was conducted on both native and pseudo-islets. This technique provided spatial information about the localization of specific cell types, as well as key hormones and receptors, within the three-dimensional architecture of the islet. Comparisons between native islets and engineered pseudo-islets offered insight into how well reconstituted aggregates recapitulate native cell organization, as well as whether experimental interventions altered the relative positioning or expression patterns of endocrine cell types.

1.4.5 Glucose-stimulated insulin secretion and hormone secretion quantification by ELISA

To assess functional outcomes, GSIS assays were performed, with subsequent quantification of secreted hormones (insulin and glucagon) by enzyme-linked immunosorbent assay (ELISA). This

combination of approaches provided a direct measure of β- and α-cell responsiveness to glucose and allowed evaluation of islet functionality under defined experimental conditions.

1.4.6 Confocal imaging of Ca^{2+} dynamics in live cells

Finally, to investigate intracellular signaling mechanisms, confocal imaging of calcium (Ca^{2+}) dynamics was employed. Ca^{2+} oscillations represent a critical signal transduction step linking glucose metabolism to insulin secretion in β-cells and thus provide a mechanistic readout of stimulus-secretion coupling. By monitoring Ca^{2+} responses in real time across large numbers of cells by confocal imaging enabled detailed analyses of functional heterogeneity, synchronization, and the effects of pharmacological modulation.

Chapter 2 Trace Amines in Health and Disease

This chapter has been formatted for inclusion in this dissertation based on the manuscript “Trace Amines are Essential Metabolites for the Autocrine Regulation of β-Cell Signaling and Insulin Secretion” by Sebastian Hauke, Kaya Keutler, Aurelien Laguerre, Mireia A. Carbo, Jona Rada, David Grandy, Dmytro A. Yushchenko, and Carsten Schultz available on bioRxiv (DOI: https://doi.org/10.1101/2024.03.21.585773), but has been further expanded. The author of this dissertation is the co-first author of this manuscript and used β-cell models, live mouse and human islets to test the influence of trace amines on hormone secretion through the activation of trace amine-associated receptor (TAAR) 1.

2.1 Introduction

Previously, TAAR1 has been identified as potentially involved in the regulation of insulin secretion. Regard *et al.* provided initial evidence by identifying *Taar1* mRNA in mouse β-cells from pancreas sections, confirming expression by qRT-PCR in two mouse β-cell lines, and also detecting *Taar1* mRNA in human islet preparations (119). Their findings supported the notion that β-cells within pancreatic islets are the cell type with the most abundant TAAR1 expression. These observations established that the receptor is expressed “in the right place,” yet expression alone does not confirm receptor functionality, nor whether endogenous ligands are present for receptor activation.

Subsequent studies investigated whether TAAR1 activation influences insulin secretion. Raab *et al.* addressed the *in vivo* relevance of TAAR1 signaling using C57BL/6J mice subjected to intravenous (iv) and oral glucose tolerance tests (oGTT). When the selective TAAR1 agonist RO5166017 (Roche, structure in Fig. 7b) was administered during a GTT, an increase in plasma insulin levels compared to control conditions was observed, indicated by a ~ 20 % reduction in the glucose area under the curve (AUC)

without affecting basal blood glucose levels (105). Michael *et al.* extended these observations to rat and mouse insulinoma cells (INS-1 and MIN6), providing mechanistic insights into downstream signaling. They demonstrated that the insulinotropic effects of TAAR1 agonists T_1AM (3-iodothyronamine) and RO5166017 were abolished by the adenylyl cyclase (AC) inhibitor MDL-12,330A, the TAAR1 antagonist *N*-(3-ethoxyphenyl)-4-pyrrolidin-1-yl-3-trifluoromethylbenzamide (EPPTB) (structure in Fig. 7b) (120), and inhibitors of PKA (H89) and Epac (HJC-0350). These findings further support that TAAR1 is a functional $G_{\alpha s}$-coupled receptor in β-cells, activating AC and leading to cAMP production (112) (cartoon version as seen in Fig. 6). Although EPPTB use indicates ligand specificity, the selectivity of other ligands, in particular endogenous biogenic amines, remains unresolved.

TAAR1 is also recognized as a promiscuous receptor. While trace amines (TAs) are its canonical ligands, many structurally similar biogenic amines can activate it to some extent (121). Most agonists and antagonists, including those developed by Roche, were initially designed to study TAAR1s CNS functions, such as in schizophrenia and depression (122). Revel *et al.* further characterized two selective agonists, RO5256390 (full agonist) and RO5263397 (partial agonist) (structures in Fig. 7b), across rodent, primate, and human TAAR1. Additionally, using the TAAR1-KO with a β-galactosidase (lacZ) reporter, they confirmed receptor expression only in β-cells and not α-cells, but did not directly link receptor activity to insulin secretion (107,123).

Taken together, current studies address several of the key criteria required to establish TAAR1 involvement in insulin secretion. Expression in the relevant cell type has been demonstrated by Regard *et al.*(119) and confirmed with β-cell specificity by Revel *et al*. (107). Functional causality has been suggested by Raab *et al. in vivo* (mouse) (105) and by Michael *et al.* (112) in insulinoma cell lines. Pharmacological specificity has been partially established using the selective agonist RO5166017 and the antagonist EPPTB. Mechanistically, Michael *et al.* further demonstrated that TAAR1 activation stimulates AC, elevates cAMP, and increases intracellular Ca^{2+}, providing downstream signaling evidence.

Finally, *in vivo* physiological relevance has been indicated by reduced glucose AUC in mice treated with RO5166017 (105).

Our work was inspired by these findings. We screened TAAR1 ligands, including endogenous ones, such as the most prominent members of the TA family (β-phenylethylamine (PEA), p-tyramine (TYR), tryptamine (TRYP), synephrine (SYN), and octopamine (OCT)), for effects in β-cells using the MIN6 cell line (see structures in Fig. 7a). MIN6 cells were chosen not only as a β-cell model but also because they simulate pancreatic islets through multihormonal expression (as indicated by Nakashima *et al.*, 2009) (124). In collaboration with colleagues from the Veteran Affairs (VA) hospital in Portland, OR, we utilized a TAAR1-KO mouse model (125) to perform GTTs, insulin tolerance tests (ITT), and microscopy on isolated islets, assessing Ca^{2+} dynamics as a proxy for insulin secretion. This allowed us to touch on functional causality, specificity, signaling, and *in vivo* relevance of TAAR1 under the lens of applying endogenously relevant compounds.

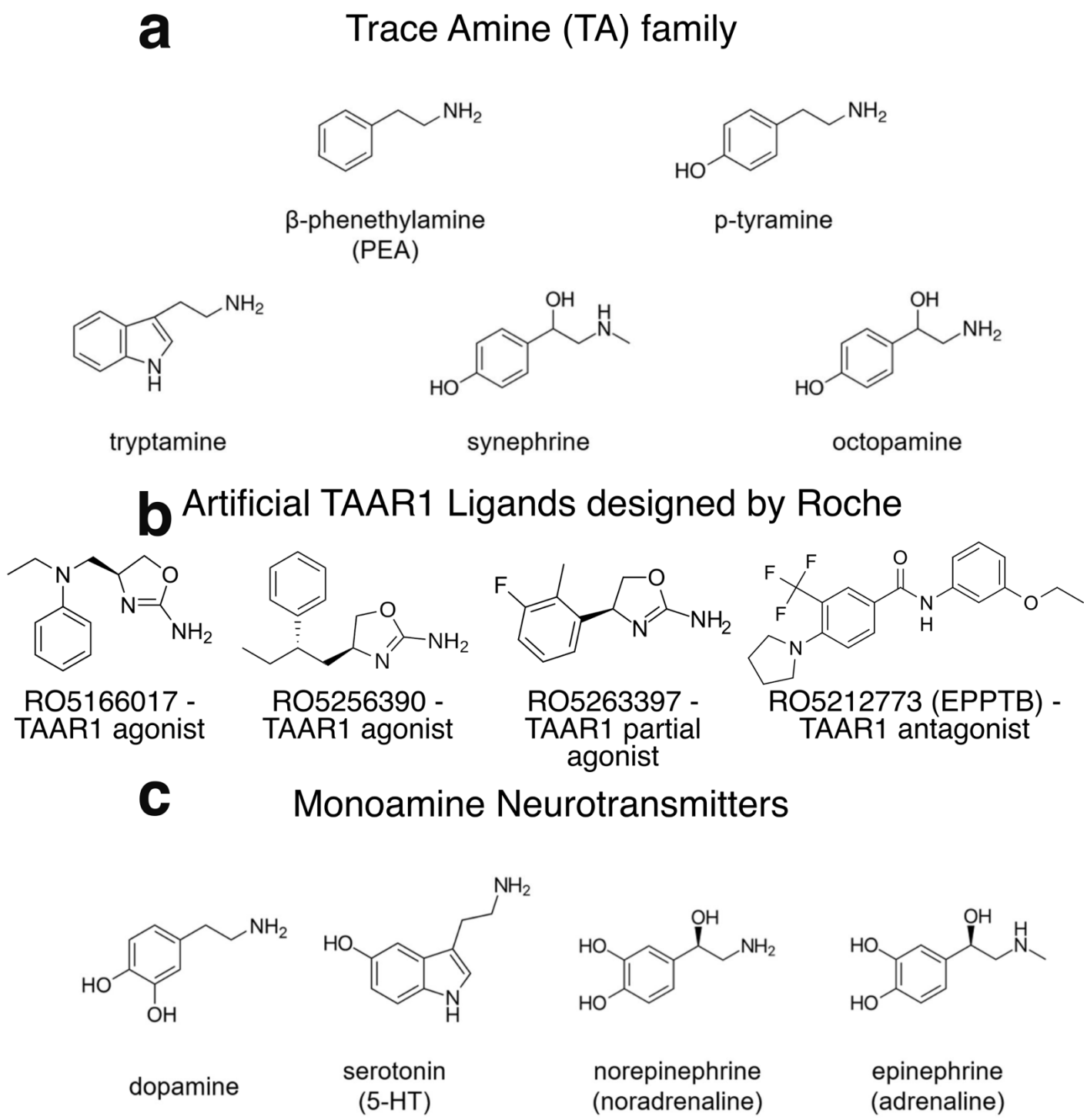

Figure 7: Representative chemical structures of (a) endogenous TA, (b) synthetic TAAR1 agonists and antagonists, and (c) classical monoamine neurotransmitters.

Despite the progress that has been made in deciphering the involvement of TAAR1 in β-cell function, some gaps remain. So far, most evidence relies on synthetic ligands with unknown endogenous relevance, and it is not investigated whether endogenous ligands would have similar effects, particularly in humans. Given the affinity differences in terms of antagonism that have been reported between rodent

and human TAAR1 (126), it is not advisable to extrapolate rodent findings to human physiology. Further, studies have not yet employed β-cell–specific TAAR1 knockout or knockdown models, which would be essential to definitively attribute the observed effects to TAAR1 rather than compensatory pathways. Additionally, the mouse model used so far in TAAR1 research is the C57BL/6J strain, which is known to have intrinsic alterations in glucose homeostasis due to a loss-of-function nicotinamide nucleotide transhydrogenase (*Nnt*) gene, which may confound the interpretation of metabolic phenotypes. Loss of function in that gene has been reported to reduce GSIS *in vitro* and lead to a moderately reduced glucose tolerance *in vivo* (127). This suggests that the *in vitro* phenotype is more pronounced compared to the *in vivo* phenotype, and hence, the latter can easily be missed. While the C57BL/6NJ strain resolved some of these issues, it has not been universally adopted. Several studies have addressed the differences between 6J and 6NJ mice, highlighting that the two strains differ in GSIS and glucose homeostasis in general and that those differences cannot be solely attributed to the loss of *Nnt* (128,129). Fergusson *et al.* indicate that 6J and 6NJ mice show no differences in insulin sensitivity, insulin clearance, β-cell mass, or CNS glucose sensing, but 6J mice have intrinsic β-cell secretory defects due to the *Nnt* mutation. Nemoto *et al.* extend these findings by investigating strain differences in terms of differential gene expression beyond *Nnt*. They find that insulin-degrading enzyme (*Ide*) is also among the differentially expressed genes, which potentially explains lower circulating insulin levels in those mice (129). It should be noted that the TAAR1-KO mouse was generated on a mixed background, out of which one is the C57Bl/6J strain, which was crossed with 129S1/Sv (125). Hence, the issues mentioned above for 6J mice likely extend to the TAAR1-KO mice. However, the authors mention that compared to wild-type (WT) littermates, KO mice are normal on several tests and do not show any genotypic differences (125).

2.2 Materials and Methods

2.2.1 Culture and maintenance of mouse insulinoma 6 (MIN6) and α Transformed Cell line 1 (αTC1) clone 9 cells.

MIN6 cells were a kind gift from Dr. Miyazakis's lab (Osaka, Japan). MIN6 cells were cultured in Dulbecco's Modified Eagle's Medium (DMEM) with 4.5 g/L glucose (Gibco, REF# 11965-092) supplemented with 70 μM β-mercaptoethanol (Gibco, REF# 21985-023) before use. Cells were passaged once per week and used within passages 17-30.

αTC1 clone 9 cells (RRID:CVCL_0150) were a kind gift from the lab of Dr. Grompe (Portland, OR, USA). αTC1 cells were cultured in DMEM with 1 g/L glucose (Gibco, REF# 11885084) that was supplemented with 15 mM HEPES (5 mL, Cytivia, REF #AJ30727929), NEAA (10 mL, Gibco, REF #11140-050), and 100 mg BSA (Sigma, REF# A7906). Cells were passaged every three days and used within passages 4-13.

2.2.2 Sample preparation for TA extraction and LC-MS/MS analysis.

MIN6 cells were grown in 60 mm diameter dishes (Nunclon Delta Surface, Thermo Scientific) to form clusters of 70 – 80 % confluence within 5 days after seeding. The growth medium was removed, and cells were washed twice with Dulbecco's Phosphate-Buffered Saline (DPBS) (1 mL) at room temperature (RT). MIN6 cells were pre-stimulated with buffer (1.5 mL) for 60 min at 37 °C, 5 % CO2. For priming of MIN6 cells in advance of the application of respective stimuli, identical buffer glucose concentrations were selected in pre-stimulation and stimulation steps. MIN6 cells were incubated in 1.5 mL buffer (+/- stimulus) for 60 min at 37 °C, 5 % CO2.

Following stimulation, MIN6 cells were scraped in 150 μL of 20 mM 4-(2-hydroxyethyl)-1-piperazineethanesulfonic acid (HEPES) buffer, using disposable cell lifters (Thermo Fisher) and lysed by

pipetting up and down. 50 μL of this were collected for BCA-based protein quantification (Pierce™ BCA Protein assay kit, Thermo Scientific, Rockford, IL, USA). The residual 100 μL were transferred to 2 mL tubes for extraction. 100 μL of 80 % methanol (MeOH) (in H2O), supplemented with 2 % formic acid, was added, and samples were incubated for 30 min at – 80 °C. Samples were concentrated to complete dryness under vacuum at 4 °C, O/N. Isotope-labeled TAs were prepared as stock solutions: β-PEA (2-phenyl-d5-ethylamine, 0.965 mg/mL, ethanol (EtOH)), tryptamine (tryptamine-α,α,β,β-d4, 6.7 mg/mL, EtOH), synephrine (synephrine-13C2, 15N, 100 µg/mL, DMSO), octopamine (octopamine-d3, 1 mg/mL, EtOH), and tyramine (tyramine-d4, 1 mg/mL, EtOH). Stocks were combined to generate a heavy internal standard master mix (1 μg/mL in EtOH (hISDs mix)). Heavy-isotope labeled TAs within this master mix were spiked into samples. Stocks of non-labeled TAs were prepared (2 μg/mL in EtOH), which served as references and quality controls in LC-MS measurements.

Separation of metabolites by liquid chromatography was performed on a Vanquish Ultra-High-Performance Liquid Chromatography (UHPLC) system (Thermo Fisher), equipped with a Luna Omega Polar C18 column (1.6 µm, 100x2.1 mm) at a flow of 0.26 mL/min and at 40 °C. Mobile phase A consisted of 7.5 mM ammonium acetate, supplemented with 0.02 % formic acid (pH 4). Mobile phase B consisted of 7.5 mM ammonium acetate in acetonitrile:H2O (95:5). The applied gradient for MeOH/HCl extracted samples is listed in Table 1. Extracted samples were re-suspended in 100 µL mobile phase A. Samples were vortexed (10 s) and centrifuged at maximum speed for 2 min at RT. 100 µL of the clear supernatant (SN) was injected for analysis. Mass spectrometry (MS) was performed on a Q-Exactive Plus (Thermo Fisher) high-resolution mass spectrometer (HRMS), equipped with an advanced hybrid quadrupole-Orbitrap. Ionization was achieved by electrospray ionization (ESI-MS) in positive mode (spray voltage: 4 kV). Spectra were acquired as full scans (60 - 900 m/z) with a resolution of 35000 (detailed parameters are listed in Table 2). The collected LC-MS data were evaluated using the Xcalibur software tool (Thermo Fisher).

Table 1: Applied gradient for LC-MS analysis of TA extracts. Mobile phase A consisted of 7.5 mM ammonium acetate, supplemented with 0.02 % formic acid (pH 4), mobile phase B of 7.5 mM ammonium acetate in acetonitrile:H2O (95:5).

Time (min)	% of mobile phase B
0.0	5
1.0	5
7.0	54
8.0	90
11.0	90
11.5	5
14.0	5

Table 2: MS parameters for TA detection.

ESI mode	positive
Scan range	Full scan (60-900 m/z)
Resolution	35,000
Spray Voltage	4 kV
S-lens RF level	65/75
Auxiliary gas	5
Capillary temperature	300 °C
Probe heater temperature	320 °C
Injection volume	20 μL

2.2.3 Hormone secretion analysis from MIN6 cells by ELISA.

Experiments for the determination of insulin secretion were performed in triplicate /_condition. Cells were washed 1 x with DPBS and equilibrated by incubation for 1 h at 37 °C, 5 % CO2 in KRHB + 2.8

mM glucose (pre-incubation). Cells were then transferred to fresh buffer (Krebs Ringers HEPES Buffer (KRHB) + 2.8 mM (basal) or 22.2 mM (stimulated)) glucose for 1 h at 37 °C, 5 % CO2. After incubation, buffers were collected and stored at 4 °C for subsequent ELISA analysis (Promega, Lumit, Insulin Kit REF#CS3037A05 and Glucagon Kit REF#W8020). Additionally, total human insulin content was measured from an aliquot of Radioimmunoprecipitation Assay Buffer (RIPA)-lysed (RIPA, ThermoFisher REF# 89900 + Protease Inhibitors, cOmplete™ Protease Inhibitor Cocktail tablets, Sigma, REF# 11697498001) cells by ELISA (Promega, Lumit). Statistical analyses of the results were performed using Graphpad Prism 10.5 (for analysis of variance tests) and Microsoft Excel (for mean and standard deviation).

2.2.4 Confocal laser scanning microscopy and Ca^{2+} dynamics analysis in MIN6 cells.

Live cell imaging was performed on a FluoView1200 (Olympus IX83) confocal laser-scanning microscope, equipped with an environment box (custom-made at EMBL) to allow imaging at 37 °C and 5 % CO2. Olympus 60x Plan-APON (NA 1.4, oil) or 20x UPLS APO (NA 0.75, air) objectives and FluoView software (version 4.2) were applied. Images were acquired using a Hamamatsu C9100-50 EM CCD camera. A 488 nm laser line (120 mW/cm2, 2.5 %) in combination with a 525/50 emission mirror was used to image the green channel. A 559 nm laser line (120 mW/cm2, 2.0%) and a 643/50 emission filter were used for red channel recordings. For monitoring Ca^{2+} dynamics in response to external stimuli, cells were incubated with the acetoxymethyl ester of the Ca^{2+} indicator Fluo-4 (Life Technologies, Eugene, OR), 5 μM in DMEM (1 g/L glucose) for 20 min at 37 °C and 5 % CO2. The frame time was set to 3.9 s, with images acquired in 4 s intervals. For imaging, MIN6 cells were grown as clusters of ~ 70 % confluence. Imaging experiments were performed in HEPES buffer (in mM: 115 NaCl, 1.2 CaCl2, 1.2 MgCl2, 1.2 K2HPO4, and 20 HEPES, pH 7.4).

2.2.5 Reverse-Transcription PCR (RT-PCR) for TAAR1 in MIN6 and αTC1 clone 9 cells.

Total RNA was extracted from confluent MIN6 and αTC1 clone 9 cells (culture conditions as in Section 2.2.1) using Trizol. RNA integrity was verified by A260/280 and agarose electrophoresis. cDNA was synthesized from 1 μg total RNA using random primers mix and RevI (Thermo). PCR targeted mouse Taar1 using intron-spanning primers (forward 5′- ACTCTTCACCAAGAATGTGG-3′; reverse 5′-CCAACAGCGCTCAACAGTTC-3′; amplicon ~ 149 bp) with 30 cycles (95 °C 30 s, 58 °C 30 s, 72 °C 30 s). Amplicons were resolved on 2 % agarose with SYBR Safe and visualized under UV/blue light. HeLa Kyoto cells served as a negative control, and TAAR1 plasmid DNA served as a positive control.

2.2.6 Stable transfection of hTAAR1 in HEK293T cells.

HEK293T cells stably expressing human TAAR1 were kindly provided by the lab of Dr. Janowsky. Briefly, the cells were generated as described by Harkness et al. (130). There, a plasmid encoding human TAAR1 cDNA with a C-terminal monomeric green fluorescent protein (mGFP) tag (RC211034L4, OriGene, Rockville, MD) was transformed into Stbl2 competent E. coli (Invitrogen, Grand Island, NY). Transformed E. coli were selected in 34 µg/mL chloramphenicol (Sigma, St. Louis, MO), and plasmid DNA was prepared using the Qiagen miniprep kit (Qiagen, Valencia, CA) after transformation. The sequence was verified with the primers V2-F (5' AGCAGAGCTCGTTTAGTGAACC 3') and LR50 (5'CAGAGGTTGATTATCGATAAG 3'). The purified expression plasmid was transfected into HEK293T cells using polyethylenimine (PEI)-mediated transfection (1 µg/mL; PEI:DNA = 1:2). Cells stably expressing TAAR1 were selected in 2 µg/mL puromycin (Sigma). The cells were maintained under constant selection in DMEM (4.5 g/L glucose) + 10 % FCS + 1 % P/S + 2 μg/mL puromycin.

2.2.7 TAAR1-KO animals.

TAAR1 KO mice were kindly provided by the lab of Dr. Janowsky. The KO mice (C57BL/6 background) were obtained from the UC Davis Knockout Mouse Project (130). TAAR1 KO mice were generated by

complete deletion of the entire coding region of the mouse TAAR1 gene using procedures described by Poueymirou *et al.* (131). Mouse breeding and genotyping were performed as previously described (130). Mice (10–20 weeks old) of both sexes were used in this study, and TAAR1 KO mice and WT C57BL/6 littermate control mice were age- and sex-matched in all experiments.

Mice were group housed in filtered polycarbonate cages (28 cm × 18 cm × 13 cm) on ECO-Fresh bedding (Absorption Corporation, Ferndale, WA) with *ad libitum* access to water and rodent chow (5LOD, 5.0 % fat content; Purina Mills, St. Louis, MO). Housing was maintained at 21±1 °C with a 12-hour light/dark schedule. All procedures were conducted following the National Institutes of Health Guide for the Care and Use of Laboratory Animals, and with approval by the Veterans Affairs Portland Health Care System Institutional Animal Care and Use Committee.

2.2.8 Analysis of cAMP levels in HEK293T cells transfected with hTAAR1.

cAMP accumulation in hTAAR1 KO and knock in (KI) HEK293T cells was measured using the Cayman cAMP assay kit (Cayman Chemical, 581001). Cells (2×10^5/well) were seeded in 48-well plates in triplicate/condition. After O/N attachment, cells were serum-starved in medium supplemented with charcoal-stripped FCS O/N.

The assay buffer consisted of 1× EBSS supplemented with 0.2 mg/mL ascorbic acid, 15 mM HEPES, 1.3 mM $CaCl_2$, 1.2 mM $MgSO_4$, 22 mM glucose, and 0.5 mM 3-isobutyl-1-methylxanthine (IBMX) (added last from dimethyl sulfoxide (DMSO) stock). Buffer was adjusted to pH 7.4 and prewarmed to 37 °C. Cells were washed and preincubated with assay buffer for 15–20 min at 37 °C, followed by stimulation with drug dilutions (10^{-4} to 10^{-7} M, log scale) prepared in 1× Earle's Balanced Salt Solution (EBSS). Forskolin (10 μM) served as a positive control. After 1 h at 37 °C, the media was removed and 40 μL of 3 % trichloroacetic acid (TCA) was added for lysis. Plates were wrapped in foil and rocked for ≥ 2 h at RT or overnight at 4 °C.

ELISA standards were prepared according to the manufacturers' instructions. TCA-treated samples were diluted 1:5 in Enzyme Immunoassay (EIA) buffer directly in the 48-well plate and transferred (50 μL/well) to the ELISA plate together with standards. Tracer and antiserum (50 μL/well each) were added to a total volume of 150 μL/well. Plates were sealed, wrapped in foil, and incubated overnight (O/N) at 4 °C. The following day, plates were washed five times with buffer containing 0.05 % Tween and developed with Ellman's reagent (2.5 mg/mL in ddH_2O, freshly prepared). Plates were incubated for 2 h at RT in the dark and then read at 410 nm.

2.2.9 Pancreatic islet isolation from TAAR1-KO and WT littermate mice.

Pancreatic isolation surgery was performed by Dr. J. Huey (Janowsky lab). Mice of both genotypes were euthanized by cervical dislocation, and the pancreas was excised following injection of collagenase solution (1 mg/mL) into the pancreatic duct. Tissue was digested at 37 °C for 13 min, and islets were isolated by density gradient centrifugation using Histopaque (1.083 and 1.119 g/mL; 20 min, 2000 rpm, RT). Islets were handpicked under light microscopy and recovered O/N in Roswell Park Memorial Institute (RPMI) medium supplemented with 10% FBS, 100 U/mL penicillin, and 100 mg/mL streptomycin. Recovered islets were dissociated into single cells using 0.05 % Trypsin-ethylenediaminetetraacetic acid (EDTA). Once dissociation was confirmed by light microscopy, cells were pelleted, resuspended in ice-cold medium, and mixed with Matrigel (1:10 of medium volume). Cells were seeded onto poly-L-lysine–coated 8-well microscopy dishes, allowed to settle for 45 min at 37 °C, 5 % CO_2, then overlaid with 400 μL medium and recovered O/N under the same conditions.

2.2.10 Confocal laser scanning microscopy and Ca^{2+} dynamics analysis in isolated mouse islets from WT and TAAR1-KO mice.

Calcium dynamics in dispersed mouse pancreatic cells were assessed using the Ca^{2+}-sensitive dye Fluo4-AM (Invitrogen, 5 μM). Cells were incubated in staining medium containing 5 μM Fluo4-AM and

1 g/L glucose for 20 min at 37 °C, 5% CO_2, followed by washing and transfer to imaging solution containing 11 mM glucose.

Imaging was performed under controlled environmental conditions (37 °C, 5% CO_2, ~ 30% humidity). Cells were visualized using epifluorescence at 20 × magnification and excited with a 488 nm laser. Acquisition parameters were: look-up table (LUT) set to Hi/Lo with range at 50 %, background offset adjusted to blue, pinhole opened to ~ 250 μm, and frame time 3.9 s. A total of ~ 300 frames/stimulus were collected.

Stimuli were applied as 10 × stock solutions to achieve a 1:10 final dilution, and the exact frame of addition was recorded (relevant for data analysis). At the end of each experiment, 5 μM ionomycin was added to determine the maximal dye response (100 % output). To identify β-cells, dithizone (DTZ) solution was applied to the same field of view for 10 min. Only red cells were used for data analysis, which correspond to β-cells due to zinc chelation by DTZ.

2.2.11 Confocal laser scanning microscopy and Ca^{2+} dynamics analysis in human-donor-derived pseudo-islets.

See section 2.2.10

2.2.12 Ca^{2+} dynamics analysis software.

Ca^{2+} dynamics data were processed using a customized Python script (available at DOI: 10.5281/zenodo.17526692). For this, selected region(s) of interest (ROIs) were normalized to the background, generating F/F_0 data. This data was then normalized to the baseline = to Ca^{2+} dynamics before stimulus addition. Once normalized, the tool proceeded with automated peak/spike detection and visualization for user verification to confirm capture of biologically relevant signals. Additionally, it performed outlier removal (*e.g.*, exclusion of cells showing monotonic increases or decreases indicative of cell death), and quantitative peak counting. A Ca^{2+} peak (or spike) was defined as a maximum in fluorescence

intensity flanked by two minima. For each defined period (*e.g.,* baseline, first stimulation, second stimulation, etc.), the number of peaks was quantified, allowing comparisons across conditions. The analyzed ROIs were exported as .csv files and visualized using GraphPad Prism (10.5) as Oscillation Counts/Conditions tested.

2.3 Results

2.3.1 Detection and Functional Characterization of Endogenous TAs in Pancreatic β-Cells

As reported previously (103), and shown in Fig. 9g for our model cells (MIN6), pancreatic β-cells express TAAR1. It has further been suggested that TAAR1 may contribute to the regulation of insulin secretion, although the precise mechanism underlying this effect remains unresolved. Prior studies investigating TAAR1 function have largely employed synthetic agonists such as RO5166017, rather than the receptors' endogenous ligands, the TAs. In the present study, we aimed to determine whether TAs can induce a response through pancreatic TAAR1 and whether such a response impacts insulin secretion from these cells. Additionally, we investigated the availability of TAs within the pancreatic microenvironment to assess their potential role as endogenous ligands. To address this, we employed tandem mass spectrometry (LC-MS/MS) in combination with stable isotope-labeled amino acid precursors (^{15}N-phenylalanine, tryptophan, and tyrosine) to determine whether ^{15}N-TA would be detectable, indicating that the biosynthetic machinery for TA production is present within β-cells.

The TA family encompasses a broad range of biogenic amines, including several compounds that are commonly referred to as the TA family: β-phenylethylamine (PEA), p-tyramine (TYR), tryptamine (TRYP), synephrine (SYN), and octopamine (OCT). Most of these are synthesized in a single enzymatic step catalyzed by aromatic amino acid decarboxylase (AADC). However, OCT and SYN require an additional enzymatic reaction catalyzed by dopamine β-hydroxylase (DBH), which hydroxylates TYR to OCT and PEA to SYN.

To investigate whether TAs are available in the environment of pancreatic β-cells and could hence function as endogenous ligands for TAAR1, we cultured MIN6 cells in a medium depleted of L-tyrosine, L-tryptophan, and L-phenylalanine. These amino acids were substituted with their stable isotope-labeled versions: ^{15}N-phenylalanine, ^{15}N-tryptophan, and ^{15}N-tyrosine (all in L-isoform), which serve as

direct substrates for AADC (Fig. 8a). Under these conditions, detection of ^{15}N-labeled TAs would indicate that the biosynthetic pathway is active in β-cells.

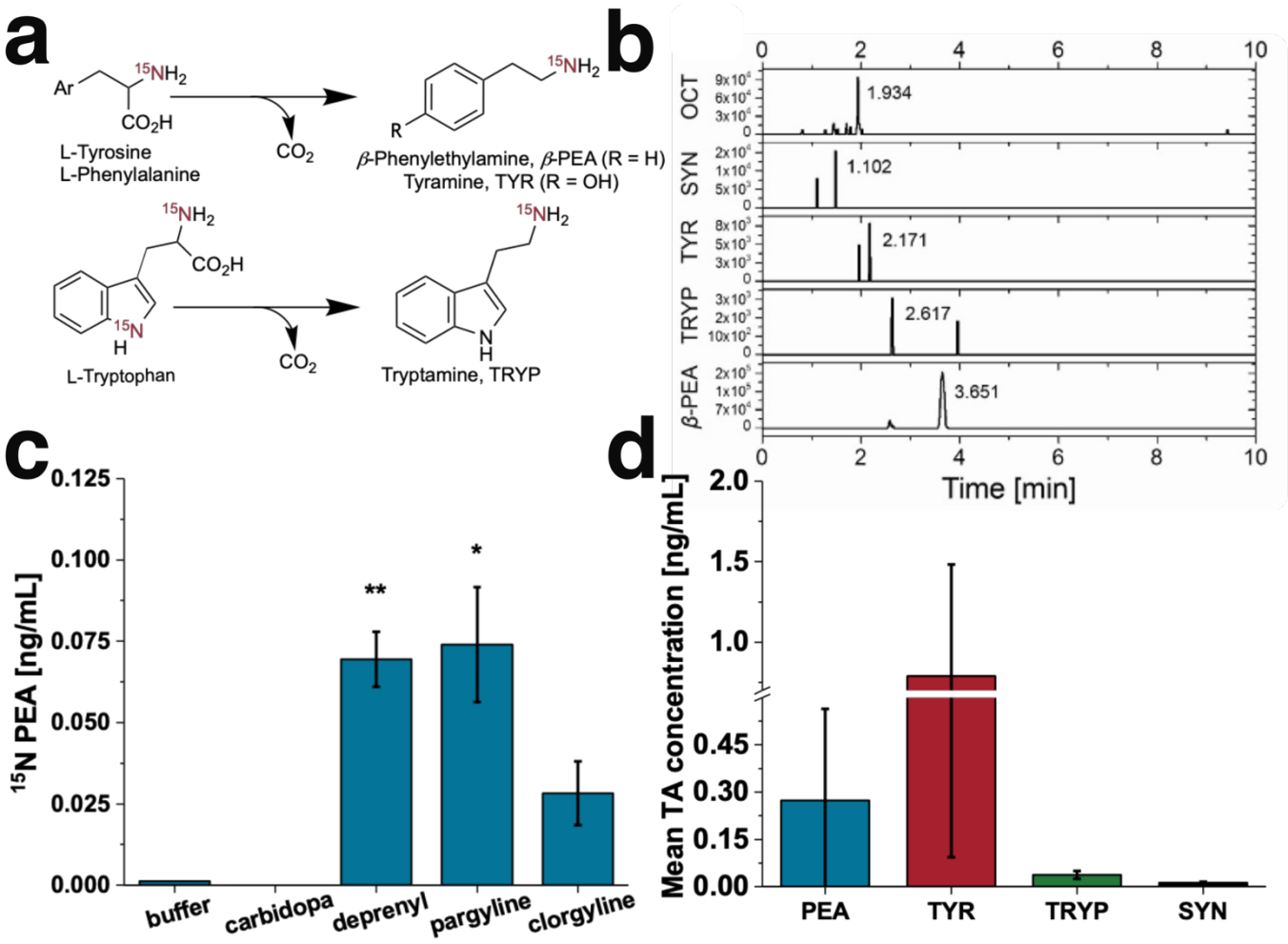

Figure 8: MIN6 cells possess the necessary pathways for trace amine biosynthesis and degradation. (**a**) Trace amines (TAs) originate from precursor amino acids and are formed by decarboxylation catalyzed by the enzyme aromatic amino acid decarboxylase (AADC). Providing MIN6 cells with ^{15}N-labelled versions of those precursor amino acids is expected to lead to the formation of ^{15}N-labeled TAs. (**b**) LC-MS/MS results visualized as intensity over time (min) with the respective retention time highlighted for each TA peak detected. (**c**) ^{15}N-PEA levels in ng/mL as detected by LC-MS/MS in control (buffer only) conditions or in the presence of carbidopa (biosynthesis inhibition), selegiline/deprenyl (monoamine oxidase B (MAO-B)inhibition), pargyline (both MAO-A and MAO-B inhibition), and clorgyline (MAO-A inhibition), each sample measured in quadruplicates. (**d**) mean TA concentration in ng/mL as detected from MIN6 cells for PEA (n = 3), TYR (n = 4), TRYP (n = 2), and SYN (n = 2) with n being the number of biological replicates for each TA. Two-way ANOVA was used for statistical analysis. Error bars refer to standard deviation (SD). Only statistically significant differences are marked (cut off for statistical significance is p = 0.05) with * = $p \leq 0.05$, and ** = $p \leq 0.01$.

Following MeOH-based extraction for cell SN and cell pellets, LC-MS/MS analysis revealed detectable levels of all investigated ^{15}N-labeled TAs (Fig. 8b). Additionally, unlabeled TAs were present in MIN6

cells, further supporting their availability in the β-cell environment and their potential role as endogenous TAAR1 ligands (Fig. 8d).

To further characterize TA metabolism, we examined changes in ^{15}N-PEA levels under pharmacological modulation of TA biosynthesis and degradation. Specifically, we applied the AADC inhibitor carbidopa as well as inhibitors of monoamine oxidase (MAO), the principal enzyme responsible for TA degradation. MAO exists in two isoforms with distinct substrate preferences: MAO-B preferentially degrades PEA and, to a lesser extent, TYR (which can also be metabolized by MAO-A), whereas MAO-A primarily targets other TAs. Both isoforms are expressed in the pancreas; however, MAO-B is enriched in the endocrine pancreas, particularly in β-cells, while MAO-A is more broadly distributed within the exocrine pancreas (132–135). Importantly, inhibition of MAO-B by selegiline (deprenyl) has been reported to specifically hinder PEA degradation (132). We find that buffer levels of ^{15}N-PEA are low (>> 0.1 nM) and become undetectable under carbidopa addition. However, MAO inhibition resulted in a marked increase in ^{15}N-PEA levels, reflecting the inhibitor selectivity. The strongest elevations were observed with selegiline/deprenyl and pargyline (~ 0.075 ng/mL, ~ 0.6 nM), whereas clorgyline treatment (MAO-A selective) led to an approximate 60 % reduction in detectable ^{15}N-PEA (~ 0.025 ng/mL, ~ 0.2 nM) (Fig. 8c).

2.3.2 Glucose- and Concentration-Dependent Effects of TAs on Insulin Secretion in Pancreatic β-Cells

To test the functional impact of TAs on β-cell activity, we selected PEA and TYR as exemplary ligands, as these were detected as the most abundant TAs in our system (~ 0.3 ng/mL or 2.5 nM for PEA and ~ 0.9 ng/mL or 6.6 nM for TYR; Fig. 8d).

We performed two sets of experiments: 1) we fixed the TA concentration at 10 μM and varied the glucose concentration (3, 5, 11, and 22 mM glucose), and 2) fixed the glucose concentration at 11 mM

and varied the TA concentration (0.01, 1, 10, 25, 50, and 100 μM). The first approach allowed us to test whether TA stimulation of TAAR1 is glucose-dependent, while the second provided dose-response relationships (see Fig. 9 a_i and a_{ii}).

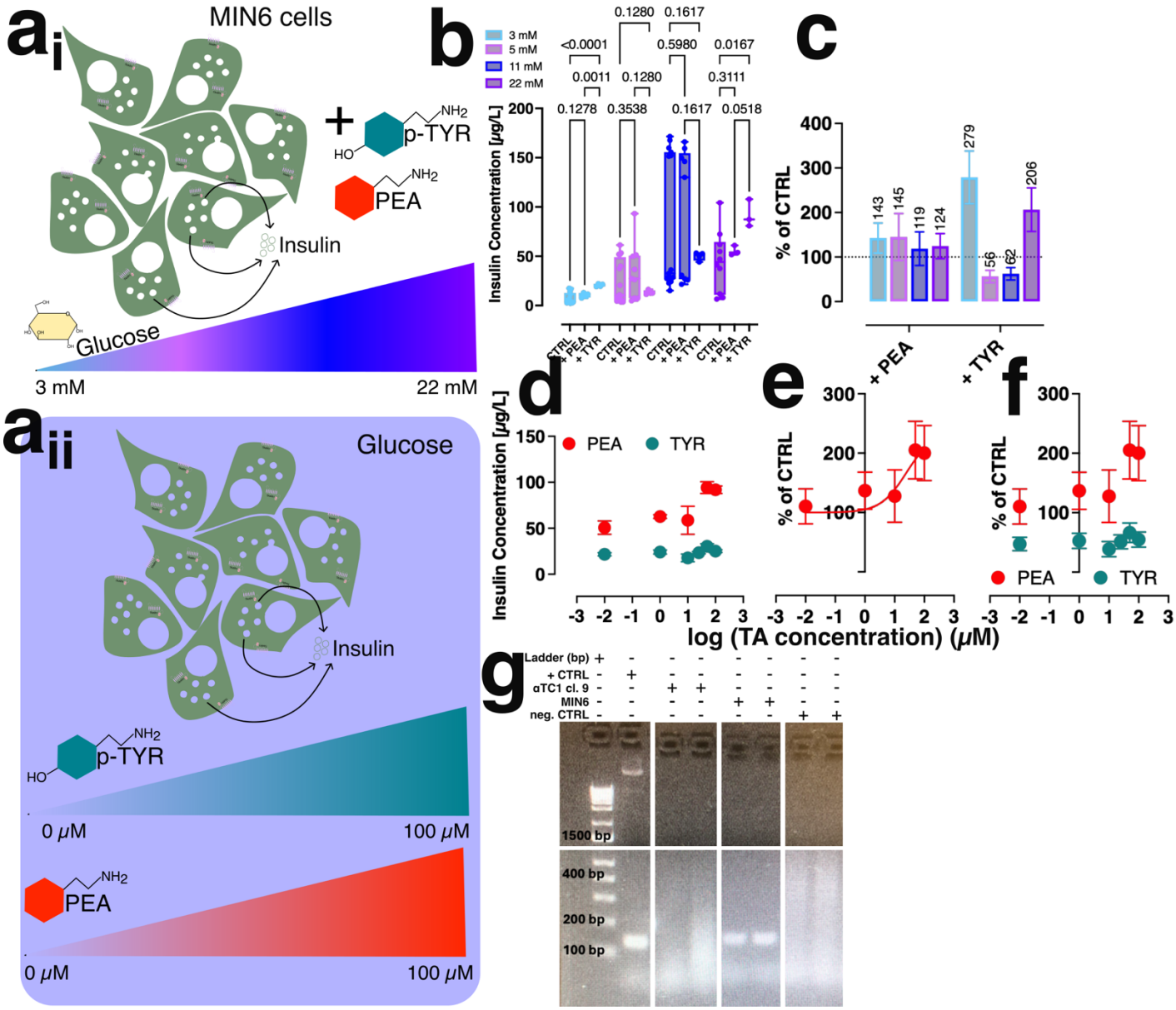

Figure 9: TAs influence insulin secretion from MIN6 cells in a glucose-dependent manner. (**a_i and a_{ii}**) experimental approaches to test glucose dependence of TA administration (a_i) and TA dose-response (a_{ii}). (**b**) Secreted insulin levels expressed in μg/L for control (CTRL), PEA, and TYR at 3 mM (light blue), 5 mM (pink), 11 mM (dark blue), and 22 mM (purple) glucose with a constant TA concentration of 10 μM. (**c**) insulin secretion expressed as % of control (CTRL) with control being different glucose concentrations without added TA, plotted for PEA and TYR at 3 mM (light blue), 5 mM (pink), 11 mM (dark blue), and 22 mM (purple) glucose, with a constant TA concentration of 10 μM. The dotted line indicates 100 % or the control level, and numbers above bars indicate the mean percentage/condition. (**d**) Secreted insulin levels expressed in μg/L at 11 mM glucose for a concentration range (x-axis expressed as log of concentration in μM) for PEA (red) and TYR (teal). (**e**) insulin secretion levels expressed as % of control (buffer without TA) for PEA (red). The red line represents the 3PL curve fit applied to the data. (**f**) insulin secretion levels expressed as % of control (buffer without TA) for PEA (red) and TYR (teal), x-axis is log of concentration in μM. (**g**) agarose gel results of RT-PCR for TAAR1 in MIN6 cells, αTC1 cl. 9, and HeLa cells (neg. CTRL) with the TAAR1 plasmid as pos. CTRL. Experiments described in a_i and a_{ii} were conducted using four biological replicates, each assayed in quadruplicate technical replicates. Statistical analysis was performed using two-way ANOVA with the

Benjamini-Hochberg correction for multiple comparisons. Error bars reflect the standard error of the mean (SEM). All p-values are shown, but the cutoff for statistical significance is at 0.05.

In glucose-titration experiments, administration of exogenous TAs modulated insulin secretion in a glucose-dependent manner. PEA did not significantly differ from buffer controls but consistently trended above baseline when expressed as a percentage of control (143 % at 3 mM, 145 % at 5 mM, 119 % at 11 mM, and 124 % at 22 mM glucose; Fig. 9b and c). TYR, in contrast, exerted a pronounced and biphasic effect: insulin secretion was strongly elevated at 3 and 22 mM glucose (279 % and 206 %, respectively), but was markedly reduced at intermediate glucose concentrations (56 % at 5 mM and 62 % at 11 mM; Fig. 9b and c). These findings suggest that both PEA and TYR act as context-dependent modulators of insulin secretion, with stimulation occurring at extreme glucose concentrations and suppression or attenuation at physiological mid-range levels.

In the dose–response experiments at 11 mM glucose, the outcomes diverged from those observed under glucose titration. PEA elicited increased insulin release (measured in μg/L) across all concentrations tested, with a plateau evident at 50–100 μM (Fig. 9d). When normalized to control (buffer without TA), PEA responses were close to baseline at lower concentrations and exceeded 100 % at higher concentrations (110 % at 0.01 μM, 137 % at 1 μM, 128 % at 10 μM, 205 % at 50 μM, and 200 % at 100 μM) (Fig. 9e and f). Given the curve shape, a three-parameter logistic (3PL) fit was applied, constraining the bottom to 100 %. The resulting fit yielded an apparent EC_{50} of ~ 25 μM (24.73 μM), with a curve top of ~ 234 %, indicating that maximal PEA stimulation produced a ~ 2.3-fold increase over baseline insulin output.

TYR, in contrast, behaved differently. Insulin secretion values were consistently below control across all tested concentrations (expressed as % of control: 47 % at 0.01 μM, 53 % at 1 μM, 39 % at 10 μM, 51 % at 25 μM, 66 % at 50 μM, and 55 % at 100 μM), resulting in an almost flat dose–response curve (Fig. 9d and f). Due to the lack of dose-dependent changes, curve fitting was not performed.

2.3.3 Pharmacological Characterization of TAAR1 Activation and Functional Validation in Human β-Cells

Given the number of biogenic amine receptors expressed on pancreatic β-cells, there is potential for off-target effects, particularly at higher TA concentrations. To address receptor specificity at the level of human TAAR1, and in recognition of the species-dependent differences discussed earlier, we employed HEK293T cells engineered either with TAAR1 knockout (KO) or knock-in/overexpression (KI), generously provided by Dr. J. Huey (Janowsky lab).

To test for TAAR1 activation, we measured intracellular cAMP accumulation as a downstream readout (Fig. 10a). As expected, TAAR1-KO cells exhibited lower cAMP responses compared with TAAR1-KI cells, consistent with TAAR1 activation driving cAMP production. Test compounds included the endogenous TAs PEA, p-TYR, and OCT (Fig. 10d), as well as the synthetic full agonist RO5256390 (Roche, Fig. 10b and c). In addition, the precursor amino acids L-tryptophan, L-tyrosine, and L-phenylalanine were used as negative controls (Fig. 10e).

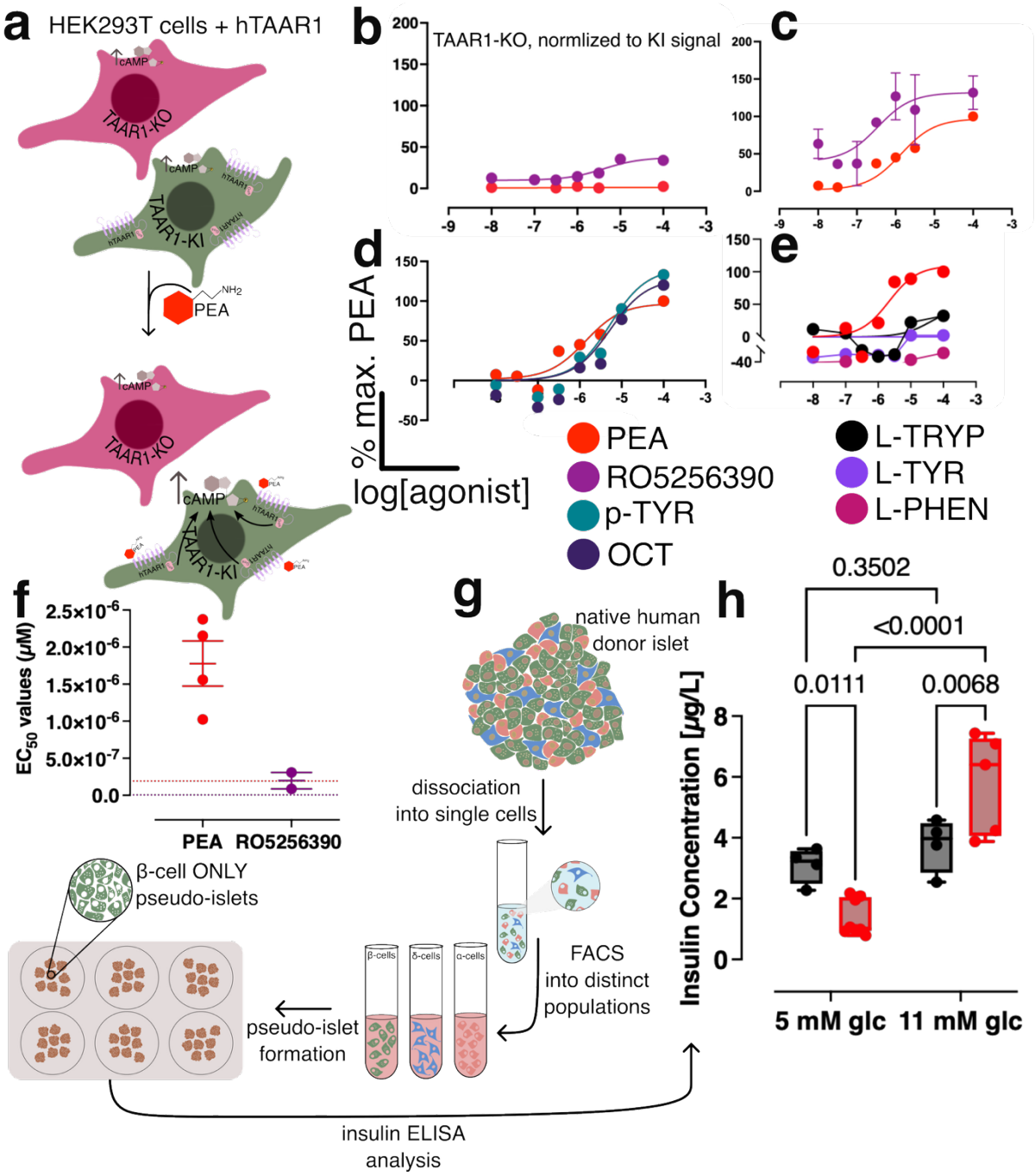

Figure 10: Trace amines show receptor specificity for human TAAR1 and maintain their effect on insulin secretion in human-donor-derived β-cells. (**a**) Experimental overview with HEK293T cells overexpressing hTAAR1 vs. TAAR1-KO cells. This system was used to test TA receptor specificity with cAMP production as read out. (**b-e**) Dose-response curves with % of maximal PEA response on the y-axis and log of TAAR1 agonist in μM on the x-axis. PEA (red) was used as the reference curve; p-TYR (teal), RO5256390 (purple), and OCT (dark blue) were also tested as TAAR1 agonists. L-TRYP (black), L-TYR (violet), and L-PHEN (bordeaux), TA precursor amino acids served as negative controls. (b) shows cAMP signal derived from TAAR1-KO cells, and (c-e) show signal derived from TAAR1-KI/OE cells. (**f**) estimated EC_{50} values for PEA (red) and RO5256390 (purple) based on 3PL fit of the dose-response curves in (c). Dashed lines of the respective colors correspond to the literature-reported EC50 values of ~ 193 nM (red) and 5.3 nM (purple), both for hTAAR1. (**g**) schematic overview of how the human-donor-derived β-cell pseudo-islets were obtained. (**h**) Insulin concentration in μg/L measured by ELISA from SN of β-cell only pseudo-islets generated as described in (**f**) for 10 μM PEA (red) vs. buffer control (black) at 5 mM and 11 mM glucose. Two-way ANOVA was used for statistical analysis with Benjamini-Hochberg correction for multiple comparisons. P-values are indicated on the graph; the cutoff for statistical significance was 0.05. Error bars reflect SEM.

Dose-response curves were graphed as % of maximal response to PEA (y-axis) and log of agonist concentration in μM (x-axis) (Fig. 10b-e). In TAAR1-KI cells, endogenous TAs and RO5256390 produced sigmoidal dose–response curves across the tested concentrations. Using PEA as the reference agonist, RO5256390 demonstrated a leftward and upward shift, consistent with higher potency and efficacy (Fig. 10c). In contrast, p-TYR and OCT exhibited rightward shifts relative to PEA, with modest upward shifts in maximal response at higher concentrations (Fig. 10d). Sigmoidal dose-response curves were fit with a three-parameter logistic (3PL) curve with x = log(agonist) and the EC_{50} values for both PEA and RO5256390 could be estimated based on the fit. The estimated EC_{50} for PEA was 1.77 μM ± 3.049 x 10^{-7} with an E_{max} of ~ 98 %, whereas the estimated EC_{50} for RO5256390 was 0.197 μM ± 1.110 x 10^{-7} with an Emax of ~ 131 % relative to PEA (Fig. 10f). In TAAR1-KO cells, neither PEA nor RO5256390 produced a sigmoidal response, instead yielding flat curves consistent with loss of TAAR1 engagement (Fig. 10b). Likewise, precursor amino acids failed to induce a sigmoidal curve in TAAR1-KI cells, confirming their inability to activate TAAR1 (Fig. 10e).

These findings establish a receptor-specific pharmacological profile in a simplified system (HEK293T cells), which contrasts with the more complex, glucose-dependent outcomes observed in β-cells, highlighting the influence of cellular context on TAAR1-mediated signaling. Because HEK293T cells do not provide a physiologically relevant context for insulin secretion, we extended these findings to human donor-derived β-cells, aggregated into islet-like structures (workflow shown in Fig. 10g). In this system, PEA significantly increased insulin secretion at 11 mM glucose relative to buffer control (~ 143 % of CTRL), whereas at 5 mM glucose, PEA apparently suppressed insulin secretion compared to buffer (~

47 % of CTRL) (Fig. 10h). Within each condition, glucose concentration increase from 5 to 11 mM led to an increase of insulin secretion by ~ 22 % for CTRL and ~ 270 % for + PEA (Fig. 10h).

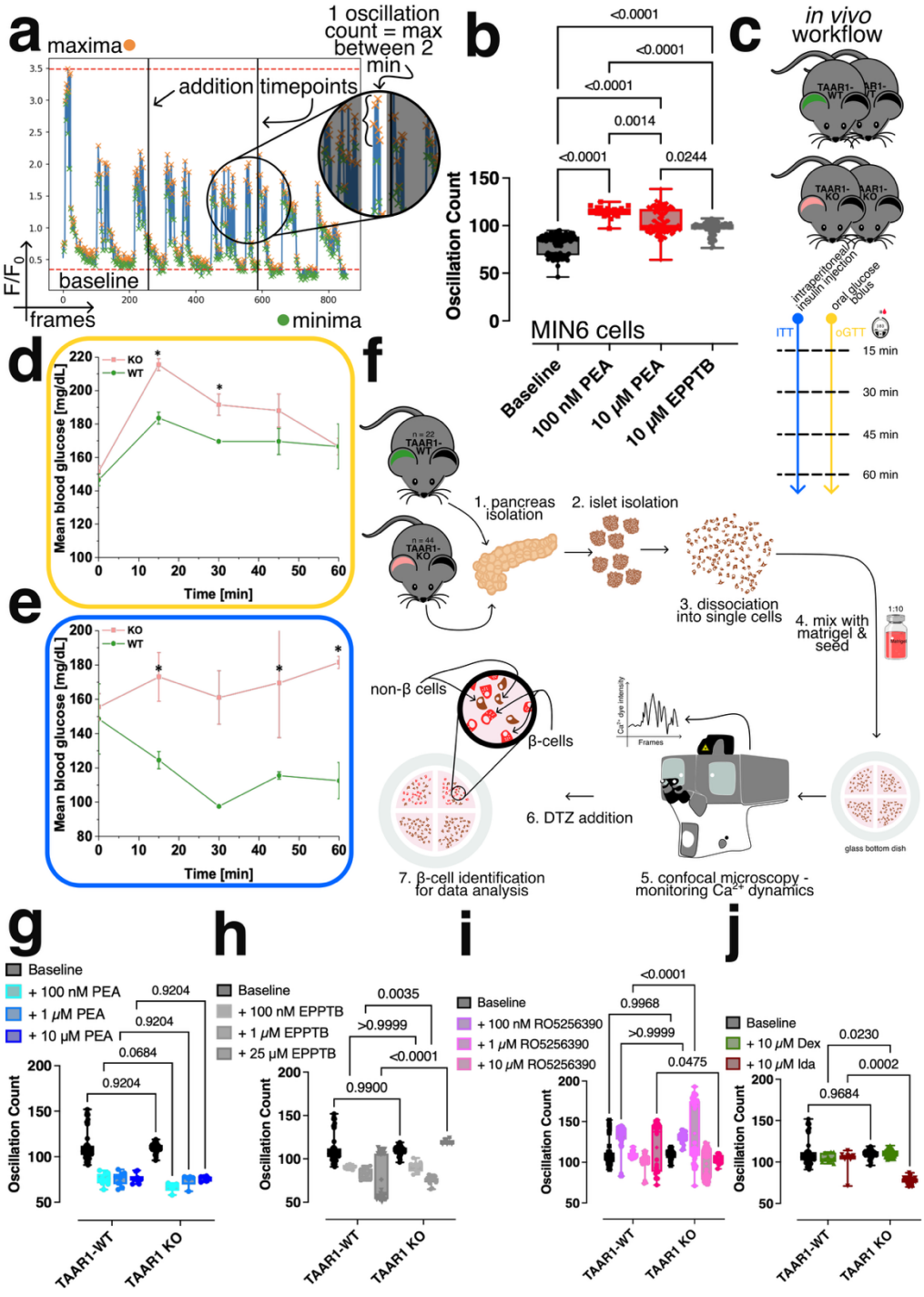

Figure 11: *In vivo* glucose tolerance and insulin sensitivity, and *ex vivo* Ca^{2+} dynamics as a proxy for insulin secretion. (**a**) Exemplary Ca^{2+} dynamics plot generated using a custom-written analysis script. The script identifies maxima (orange) and minima (green) of normalized fluorescence intensity (F/F_0) and transforms these into oscillation counts for each stimulation period. One oscillation count corresponds to a single maximum flanked by two minima. (**b**) Mean oscillation counts in MIN6 cells exposed to 100 nM or 10 μM PEA (red) compared with 10 μM EPPTB, a selective TAAR1 antagonist (grey), and baseline (5 mM glucose only, black). (**c**) To evaluate TAAR1s' role in systemic glucose homeostasis, glucose tolerance tests (GTT, yellow) and insulin tolerance tests (ITT, blue) were performed in TAAR1-KO and WT littermate C57BL/6J mice. For each test, a bolus of glucose or insulin was administered at T0, followed by blood glucose measurements every 15 min using a handheld glucometer. Assays were terminated at 60 min. (**d, e**) GTT and ITT curves comparing TAAR1-KO (pink) and WT (green) mice, with mean blood glucose concentration plotted over time. (**f**) Workflow schematic depicting *ex vivo* Ca^{2+} imaging experiments in dissociated primary islet cells from C57BL/6J WT and TAAR1-KO mice, under TAAR1-specific stimulation. Data analysis was performed with DTZ+ = β-cells only. (**g-i**) Concentration-dependent effects of PEA (100 nM (cyan), 1 μM (blue), and 10 μM (cobalt)), EPPTB (100 nM (silver), 1 μM (aluminum), and 25 μM (tin)) and the TAAR1 agonist RO5256390 (100 nM (lavender), 1 μM (light pink), and 10 μM (pink)) compared to baseline (black). (**j**) Positive control experiments targeting ADRA2 signaling with the agonist dexmedetomidine (10 μM, green) and antagonist idazoxan (10 μM, brown). Statistical analyses were performed using two-way ANOVA or mixed-effect models where applicable, with a significance threshold of $p < 0.05$. p-values are reported on the graphs. Error bars indicate SEM; * denotes $p < 0.01$.

2.3.4 *In Vitro* and *In Vivo* Analyses of TAAR1-Dependent Ca^{2+} Signaling and Glucose Regulation

Observing Ca^{2+} dynamics in response to exogenous stimuli is an established proxy for insulin secretion in the field of β-cell research (136). In this study, we employed Ca^{2+} dynamics as an additional functional readout, complementing hormone-specific ELISA assays, to determine whether TAs influence insulin release from β-cells.

Given the large volume of data generated by this approach (≥100 cells per field of view over multiple frames), we implemented a standardized analysis pipeline to reduce user bias and ensure reproducibility. Specifically, we developed a custom script that performed background subtraction, baseline normalization (normalization to Ca^{2+} dynamics before stimulus addition, F/F_0), automated peak/spike detection and visualization for user verification to confirm capture of biologically relevant signals, outlier removal (*e.g.*, exclusion of cells showing monotonic increases or decreases indicative of cell death), and quantitative peak counting. A Ca^{2+} peak (or spike), which has been shown to coincide with a burst of insulin release (30,137,138), was defined as a maximum in fluorescence intensity flanked by two minima (see example in Fig. 11a). For each defined period (*e.g.,* baseline, first stimulation, etc.), the number of peaks was quantified, allowing comparisons across conditions. In MIN6 cells, we observed a mean of 80 (±1.035) Ca^{2+} peaks at baseline (11 mM glucose). Upon addition of PEA (red), the number of spikes increased to 115 (± 1.181) for 100 nM PEA, and 104 (± 1.215) for 10 μM PEA, corresponding to ~ 44 % and ~ 30 % increases, respectively. In contrast, addition of the TAAR1 antagonist EPPTB (10 μM, grey) reduced the number of peaks relative to PEA stimulation, though not compared with baseline (97 ± 0.6153) (Fig. 11b).

Finally, we investigated the effect of TAs on TAAR1 *in vivo* using TAAR1-KO mice generated in the Janowsky lab (VA). With the assistance of Dr. J. Huey, Dr. T. Phillips, and Dr. D. Hegarty, we performed both live animal experiments and *ex vivo* studies on isolated primary islets from TAAR1-KO and WT littermates (Fig. 11c and f). Our *in vivo* cohort was relatively small (n = 8, 4 per genotype), whereas the

ex vivo analysis of Ca^{2+} dynamics included a substantially larger dataset (44 KO and 22 WT animals, spanning both sexes and a range of ages).

For the *in vivo* approach, we studied 12-week-old male mice and subjected them to oGTT (yellow) and ITT (blue) following intraperitoneal insulin injection (schematic protocol in Fig. 11c). These assays were designed to probe whether TAAR1 influences glucose homeostasis at the organismal level by comparing the ability of KO and WT mice to clear a glucose bolus and to counterbalance insulin-induced hypoglycemia.

We observed that baseline blood glucose levels were comparable between genotypes (~150 mg/dL, compare Fig. 11d and e). Following glucose administration, however, TAAR1-KO mice displayed impaired clearance, failing to reduce blood glucose to WT levels during the first 30 min, with values plateauing around ~ 220 mg/dL before converging with WT at 60 min (~ 160 mg/dL, Fig. 11d). In comparison, the WT plateau was ~ 180 mg/dL, corresponding to ~ 20 % lower compared to the KO plateau. Following insulin administration, KO mice exhibited paradoxical hyperglycemia: blood glucose increased rather than decreased, in contrast to the marked drop observed in WT mice (from 150 mg/dL to ~ 100 mg/dL, Fig. 11e). This divergence persisted throughout the assay, with KO mice never matching WT values, even at 60 min when the experiment was terminated. Statistically significant genotype differences were observed at 15, 45, and 60 min post-insulin bolus (Fig. 11e). Despite the limited sample size, these results indicate that loss of TAAR1 exerts measurable effects on glucose regulation *in vivo*.

To further extend these observations, we examined Ca^{2+} dynamics in primary isolated islets from KO and WT mice using confocal microscopy (workflow in Fig. 11f). To activate TAAR1, we applied PEA as a representative TA across a concentration range of 100 nM to 10 μM (Fig. 11g). To block TAAR1, we used the selective antagonist EPPTB at 100 nM, 1 μM, and 25 μM (Fig. 11h). Unexpectedly, PEA did not increase oscillation counts above baseline in either genotype at any concentration tested (100 nM:

μ_{WT} = 75.3 ± 1.989, μ_{KO} = 66.6 ± 2.293, 1 μM: μ_{WT} = 75.4 ± 2.262, μ_{KO} = 74.4 ± 3.108, and 10 μM: μ_{WT} = 76.2 ± 1.569, μ_{KO} = 76 ± 1.183). EPPTB, in contrast, reduced oscillation counts relative to baseline, with similar effects on both genotypes except at 25 μM (100 nM: μ_{WT} = 91.1 ± 0.735, μ_{KO} = 91.2 ± 2.005, 1 μM: μ_{WT} = 83.3 ± 1.746, μ_{KO} = 75 ± 1.199, and 25 μM: μ_{WT} = 76.2 ± 5.199, μ_{KO} = 119 ± 1.183).

To confirm that TAAR1 was effectively targeted, we employed the synthetic, selective agonist developed by Roche, RO5256390 in a concentration range from 100 nM – 25 μM (Fig. 11i). Compared to PEA, responses were broader but did not differ between genotypes except at 1 and 25 μM (100 nM: μWT = 130.5 ± 2.88, μKO = 130.5 ± 1.490, 1 μM: μWT = 109.1 ± 0.837, μKO = 135.5 ± 5.056, 10 μM: μWT = 100.3 ± 2.144, μKO = 98.3 ± 2.513, and 25 μM: μWT = 118.2 ± 5.317, μKO = 103.1 ± 1.517). Thus, in contrast to the *in vivo* findings, we observed no statistically significant differences in Ca^{2+} dynamics between WT and KO islets either at baseline (5 mM glucose: μWT = 111.2 ± 2.020, μKO = 110.3 ± 0.567) or under pharmacological manipulation of TAAR1 (Fig. 11g-i).

Since TAAR1 manipulation did not yield detectable effects, we performed a positive control to validate the assay. For this, we examined α_2-adrenergic receptor (ADRA2) signaling by stimulating with Dexmedetomidine (Dex, agonist), followed by Idazoxan (Ida, antagonist) at 5 mM glucose. In β-cells, ADRA2 is $G_{i/o}$ coupled, reducing AC activity, lowering cAMP, and thereby decreasing exocytosis (139). ADRA2 is also reported to activate G-protein-gated inwardly rectifying potassium (GIRK) channels, causing membrane hyperpolarization and reduced Ca^{2+} influx (140). Based on this, we expected Dex to lower oscillation counts relative to baseline, and Ida to reverse this effect.

As expected, Dex reduced oscillation counts slightly (μ_{WT} = 104.9 ± 1.670; μ_{KO} = 105.5 ± 0.557). When Ida was added directly afterward, WT cells showed no response (μ_{WT} = 103.4 ± 3.739), suggesting possible off-target effects. For KO cells, Ida addition led to a significant drop in oscillation count (μ_{KO} = 77.4 ± 0.464), in line with suspected off-target effects, observed in WT but more pronounced.

Upon further consideration, we noted that C57BL/6J mice, the background strain used for TAAR1-KO generation, are characterized by a loss-of-function mutation in the nicotinamide nucleotide transhydrogenase (*Nnt*) gene, which has been reported to impair glucose homeostasis (127). It is therefore plausible that this strain-specific defect masked or overrode genotype-dependent effects in our *ex vivo* assays.

2.4 Discussion

Although expressed at low abundance, TAAR1 has been consistently identified in pancreatic β-cells by RNA detection and antibody-based staining across multiple laboratories (103,105,107). In agreement with these findings, we detected TAAR1 transcripts in MIN6 cells by RT-PCR (Fig. 9g). While this approach is qualitative and cannot determine expression levels or confirm receptor protein at the site of action, it indicates active transcription and suggests receptor availability. This interpretation is reinforced by the absence of detectable TAAR1 in αTC1 clone 9 cells, consistent with Revel *et al*. (107), who reported TAAR1 exclusion from glucagon-positive α-cells.

Using the MIN6 model, we further demonstrated that TAs are not only detectable but also likely synthesized endogenously, as shown by the detection of ^{15}N-labeled TAs following supplementation with ^{15}N-labeled precursor amino acids (Fig. 8a-c). This finding shifts the perspective on TAs from exogenous signaling molecules, such as those delivered by neuronal input, to potential autocrine factors produced and regulated within the islet microenvironment. Their insulinotropic effects were also glucose-dependent, though the concentrations at which they were most effective differed between individual amines. Additional work in the lab, extended these observations by examining CNS-active compounds that are structurally related to TAs but have not been formally characterized as TAAR1 ligands. The compounds tested included tricyclic antidepressants such as dibenzepine, idazoxan, and nomifensine, the benzodiazepine flurazepam, the antiparkinsonian agent diphenylhydramine, and ergoline

derivatives including lisuride (an antiparkinsonian agent) and methysergide (used in migraine prophylaxis). These compounds were assessed for their effects on insulin secretion from MIN6 cells and on intracellular Ca^{2+} oscillatory activity, with PEA serving as a positive control. The resulting data, currently available as a preprint, indicate that compounds sharing structural motifs with TAs can exert insulinotropic effects, likely mediated through TAAR1 activation (141).

Dose–response analyses revealed distinct potencies among TAs. PEA exhibited the highest efficacy with an EC_{50} of ~ 25 μM (determined in MIN6 cells), compared to TYR, which was less potent. While this EC_{50} is higher than literature-reported values (~ 0.2 μM on mouse TAAR1 determined by radioligand binding assay vs. ~ 0.08 - 0.4 μM on mouse TAAR1 determined by cAMP production in HEK293 cells) (100,120,142,143), those values were generated in different overexpression systems measuring proximal ligand–receptor interactions. In contrast, our readouts reflect downstream insulin secretion in a β-cell model (MIN6). Considering the confined extracellular space of islets and the likelihood of autocrine signaling, an effective concentration of 25 μM appears physiologically reasonable (144). Our findings further suggest that PEA functions as a weak partial agonist at β-cell TAAR1, with effects that are clearly glucose- and dose-dependent (Fig. 9b-f). Glucose dependency was particularly evident at the extreme ends of the glucose range tested (3 and 22 mM). In contrast to PEA, TYR displayed a more complex profile. Under glucose titration, TYR exhibited strong bidirectional effects, with stimulation at both low and high glucose concentrations, but suppression at intermediate concentrations (Fig. 9b and c). Under dose–response conditions at 11 mM glucose, TYR failed to follow a sigmoidal response and predominantly suppressed insulin secretion relative to control (Fig. 9d and f).

Although our experimental results from the two experimental approaches (Fig. $9a_i$ and a_{ii}) initially seemed divergent, they converged upon closer examination. For example, PEA at 10 μM yielded ~ 98 % of baseline secretion across a glucose gradient but ~ 128 % at a fixed glucose concentration. These values, though not identical, are similar across two distinct experimental approaches. TYR, in contrast,

displayed biphasic effects, enhancing secretion only at extreme glucose concentrations (3 mM and 22 mM) while suppressing it at intermediate levels. This pattern may suggest engagement of multiple targets or lower potency at TAAR1. It has been previously reported that TYR can serve as an indirect sympathomimetic agent, where it may engage adrenergic signaling, autonomic feedback, or local catecholamine-mediated inhibition of insulin secretion. Gilliam *et al.* report that low-dose TYR infusion in healthy subjects suppresses acute insulin release. The authors suggest that this is because TYR triggers endogenous catecholamine release from sympathetic nerves, which then act on α-adrenergic receptors on β-cells (G_i-coupled) to inhibit insulin secretion (145). Thus, at intermediate glucose concentrations (5 and 11 mM) or moderate concentrations of TYR, the inhibitory/receptor crosstalk effects (off-target effect on the α-adrenergic receptor) might dominate the TAAR1-mediated stimulatory pathway, resulting in net suppression. At low or high glucose (3 and 22 mM) (or high TYR), perhaps the positive TAAR1-mediated effect dominates, or the suppression is overridden by strong metabolic drive. However, considering our receptor specificity study using hTAAR1 in HEK293T cells, TYR displayed a rightward shift in the dose–response curves relative to PEA (Fig. 10d), which is consistent with lower potency.

Dose-response analysis in hTAAR1-expressing HEK293T cells allowed us to estimate EC_{50} values for PEA and RO5256390. The estimated values obtained from our dose-response curve (PEA: EC_{50} = ~ 1.77 μM, RO5256390: EC_{50} = ~ 0.197 μM, Fig. 10f) are higher compared to literature-reported values (PEA: EC_{50} = ~ 80.6 nM, RO5256390: EC_{50} = ~ 5.3 nM, both on hTAAR1). However, consistent with the literature, RO5256390 is more potent than PEA, although only 9-fold compared to 15-fold (literature). This divergence likely arises from assay- and system-dependent factors.

Calcium imaging provided mechanistic support. PEA increased Ca^{2+} spiking by ~ 30 % at 10 μM and ~ 44 % at 100 nM (Fig. 11b). Applied in sequence to PEA, the TAAR1 antagonist EPPTB reduced spiking by ~ 7-16 % relative to PEA, but the activity remained above baseline (Fig. 11b). This action is

consistent with neutral antagonism on TAAR1 (120,146). While ELISA confirmed increased insulin secretion under matched conditions, secretion rose more modestly over baseline (119 % at 10 μM PEA, Fig. 9c). This indicates that insulin release depends not only on Ca^{2+} oscillation number but also on amplification mechanisms and granule-pool dynamics downstream of Ca^{2+} entry. In β-cells, glucose metabolism elevates the ATP/ADP ratio, closing K_{ATP} channels, depolarizing the membrane, and generating voltage-dependent Ca^{2+} oscillations that drive insulin exocytosis (triggering pathway). Concurrently, glucose activates an amplifying pathway that operates distal to Ca^{2+} entry and enhances the efficacy of Ca^{2+} on granule recruitment and fusion. TAs further potentiate this process by engaging TAAR1, a $G_{\alpha s}$-coupled receptor that elevates intracellular cAMP levels and thereby strengthens both PKA- and Epac-dependent components of the amplifying pathway. Because Ca^{2+} oscillations arise from the interplay between metabolic flux, ion-channel gating, and Ca^{2+} clearance, the combined actions of glucose-driven triggering events and TAAR1-mediated amplification combine to increase the efficiency with which each Ca^{2+} oscillation translates into insulin granule exocytosis.

Because TAAR1 exhibits low sequence homology between rodents and primates (99,102), results from murine systems cannot be directly extrapolated to humans. To address this, we employed HEK293T cells expressing human TAAR1 (hTAAR1), which confirmed TA activity and yielded EC_{50} values for PEA closer to those reported in the literature (143). While informative, this model lacks the context of β-cells necessary for insulin secretion. Therefore, we turned to human donor-derived β-cells assembled into islet-like structures (Fig. 10g and h). In this system, PEA enhanced Ca^{2+} spikes above baseline at 11 mM glucose (~143 % increase) but not at 5 mM (~ 47 % of CTRL). This result initially seemed inconsistent with our MIN6 data (where we see increased insulin secretion at all tested glucose concentrations), but can be explained by species-specific glucose sensitivity as well as the lack of paracrine regulation in the β-cell only aggregates, which can dampen the stimulus-responsiveness compared to native islets (147–149). Despite that, this result is consistent with PEA stimulating insulin release in a

glucose-dependent manner, which aligns with cAMP-dependent amplification seen when TAAR1 (or other G_s-coupled GPCRs) are engaged.

To evaluate systemic relevance, we investigated TAAR1-KO mice and WT littermates using oral glucose and insulin tolerance tests. TAAR1 deficiency impaired whole-body glucose homeostasis *in vivo* (Fig. 11d and e). However, isolated islets from WT and TAAR1-KO mice showed no differences in Ca^{2+} dynamics between genotypes (Fig. 11g-j). To minimize potential misinterpretations arising from the presence of multiple islet cell types in dissociated cultures, we employed dithizone (DTZ) staining post-experiment to identify β-cells specifically (150). DTZ chelates Zn^{2+} co-secreted during insulin exocytosis, thereby selectively labeling β-cells, which appear red under bright-field microscopy (workflow in Fig. 11f). Only DTZ^+ cells were included in subsequent Ca^{2+} response analyses.

Despite restricting analysis to β-cells, we did not observe statistically significant differences between WT and KO β-cells in most conditions following TAAR1 manipulation. Occasionally, significant differences emerged between WT and KO β-cells at higher concentrations of EPPTB (Fig. 11h) or RO5256390 (Fig. 11i). However, within each genotype, TAAR1 modulation failed to elicit the expected effects.

To verify system responsiveness, we used α_2-adrenergic receptor (ADRA2) modulation as a positive control, applying the agonist dexmedetomidine (Dex) followed by the antagonist idazoxan (Ida) at 5 mM glucose. Given the inhibitory G_i-coupling of ADRA2 in β-cells, we anticipated Dex to reduce oscillation counts relative to baseline and Ida to reverse this effect. Yet, neither genotype exhibited this expected response (Fig. 11j), suggesting that GPCR signaling was generally non-functional in both WT and KO β-cells under these conditions.

This generalized signaling deficit likely stems from the C57BL/6J genetic background of the TAAR1-KO strain, which carries a loss-of-function mutation in nicotinamide nucleotide transhydrogenase (*Nnt*),

a mitochondrial enzyme essential for maintaining redox balance and supporting glucose-stimulated insulin secretion (127). The impact of Nnt deficiency becomes most apparent around 20 weeks of age (127). Therefore, our *in vivo* cohort (12–20 weeks) was not affected, and genotype-specific differences could still be observed. The *in vitro* cohort, however, composed primarily of animals older than 20 weeks, reflected background-driven impairments that likely masked TAAR1-specific phenomena. Alternatively, or perhaps additionally, the physiological phenotype observed *in vivo* may depend on compensatory mechanisms outside the islet microenvironment, which are absent in isolated β-cell preparations.

Chapter 3 Reverse-Engineered Islets: Building and Analyzing Pancreatic Pseudo-Islets

This chapter has been formatted for inclusion in this dissertation based on the project “Islet-Lego: reverse-engineered pseudo-islets from human donor islets” by Kaya Keutler, Craig Dorrell, Pamela Canday, and Carsten Schultz. The author of this dissertation is the first author on this project and used β-cell models and human islets to create and evaluate a model system for the investigation of islet formation (herein pseudo-islets).

3.1 Introduction

The starting point of forming pseudo-islets is healthy human donor islets. Human donors are inherently heterogeneous, and therefore, each islet preparation differs slightly from the previous one. Human islet preparations used in this thesis were received through the Integrated Islet Distribution Program (IIDP, USA) and the Alberta Diabetes Institute Islet Core (ADI, Canada). Both organizations provide extensive donor metadata, including anthropometric, metabolic, and in some cases, genetic information, thereby allowing controlled experimental stratification. In this thesis, we focused on four donor characteristics that are always reported in a standardized manner and have been previously described as being the cause of donor-to-donor variability: sex, age, body mass index (BMI), and glycated hemoglobin (A1c).

Sex is increasingly recognized as an important biological variable in islet biology (151). Human and rodent studies have demonstrated sex-dependent differences in β-cell mass, insulin secretory dynamics, and susceptibility to metabolic stress. For instance, female donors often exhibit enhanced β-cell proliferation and resilience to glucolipotoxic stress compared to males, potentially linked to estrogen receptor signaling and differential expression of genes regulating oxidative metabolism. Moreover, clinical data indicate that the onset and progression of T2D differ between sexes, with females frequently

maintaining a higher insulin secretory capacity in early stages of the disease (88,89,93,97,98,152,153). Despite these findings, sex-specific analyses remain underrepresented in islet research, underscoring the need for experimental stratification and balanced donor representation. Accordingly, one of our stratification approaches separated the donor cohort by sex to identify sex-dependent differences in islet function and pseudo-islet formation.

Age exerts a substantial influence on islet composition and functional integrity (154–157). With advancing age, human β-cells exhibit diminished proliferative potential, reduced insulin granule density, and increased expression of senescence-associated genes. Functionally, aged islets display slower calcium oscillatory dynamics and attenuated insulin release (157). Moreover, age-related shifts in α- and δ-cell proportions could alter paracrine regulation within the islet microenvironment (158). Although literature suggests that α-cells maintain their mass throughout the adult lifespan (159). Accounting for donor age is therefore critical when assessing islet functionality and regenerative potential, particularly in relation to reproductive aging and the menopausal transition.

Donor BMI correlates strongly with islet functional characteristics (160). Islets from obese donors commonly display an expanded β-cell area and higher insulin content, reflecting an adaptive response to peripheral insulin resistance (161,162). However, this compensatory remodeling is often accompanied by impaired glucose-stimulated insulin secretion and increased metabolic stress. Research indicates further that high-fat diets (HFD) induce changes in gene expression within islets, which could be contributing to the deterioration of β-cell mass and function, which is crucial for insulin production (163). Elevated BMI has also been associated with mitochondrial dysfunction and altered lipid metabolism within islet cells (164). Stratifying donors by BMI thus enables distinction between physiological adaptation to obesity and intrinsic β-cell dysfunction, providing insight into early mechanisms of β-cell compensation and metabolic stress.

A1c serves as a measure of chronic glycemic exposure and an indicator of the metabolic environment experienced by the donor before islet isolation. Even modest elevations in A1c, within the prediabetic range (> 5.7 %), are linked to β-cell dedifferentiation, oxidative stress, and impaired insulin secretory capacity (165). Consequently, donor islets with elevated A1c may exhibit altered stimulus-secretion coupling and reduced responsiveness in culture. Grouping donors by A1c level helps contextualize functional variability and separates glycemia-induced changes from intrinsic donor-specific differences.

To comprehensively address biological variability, the donor cohort in this study was stratified into four main categories, each containing two subgroups (see Table 4): sex (male, female), obesity status (obese, non-obese), reproductive status (reproductive age, postmenopausal), and glycemic history (healthy vs. elevated A1c). These groupings were selected based on literature suggestions that islet behavior is distinct between the sexes, largely attributed to the effect of estradiol on β-cells (89,93,152,153,166). Stratification by age into reproductive and postmenopausal groups further allowed exploration of hormonal influences associated with menopause, alongside age-related decline in islet functionality and cellular plasticity. Obesity, herein defined as a BMI > 30 kg/m^2, is increasingly recognized as a negative determinant of endocrine function, often associated with heightened endoplasmic reticulum and oxidative stress signaling (160,161,167,168). Separating donors into obese and non-obese groups was therefore essential to dissect obesity-associated changes in islet clustering and adaptation. Finally, A1c serves as a clinical indicator of glycemic control and a diagnostic criterion for diabetes. Donors were thus categorized as “normal” or “elevated” (A1c > 5.7 %). The 5.7 % threshold corresponds to prediabetes, a state associated with insulin resistance, impaired fasting glucose, and reduced glucose tolerance (169).

Pancreatic islets from each shipment were divided into native islets and pseudo-islets. The native islets remained intact and were used to observe the effects of in culture hormone supplementation on fully formed islets. The remaining islets were dissociated into single cells by trypsin digestion. These cells

were then stained with antibodies that allow cell type recognition. Typically, intracellular hormone staining (insulin, glucagon, somatostatin) is employed to identify β-, α-, and δ-cells, but such methods are incompatible with live-cell sorting required for pseudo-islet formation. To overcome this, surface-specific antibodies were used that recognize extracellular epitopes of endocrine cell types.

Thankfully, previous work has focused on the development of antibodies that recognize external structures on the outside of the cell types, and combination staining helped identify the distinct populations (170–172). First, HIC1-2B4 was used, which is a mouse IgG2b monoclonal antibody, and a marker for all endocrine cell types. Its antigen is the cell-surface receptor SLC3A2 that is selectively expressed by all pancreatic endocrine cells. This staining highlights the endocrine population and excludes exocrine cells or any other non-endocrine cell type that might be contaminating the preparation (170,172). HIC1-2B4 has been patented and is commercially available through Novus Biologicals in an Alexa488 conjugated or unconjugated version. A second antibody, HIC1-8G12, was used to subtype pancreatic endocrine cells. HIC1-8G12 recognizes transmembrane 4 L6 family member 4 (TM4SF4), a cell-surface tetraspanin expressed at high levels on α-cells, intermediate levels on δ-cells, and low-to-absent levels on β-cells (170,171,173). In flow-cytometry experiments, the top fraction of TM4SF4^{high} cells co-expresses glucagon, confirming that TM4SF4 surface expression is highest on glucagon-secreting α-cells (173,174). An earlier version of the HPa3-HIC1-8G12 antibody (HPa3 Antibody (HIC3-2D12), Novus Biologicals, REF# NBP3-18520) is commercially available, although this version is unconjugated. For this work, only primary-conjugated antibodies were used to keep protocols short (HIC1-2B4 A488, HIC1-8G12 PE, and αCD9 APC). Finally, anti-human CD9 (ThermoFisher, REF# 17-0098-42) staining was used to enhance the separation of δ-cells. This antibody recognizes human CD9 tetraspanin, a 24–27 kDa glycoprotein with four transmembrane domains and two extracellular loops (175). CD9 staining selectively identifies human pancreatic δ-cells, because δ-cells display higher surface levels of this tetraspanin compared to other islet endocrine cells. In a functional proteomics screen on human

islets, the top 10 % of CD9-expressing cells ($CD9^+$) were highly enriched for intracellular somatostatin (which δ-cells produce), whereas $CD9^-$ cells lacked δ-cell identity (176). When these three antibodies are combined and additional information from side scatter and brightness of staining were drawn, distinct populations of α-cells, β-cells, and δ-cells could be identified (see Table 3).

In contrast to native islets, which are already assembled and have, depending on the age of the donor, undergone multiple environmental changes/adaptations, pseudo-islets are reconstituted *de novo* from dissociated mature islet cells. They do, however, contain the same, mature cells as the native islets they originate from. Therefore, pseudo-islets provide a unique viewpoint of how differentiated endocrine cells reassemble into functional islet structures and respond to environmental cues such as hormonal supplementation in culture media.

Table 3: Population-specific antibodies for sorting dissociated human islet cells into distinct populations.

Antibody	Recognized cell type	α-cells	β-cells	δ-cells
HIC1-2B4	Endocrine cells	+	+	+
HIC1-8G12	Non-β endocrine cells	+	-	+
CD9	δ-cells	-	-/+ (inform on side scatter)	++

The pseudo-islet platform, described here, bridges the gap between oversimplified cell-line models and the complexity of native human islets, offering a versatile and expandable tool for mechanistic studies (see Fig. 5).

3.2 Materials and Methods

3.2.1 Handling of human pancreatic islets.

Human pancreatic islets were provided by the NIDDK-funded Integrated Islet Distribution Program (IIDP) (RRID:SCR _014387) at City of Hope, NIH Grant # U24DK098085, and the JDRF-funded IIDP Islet Award Initiative (Study # BS562P & BS562). Additionally, human islets for research were provided by the Alberta Diabetes Institute IsletCore at the University of Alberta in Edmonton (http://www.bcell.org/adi-isletcore.html) with the assistance of the Human Organ Procurement and Exchange (HOPE) program, Trillium Gift of Life Network (TGLN), and other Canadian organ procurement organizations. Islet isolation was approved by the Human Research Ethics Board at the University of Alberta (Pro00013094) (27). All donors' families gave informed consent for the use of pancreatic tissue in research. Islets from both distribution programs were shipped overnight and processed on the receiving day. If that was not possible, they were stored at 4 °C for no more than seven days in the transport media. Native islets, when used as controls for pseudo-islets, were cultured in 1x CMRL 1066 media (Corning, REF# MT15110CV) supplemented with 10 % FBS, 10 mM HEPES (Cytivia, REF#AJ30727929), and 2 % L-glutamine (Gibco, REF#25030-081) with 1 % Pen/Strep (Gibco, REF# 15140122) and 1 μg/mL Amphoticerin B (Sigma, A2942, CAS # 1397-89-3) added just before use in culture. Human donor characteristics are listed in Appendix Table S1.

3.2.2 Tissue sources and pancreatic cell isolation.

Human pancreatic islets from normal donors were obtained from the NIDDK-funded Integrated Islet Distribution Program (IIDP) at City of Hope (Study # BS562P & BS562). These were collected from approved, consented cadaveric organ donors from whom at least one other organ has been approved for transplantation, and are exempt from human studies approval. Specimens were dispersed to single-cell suspensions by an 8–15 min digestion in 0.05 % trypsin-EDTA (Gibco, REF#25-300-054) at 37 °C

with dispersal by a p1000 micropipette every 3 min. The progress of the dispersion was checked by light microscopy. Undispersed tissue was removed with a 40-μm cell strainer (Fisherbrand, REF#22-363-547), and dissociated cells were stored on ice in holding buffer (CMRL1066 + 2% FBS + 0.1 mg/mL trypsin inhibitor (Sigma, REF#T9128) and 0.1 mg/mL DNAse I (Roche, REF#10104159001) before antibody labeling for FACS (FACS workflow with examples for each step in Fig. 12a-f). The number of samples analyzed was primarily determined by material availability, but it was chosen to be sufficient for statistical analysis.

3.2.3 FACS of dissociated human islets into pure α-, β-, and δ-cell populations.

Dissociated cells were resuspended in holding buffer (CMRL1066 + 2% FBS + 0.1 mg/mL trypsin inhibitor (Sigma, REF#T9128) and 0.1 mg/mL DNAseI (Roche, REF#10104159001)) before the addition of antibodies. The antibodies used were: HIC1-2B4 A488 conjugated (Novus Biologicals, REF# NBP1-18946AF488) at a 1:100 dilution, HIC1-8G12 PE conjugated (provided by the Grompe lab) at 1:50 dilution, and anti-CD9 APC conjugated to APC (Thermo Fisher Invitrogen, MA1-10307) at a 1:20 dilution. Single antibody controls, A488 + PE (fluorescence minus one (FMO)), and all combined samples were incubated at 4°C for at least 20 min. After washing with cold CMRL1066, cells were resuspended in holding buffer, and 1 μg/mL propidium iodide (PI) (Sigma, REF#P4864) was added for live/dead distinction. Cell doublets were excluded by pulse width measurement, and PI staining was used to label dead cells for exclusion (Fig. 12c and i). Analysis was performed on a Cytopeia inFluxV-GS (Becton-Dickinson, BD) or a BD Symphony S6.

3.2.4 Generation of pseudo-islets.

Freshly sorted pancreatic cells were used to generate pseudo-islets. Pure cell populations were spun down directly after sorting and resuspended in 300 μL of media (CMRL1066 + 2% FBS + 1 % Pen/strep, + 1 μg/mL Amphoticerin B). Based on the obtained cell numbers, concentrations in cells/μL were

calculated and used to mix cells in specific ratios. If not indicated otherwise, cells were combined in a 5:1 ratio for β:α, 16:1 for β:δ, and 3:1 for α:δ. Additionally, pseudo-islet mixtures were combined with MS1 cells in a 1:10 ratio, with ten MS1 cells (kindly provided by the Grompe Lab, CRL-2279) for every one endocrine cell (unless otherwise specified). Cell mixtures were seeded in ultra-low attachment, flat-bottom 6-well plates (Corning, REF# CLS3471) in 3 mL of media (CMRL1066 + 2% FBS + 1 % Pen/strep, + 1 μg/mL Amphoticerin B). Cluster formation was allowed to happen for up to 14 days with hormone (0.1 μg/mL GCG or GLP-1, and 100 nM SST) addition and culture media refill (100 μL/well to account for evaporation) every other day. Cluster formation was monitored by using a Keyence EPI-microscope in brightfield mode and FIJI software (see Appendix Fig. 4) to analyze the generated images.

3.2.5 Supplementation of pancreatic cell lines, native islets, and pseudo-islets.

For media supplementation, compounds were purchased from Sigma and used at 0.1 μg/mL for GCG and GLP-1 and 100 nM for SST. Compounds were added every other day for the duration of the experiment. To account for evaporation and to replenish nutrients, 100 μL of media was refilled every other day.

3.3 Results

3.3.1 Assessment of population purity and viability following endocrine cell sorting

For each sort, a subset of native islets was removed before dissociation and maintained in culture under the same conditions as the pseudo-islets serving as native islet controls. The remainder of the islets was processed through the sorting pipeline described in Fig.12a-f. Population purity was determined for each sort by using cells that were not associated with any of the desired populations (Fig. 12g & h). For this, a sample of those cells was collected and re-sorted with the same settings. In case of a clean and pure sort, a negligible percentage (< 0.5 %, Fig. 12h) of the sorted cells appear in the α-cell, β-cell, or δ-cell gates. Additionally, since a subset of β-cells can stain positive for CD9 (177), further purity assessment was performed using 8G12 staining as the ground truth discriminator between β-cells and non-β-cells. This way, β-cell "calling" is CD9 independent. Using this discrimination, β-cells are defined as 2B4+ 8G12–, side scatter $(SSC)^{high}$ among live singlets (Fig. 12i), and δ-cells are confined to the 2B4+ 8G12+, SSC^{low} compartment (further subdivided by CD9, Appendix Fig. 1b). Following this distinction, purity was calculated as parent percent of lineage gates among live singlets: β-cells = 2B4+ 8G12–, SSC^{high}, ~ 52 %, α-cells = 2B4+ 8G12+ CD9–, SSC^{high}, ~ 30 %, and δ-cells = 2B4+ 8G12+ CD9+, SSC^{low} ~ 9 %. To further test if there is cross-contamination between β-cells and δ-cells, we turned to our fluorescence minus one (FMO) control that does not include CD9 staining (AF488 + PE – CD9). The cell gates from our stained sample were cloned to the 8G12 FMO, showing that the δ-cell gate is empty (Appendix Fig. 1c and d).

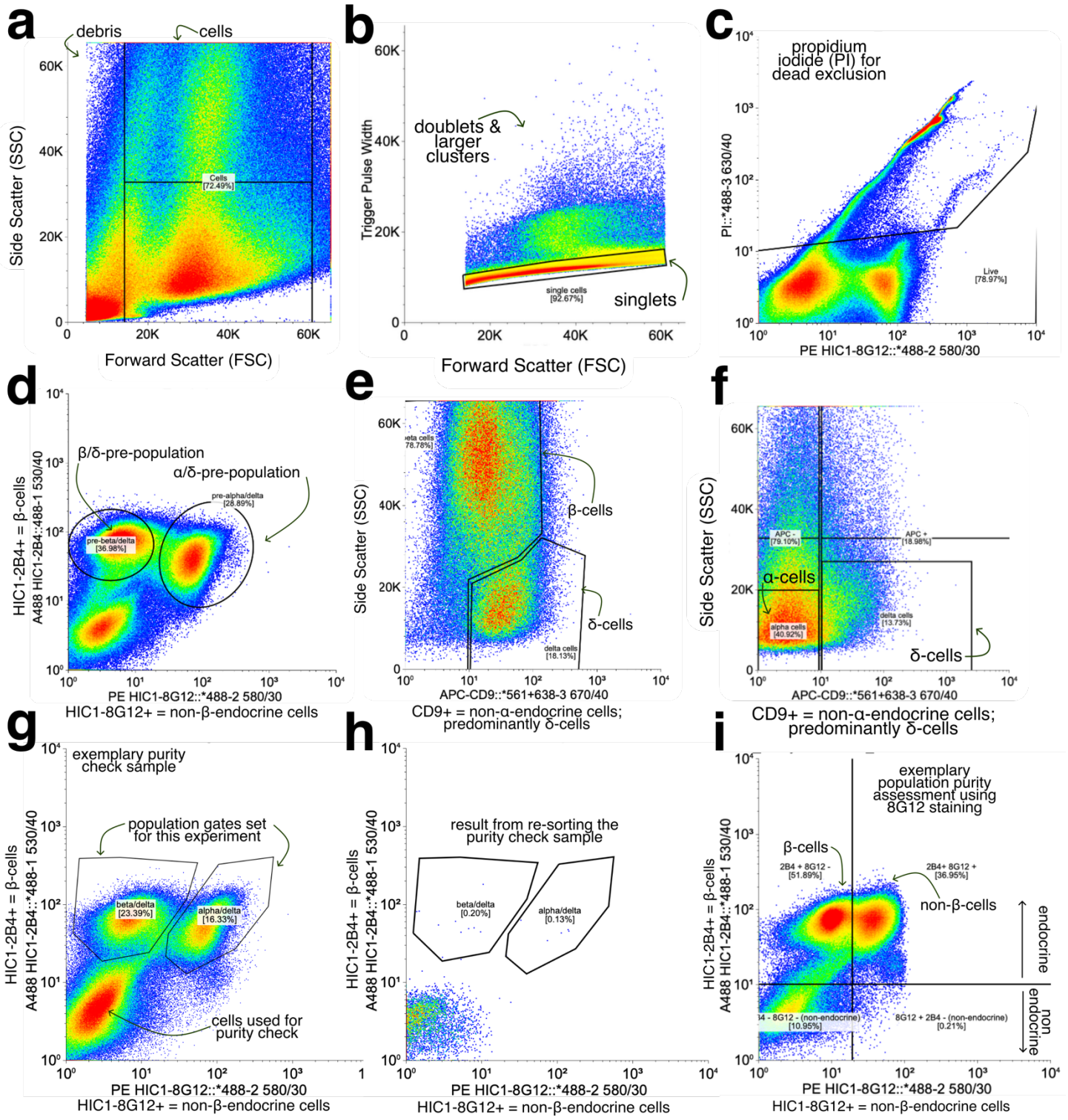

Figure 12: Cell sorting (FACS) workflow for isolating endocrine cell populations from human donor islets. Human native islets are enzymatically dissociated into single-cell suspensions and stained with a combination of endocrine-specific antibodies: HIC1-2B4, which labels β-cells; HIC1-8G12, which labels non-β endocrine cells, and CD9, which labels δ-cells and a minor subset of β-cells, and is used to exclude α-cells. This antibody panel allows for the identification and separation of β-cells, α-cells, and δ-cells. (**a**) Debris is excluded based on forward scatter (FSC) and side scatter (SSC) parameters. (**b**) Single cells are gated by excluding doublets and aggregates. (**c**) Propidium iodide (PI) is used to exclude dead cells; only PI-negative (viable) cells are analyzed. (**d**) Cells are first separated based on HIC1-2B4 (y-axis) and HIC1-8G12 (x-axis) signal to identify pre-populations of β-/δ-cells and α-/δ-cells. (**e & f**) Within these pre-populations, CD9 expression and SSC are used to further resolve δ-cells (**e**) and (**f**). Before sorting, 10 μm reference beads are used to identify the cell population window. Non-endocrine or undefined cells are collected separately for post-sort purity assessment (**g**). (**h**) exemplary post-sort analysis of purity check sample using the same pre-population gates as for the stained sample. (**i**) Excluded PI+ (dead cells) were used to identify the percentage of dead cells during FACS. All FACS data were analyzed using Floreada.io.

3.3.2 Establishment of pseudo-islets

Multiple donors were merged based on donor characteristics (sex, age, BMI, and A1c) and stratified into four groups, each with two subgroups. The resulting groups, along with the number of donors per group, are listed in Table 4.

Table 4: Donor stratification based on characteristics. Donors were stratified based on their sex, age, BMI, and A1c values. Respective donor numbers are listed.

Donor Sex		Donor Age		Donor BMI		Donor A1c	
Female	Male	Reproductive (<50 years)	Post-Menopause (> 50 years)	Non-obese (BMI < 30 kg/m^2)	Obese (BMI > 30 kg/m^2)	Normal (A1c < 5.7 %)	Elevated (A1c > 5.7 %)
17	17	19	15	20	14	19	15

Once sorted, α-cells, β-cells, and δ-cells were mixed in desired combinations and cultivated in a 1:10 ratio with MS1 cells in suspension to form pseudo-islets. Pseudo-islet formation was monitored by EPI-fluorescence microscopy every 2-3 days and up to 14 days (Fig. 13a). Identifiable clusters were already present at the first imaging point (2–3 days post-seeding), suggesting that initial pseudo-islet formation is a rapid process. In addition to testing different combinations of cells and cell-cell ratios, different media supplementations were also investigated (details in Table 5).

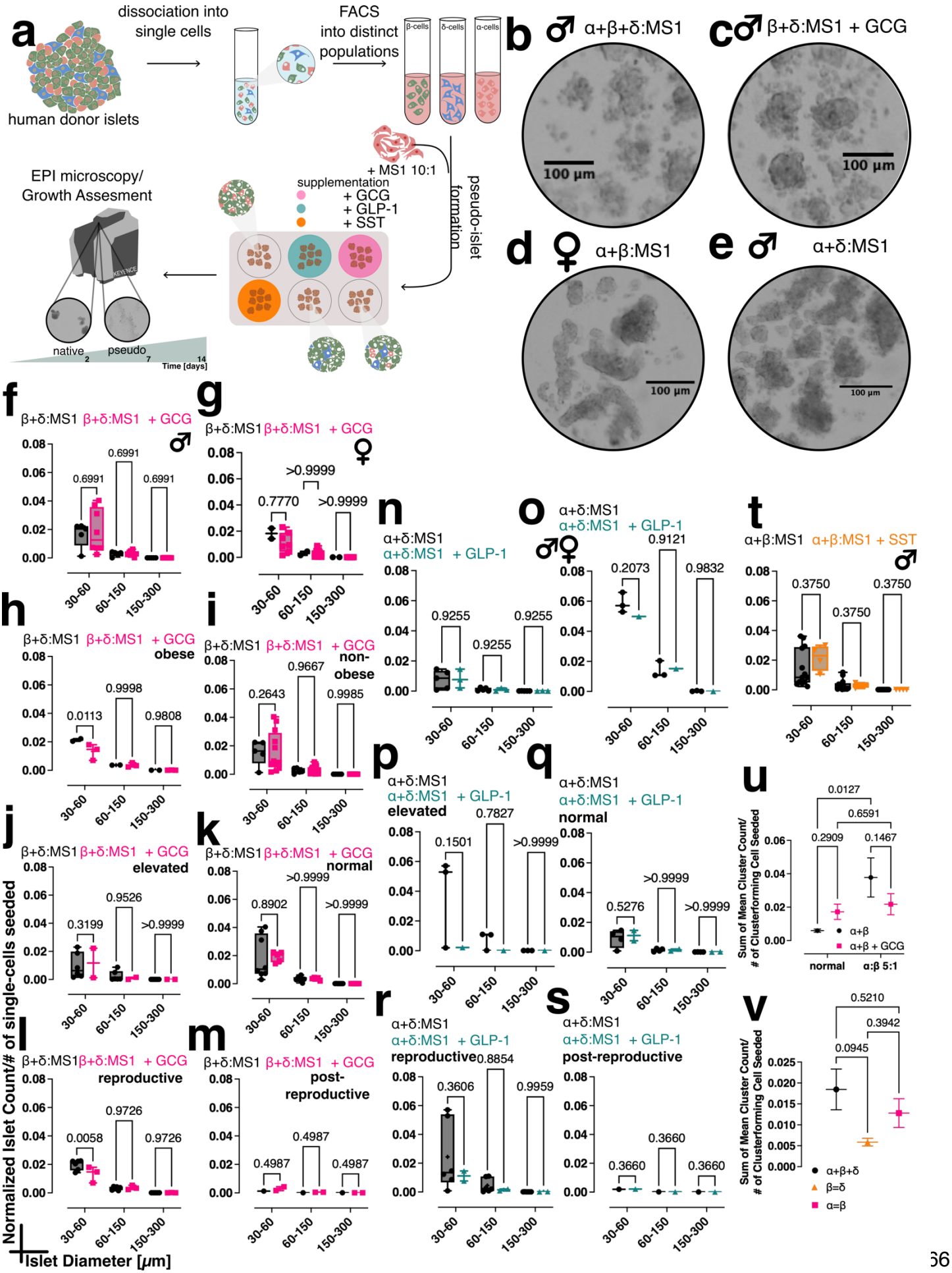
a
dissociation into single cells
human donor islets
FACS into distinct populations
β-cells
δ-cells
α-cells
+ MS1 10:1
pseudo-islet formation
supplementation
+ GCG
+ GLP-1
+ SST
EPI microscopy/ Growth Assesment
native
pseudo
Time [days]
b ♂ α+β+δ:MS1
c♂ β+δ:MS1 + GCG
d ♀ α+β:MS1
e ♂ α+δ:MS1
100 µm
f β+δ:MS1 β+δ:MS1 + GCG ♂
g β+δ:MS1 β+δ:MS1 + GCG ♀
h β+δ:MS1 β+δ:MS1 + GCG obese
i β+δ:MS1 β+δ:MS1 + GCG non-obese
j β+δ:MS1 β+δ:MS1 + GCG elevated
k β+δ:MS1 β+δ:MS1 + GCG normal
l β+δ:MS1 β+δ:MS1 + GCG reproductive
m β+δ:MS1 β+δ:MS1 + GCG post-reproductive
n α+δ:MS1 α+δ:MS1 + GLP-1
o α+δ:MS1 α+δ:MS1 + GLP-1 ♂♀
t α+β:MS1 α+β:MS1 + SST ♂
p α+δ:MS1 α+δ:MS1 + GLP-1 elevated
q α+δ:MS1 α+δ:MS1 + GLP-1 normal
r α+δ:MS1 α+δ:MS1 + GLP-1 reproductive
s α+δ:MS1 α+δ:MS1 + GLP-1 post-reproductive
u Sum of Mean Cluster Count/ # of Clusterforming Cell Seeded
α+β
α+β + GCG
normal
α:β 5:1
v Sum of Mean Cluster Count/ # of Clusterforming Cell Seeded
α+β+δ
β=δ
α=β
Normalized Islet Count/# of single-cells seeded
Islet Diameter [µm]
30-60
60-150
150-300

Figure 13: Pseudo-islet generation and comparison across donor characteristics and cell combinations. (**a**) Workflow of pseudo-islet generation, culture, and formation assessment. (**b-e**) exemplary brightfield images of pseudo-islets for different cell combinations; scale bar is 100 μm. (**f-m**) Pseudo-islets generated from the combination of β-cells and δ-cells and supplemented with 0.1 μg/mL GCG (pink) vs. CTRL (black) for male (**f**) and female (**g**) donors, obese (**h**) and non-obese (**i**) donors, donors with elevated A1c (**j**) and normal A1c (**k**), and reproductive (**l**) vs. post-reproductive (**m**) donors. (**n-s**) Pseudo-islets generated from the combination of α-cells and δ-cells and supplemented with 0.1 μg/mL GLP-1 (teal) vs. CTRL (black) for male (**n**) vs. female (**o**) donors, elevated (**p**) vs. normal A1c (**q**) donors, and reproductive (**r**) vs. post-reproductive (**s**) donors. The y-axis lists the mean islet count normalized to the number of single cells seeded for pseudo-islet generation, and the x-axis lists islet diameters in μm ranging from 30-300 μm. (**t**) Pseudo-islets generated from male donos by. the combination of α-cells and β-cells and supplemented with 100 nM SST (orange) vs. CTRL (black). (**u**) Sum of mean cluster count normalized to the number of cluster-forming cells seeded (index of dispersion vs. compaction) for α+β with 0.1 μg/mL GCG (pink) vs. CTRL (black) for normal cell ratios (5:1 β:α) vs. inverse ratios. (**v**) Sum of mean cluster count normalized to the number of cluster-forming cells seeded (index of dispersion vs. compaction) for pseudo-islets from α+β+δ clusters at normal (5:1 β:α and 16:1 β:δ) ratios, δ-cells increased to match β-cells (β=δ, orange), or α-cells increased to match β-cells (α=β, pink). Unless stratified by sex, all groups include both female and male donors. Statistical comparisons were done using two-way ANOVA or mixed effects analysis (depending on data availability) with Benjamini-Hochberg correction for multiple comparisons. All p-values are listed on the respective graphs, with the cutoff for statistical significance being 0.05. Error bars represent SEM.

3.3.3 Functional omission of cell types (absence model)

To assess the contribution of individual endocrine cell types, we eliminated one cell type at a time. This yielded α+β, α+δ, and β+δ pseudo-islets. These conditions allowed us to monitor how the absence of a specific cell type influenced cluster formation (Fig. 13f-t).

Additionally, in exploratory experiments, we supplemented the culture medium with the hormone secreted by the omitted cell type. For example, β+δ pseudo-islets were supplemented with GCG to account for the absence of α-cells. This strategy enabled a distinction between the role of the physical presence of a cell type (where cell–cell interactions can establish) versus the effect of its hormone in isolation (Fig. 13f-m & t). Similarly, the influence of GLP-1 was tested in a model lacking β-cells (α+δ clusters) (Fig. 13n-s). We applied this omission concept across all donor groups (stratified by sex (Fig. 13f and g, n, o, and t), BMI (Fig. 13h and i), A1c (Fig. 13j and k, p and q), and age (Fig. 13l, m, r and s). We find that GCG supplementation in the α-cell absence model produced statistically significant differences compared to control conditions for obese donors (Fig. 13h) as well as donors of reproductive age (Fig. 13l). In these cases, GCG supplementation lowered the mean cluster count compared to control conditions, suggesting that GCG addition leads to fewer but bigger clusters compared to control conditions (compacted system). GLP-1 addition in the β-cell absence model does not lead to

statistically significant differences compared to control, independently of how the donor cohort was stratified. GLP-1 addition in the β-cell–absence model did not change clustering metrics, suggesting either no effect on this phenotype under our conditions or that any GLP-1–mediated influence is mostly β-cell dependent. For the δ-cell absence model (α+β), which was supplemented with 100 nM SST, data were available only from male donors. Therefore, comparisons across stratification groups or with female donors were not possible. Nonetheless, a non-significant trend was observed toward an increased number of clusters within the 30–60 μm diameter range under SST supplementation (Fig. 13t).

3.3.4 Influence of cell-cell ratios

Within native islets, endocrine cells are distributed approximately as 60 % β-cells, 30 % α-cells, and 2 % δ-cells (178). These ratios translate to α:β ≈ 1:5, α:δ ≈ 3:1, and β:δ ≈ 16:1. However, more recent studies suggest that no universal “standard” islet exists. For instance, Lehrstand *et al.* described small islets (~ 60 μm in diameter), composed predominantly of β-cells, that contribute disproportionately to insulin secretion (45). In an exploratory manner, we have experimented with altered cell-cell ratios. For example, instead of α:β being 1:5, we switched to 5:1, effectively increasing the α-cell count and decreasing the β-cell count. Additionally, we experimented with equal amounts (1:1), leading to islets having the same number of α- and β-cells (Fig. 13u and v). We find that at a physiological α:β ratio, GCG addition leads to an increase in cluster counts suggestive of a more dispersed system compared to CTRL (Fig. 13u). When switching the ratio between β-cells and α-cells, effectively increasing α-cell and decreasing β-cell presence in the pseudo-islet clusters, we find that already under CTRL conditions, the system is more dispersed, indicated by increased counts (Fig. 13u, CTRL, black). GCG supplementation in that case led to a decrease in cluster counts (close to normal + GCG values), suggesting compaction (Fig. 13u, black vs. pink). This indicates that GCGs’ effect on pseudo-islet organization is composition dependent.

In contrast, α+β+δ pseudo-islets assembled at physiological ratios (5:1 β:α and 16:1 β:δ) displayed a more dispersed organization compared to α+β pseudo-islets (0.01846 vs. 0.00594; Fig. 13v vs. u). Increasing the δ-cell proportion to achieve a 1:1 β:δ ratio (0.00587 (orange) vs. 0.01846 (black), Fig. 13v) led to a significant reduction in cluster counts, indicative of enhanced compaction. This effect is likely mediated by elevated SST signaling, which inhibits both INS and GCG secretion and attenuates paracrine crosstalk, thereby promoting cluster cohesion. In contrast, when α-cell numbers were increased to match β-cell numbers, cluster counts rose again (0.0128 (pink) vs. 0.00587 (orange)), indicating a shift toward a more dispersed morphology. Relative to the physiological condition, however, the β=α configuration remained intermediate in compaction, consistent with higher endogenous GCG levels from the additional α cells.

All variations performed, but not discussed in detail in the text, including cell combinations and media supplementation across donor groups stratified by sex, age, BMI, and A1c, are listed in Table 5.

Table 5: Pseudo-islet formation across various cell type combinations and media supplementations. Pseudo-islets were formed by varying their composition, as well as the exogenous hormone availability. The number of repeats was stratified by donor sex, age, BMI, or A1c, and is also listed.

Number of re-peats/ donor sex	Number of re-peats/ donor age	Number of repeats/ donor BMI	Number of re-peats/ donor A1c	Pseudo-islet composition	Media supplementation
8 F/9 M	10 < 50/ 4 > 50	11 < 30 kg/m^2/ 3 > 30 kg/m^2	8 < 5.7 % / 7 > 5.7 %	α+β+δ:MS1	none
4 F/1 M	9 < 50/ 3 > 50	4 < 30 kg/m^2/ 2 > 30 kg/m^2	6 < 5.7 % / 3 > 5.7 %	α+β+δ:MS1	+ GCG
1 F/2 M	3 < 50/ 0 > 50	2 < 30 kg/m^2/ 1 > 30 kg/m^2	2 < 5.7 % / 1 > 5.7 %	α+β+δ:MS1	+ GLP-1
4 F/5 M	5 < 50/ 1 > 50	5 < 30 kg/m^2/ 1 > 30 kg/m^2	4 < 5.7 % / 2 > 5.7 %	β+δ:MS1	none
7 F/6 M	3 < 50/ 2 > 50	10 < 30 kg/m^2/ 3 > 30 kg/m^2	3 < 5.7 % / 6 > 5.7 %	β+δ:MS1	+ GCG
3 F/8 M	5 < 50/ 2 > 50	4 < 30 kg/m^2/ 4 > 30 kg/m^2	6 < 5.7 % / 2 > 5.7 %	α+β:MS1	none
2 F/3 M	2 < 50/ 1 > 50	2 < 30 kg/m^2/ 1 > 30 kg/m^2	2 < 5.7 % / 1 > 5.7 %	α+β:MS1	+ GCG
2 F/3 M	3 < 50/ 2 > 50	4 < 30 kg/m^2/ 1 > 30 kg/m^2	3 < 5.7 % / 2 > 5.7 %	α+β:MS1	+ GLP-1
3 M	2 < 50/ 1 > 50	2 < 30 kg/m^2/ 1 > 30 kg/m^2	2 < 5.7 % / 1 > 5.7 %	α+β:MS1	+ SST
1 F/5 M	5 < 50/ 1 > 50	5 < 30 kg/m^2/ 1 > 30 kg/m^2	4 < 5.7 % / 2 > 5.7 %	α+δ:MS1	none
1 M	1 < 50/ 0 > 50	0 < 30 kg/m^2/ 1 > 30 kg/m^2	1 < 5.7 % / 0 > 5.7 %	α+δ:MS1	+ GCG
1 F/2 M	2 < 50/ 1 > 50	2 < 30 kg/m^2/ 1 > 30 kg/m^2	2 < 5.7 % / 1 > 5.7 %	α+δ:MS1	+ GLP-1
1 M	0 < 50/ 1 > 50	1 < 30 kg/m^2/ 0 > 30 kg/m^2	0 < 5.7 % / 1 > 5.7 %	α+δ:MS1	+ SST
3 F/2 M	4 < 50/ 0 > 50	1 < 30 kg/m^2/ 3 > 30 kg/m^2	3 < 5.7 % / 0 > 5.7 %	α ONLY:MS1	none
3 F/2 M	3 < 50/ 0 > 50	1 < 30 kg/m^2/ 2 > 30 kg/m^2	2 < 5.7 % / 1 > 5.7 %	α ONLY:MS1	+ GLP-1
2 M	2 < 50/ 0 > 50	1 < 30 kg/m^2/ 1 > 30 kg/m^2	2 < 5.7 % / 0 > 5.7 %	α ONLY:MS1	+ SST
4 F/3 M	5 < 50/ 1 > 50	4 < 30 kg/m^2/ 2 > 30 kg/m^2	5 < 5.7 % / 2 > 5.7 %	β ONLY:MS1	none
3 F/3 M	4 < 50/ 1 > 50	3 < 30 kg/m^2/ 2 > 30 kg/m^2	3 < 5.7 % / 2 > 5.7 %	β ONLY:MS1	+ GCG

3.3.5 Opposing dynamics of native and pseudo-islets

Whereas native islets fragment over time in culture as reported previously (179), pseudo-islets initiate from single cells and therefore progress in the opposite direction (formation). We hypothesized that initially, subclusters (< 30 μm in diameter) would emerge as single cells began to cluster. Over time,

subclusters would decrease while aggregates within larger size bins (30–60, 60–150, 150–300 μm) would increase, reflecting pseudo-islet assembly (see Fig. 14a).

As visually described in Figure 14a, native islets fragment over time in culture, and this fragmentation is indicated by a decrease in the number of islets (normalized to the initial number seeded). Additionally, to complement the islet counts, we measured subclusters. By measuring the subclusters, we can further follow fragmentation as the islets become smaller and move out of the sizes measured (30-60, 60-150, and 150-300 μm in diameter). Fragmentation is a dynamic process. When > 150 μm in diameter islets fragment, the pieces will appear in the 60-150 μm sizing bin and eventually 30-60 μm. Because of this effect, following the smallest islet size bin (30-60 μm in diameter) over time functions as a proxy for the behavior of the larger sizes (Fig. 14c-f and k-n). Finally, when those smaller islets fall apart, they form subclusters and will then be part of the bulk counted as < 30 μm (Fig. 14 g-j and o-r).

Native islet counts were normalized to the number of IEQ seeded per well (Fig. 14b, native). Therefore, a normalized value of 1 is indicative of structural stability, meaning the number of islet-sized clusters matches the number of IEQ seeded. Values below 1 suggest fusion of multiple IEQ into larger aggregates, while values above 1 indicate fragmentation into excess smaller clusters. To refine these interpretations, we also examined the percentage of subclusters (< 30 μm diameter) normalized to the control. An increase in subclusters alongside a decreased cluster count reflects disintegration into fragments below the islet threshold. In contrast, a stable or reduced subcluster percentage points to fusion into larger aggregates. When normalized counts exceed 1, a higher subcluster percentage indicates active fragmentation, a stable percentage suggests breakage within the islet-size range, and a reduced percentage may signal degradation into single cells or debris.

For pseudo-islets, normalized counts instead reflect the number of clusters formed per single cell seeded (Fig. 14b, pseudo). Here, subcluster percentages provide additional information about size distribution. Increases in both cluster count and subcluster percentage indicate fragmentation or the

generation of many small aggregates. An increase in count with stable subcluster percentage suggests growth in the mid-size range, while a decrease in subclusters with increased counts points to fusion of smaller units into larger structures. In contrast, a decline in counts coupled with rising subcluster percentage reflects fragmentation of larger clusters, whereas declining counts with stable subcluster percentage suggest consolidation into fewer, similarly sized aggregates. Finally, concurrent decreases in both measures indicate maturation or fusion into larger structures accompanied by loss of smaller clusters.

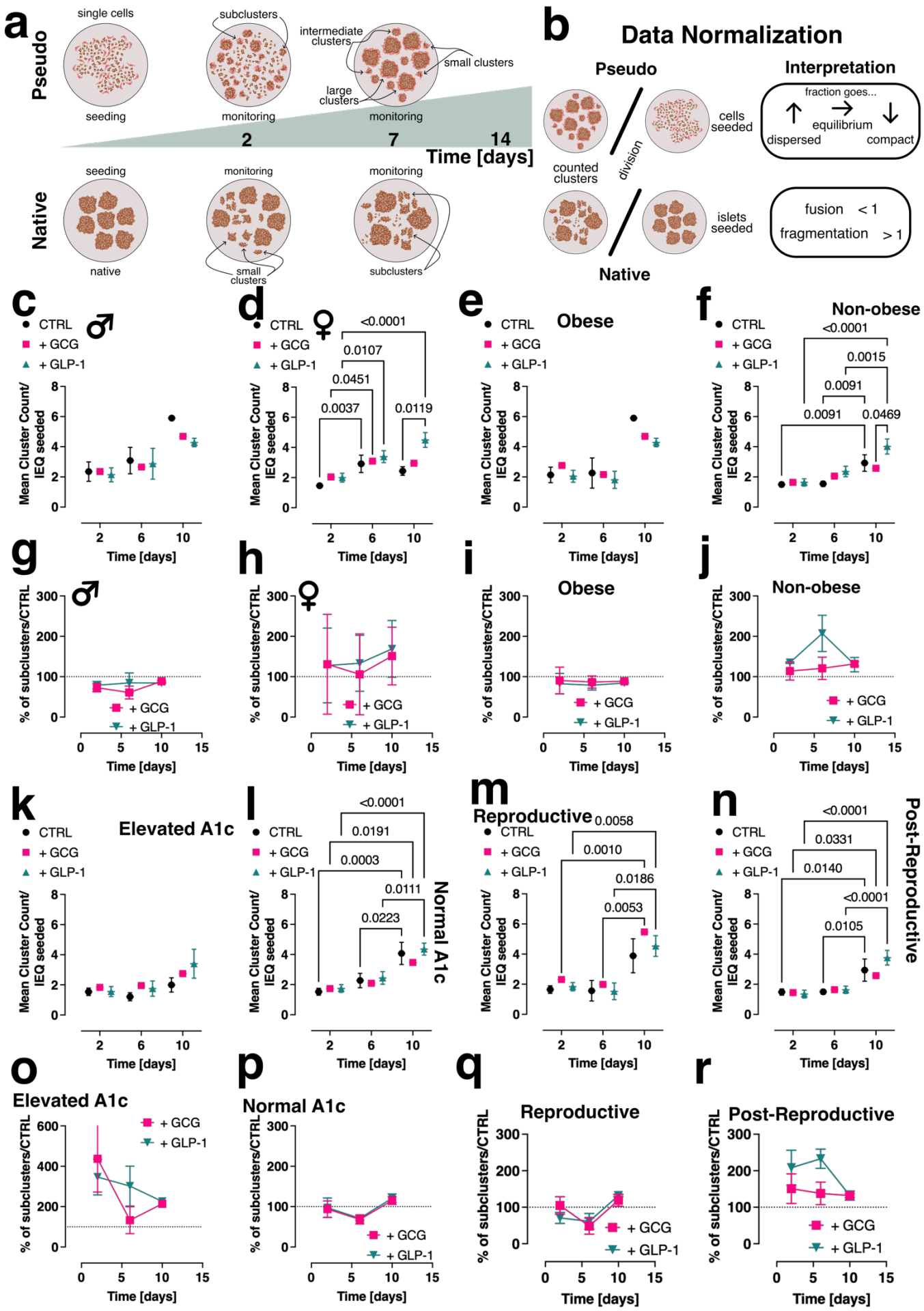
a
Pseudo
single cells
seeding
subclusters
monitoring
intermediate clusters
large clusters
small clusters
monitoring
2
7
14
Time [days]
Native
seeding
native
monitoring
small clusters
monitoring
subclusters
b
Data Normalization
Pseudo
counted clusters
division
cells seeded
Native
islets seeded
Interpretation
fraction goes...
dispersed
equilibrium
compact
fusion < 1
fragmentation > 1
c
CTRL
+ GCG
+ GLP-1
♂
Mean Cluster Count/ IEQ seeded
Time [days]
d
♀
<0.0001
0.0107
0.0451
0.0037
0.0119
e
Obese
f
Non-obese
<0.0001
0.0015
0.0091
0.0091
0.0469
g
% of subclusters/CTRL
h
i
j
k
Elevated A1c
l
<0.0001
0.0191
0.0003
0.0111
0.0223
Normal A1c
m
Reproductive
0.0058
0.0010
0.0186
0.0053
n
<0.0001
0.0331
0.0140
<0.0001
0.0105
Post-Reproductive
o
Elevated A1c
p
Normal A1c
q
Reproductive
r
Post-Reproductive

Figure 14: In-culture behavior of native islets across donor groups and conceptual comparison to pseudo-islets.(**a**) Conceptual model of temporal behavior for pseudo-islets (top) and native islets (bottom). (**b**) Data normalization strategy: Native islets are normalized to the number of IEQs seeded, whereas pseudo-islets are normalized to the number of single cells seeded. Because of this difference, the interpretation of cluster counts is not interchangeable between the two preparations. To visualize behavior over time, changes in the smallest islet size bin (30–60 μm diameter) are shown in c–f and k–n. Increases within this bin indicate fragmentation of larger clusters and mirror trends observed at larger sizes. The percentage of subclusters, normalized to control, is shown in g–j and o–r. (**c, d**) Mean cluster counts for male and female donors under control (black), + 0.1 μg/mL GCG (pink), and 0.1 μg/mL GLP-1 (teal). (**e, f**) Mean cluster counts for obese and non-obese donors under the same conditions. (**g, h**) Percent subclusters over time for male and female donors, normalized to control. (**i, j**) Percent subclusters over time for obese and non-obese donors, normalized to control. (**k, l**) Mean cluster counts for donors with elevated vs. normal A1c under control, GCG, and GLP-1. (**m, n**) Mean cluster counts for donors of reproductive age vs. post-reproductive age under the same conditions. (**o, p**) Percent subclusters over time for elevated vs. normal A1c cohorts, normalized to control. (**q, r**) Percent subclusters over time for reproductive vs. post-reproductive age cohorts, normalized to control. Unless stratified by sex, all groups include both female and male donors. Statistical significance was assessed by two-way ANOVA. P-values for significant comparisons ($\alpha = 0.05$) are shown on the graphs. Error bars represent SEM.

3.3.4.1 Stratification by donor sex

Based on our 2-3 days post-seeding observations, it appears that pseudo-islet formation is quick, as all islet sizes were already detectable. Additionally, pseudo-islets don't continue to form clusters indefinitely, or until all single cells are part of a cluster (as initially expected) but can also undergo fragmentation. Whether we see growth or fragmentation seems to depend on the cellular makeup, donor characteristics, and the type of media supplementation. For example, female-derived β+δ pseudo-islets show increasing counts of 30-60 μm clusters, whereas 150-300 μm clusters completely disappear by day 10 for + GCG or day 14 for basal conditions (Fig. 15b). This observation would suggest that those islets fragment over time in culture, just like native islets would. However, when checking the % of subclusters, the picture is different. Here, we observe that the percentage of subclusters normalized to basal conditions remains under 100 %, indicating no additional subcluster formation in the + GCG condition (Fig. 15j and Table 6). Together, this suggests that β+δ pseudo-islets + GCG favor smaller clusters over time in culture (larger clusters fragment over time but the smaller ones formed seem to stabilize). In contrast, male β+δ pseudo-islets do not lose 150-300 μm clusters over time, suggesting absent or at least slower fragmentation compared to females (Fig. 15d). There is some fluctuation observable for the 30-60 μm clusters (Fig. 15h), but 60-150 and 150-300 μm stay stable over time. Additionally, the percentage of subclusters in the + GCG condition remains below that in the basal condition, suggesting no additional subcluster formation compared to the CTRL condition (Fig. 15l and Table 6).

However, monitoring different sizes under different conditions over time is challenging and may lead to misinterpretations. Therefore, we used the smallest cluster size (30-60 μm in diameter) and monitored its growth over time as a proxy for the behavior of the bigger clusters (as was done for native islets) (Fig. 15e-h). In combination with the % of subclusters (Fig. 15i-l), we can conclude about formation vs. fragmentation and cluster stability. Remaining with the β+δ pseudo-islet example, female-donor-derived pseudo-islets show cluster increases over time, with + GCG trending towards compacted clusters compared to CTRL conditions (up to 120 % difference between the conditions) (Fig. 15f). The percentage of subclusters for + GCG remained stable under 100 % (Fig. 15j), suggesting absent fragmentation but also no further growth of formerly < 30 μm clusters into clusters > 30 μm. Male-donor-derived β+δ pseudo-islets show decreased counts (68.75 % for CTRL and 58.9 % for + GCG, compared to day 2, Fig. 15h), with similar compactness. On day 10 in culture, the + GCG condition was found increased compared to CTRL (+ 62.2 %), accompanied by a decrease in % subclusters (Fig. 15l), suggesting the formation of new clusters that formerly were counted as < 30 μm in diameter. Based on the combined analysis of mean cluster counts, percentage of subclusters, and growth within the 30–60 μm range, both male- and female-derived β+δ pseudo-islets showed evidence of cluster formation and subsequent stabilization over time (Fig. 15f and h). In female-derived pseudo-islets, cluster counts increased over time under both CTRL and + GCG conditions, suggesting the formation of many small aggregates. GCG supplementation promoted the development of more compact structures compared to CTRL, but prolonged culture did not indicate further fusion of small (< 30 μm) clusters into larger (> 30 μm) ones. Male-derived pseudo-islets, in contrast, showed a gradual reduction in cluster counts over time, consistent with ongoing compaction. Under + GCG conditions (especially long term), this effect was more pronounced, with evidence suggesting that small clusters contributed to the formation of larger aggregates. Our observations for all other conditions tested while stratifying by sex are summarized in Table 6.

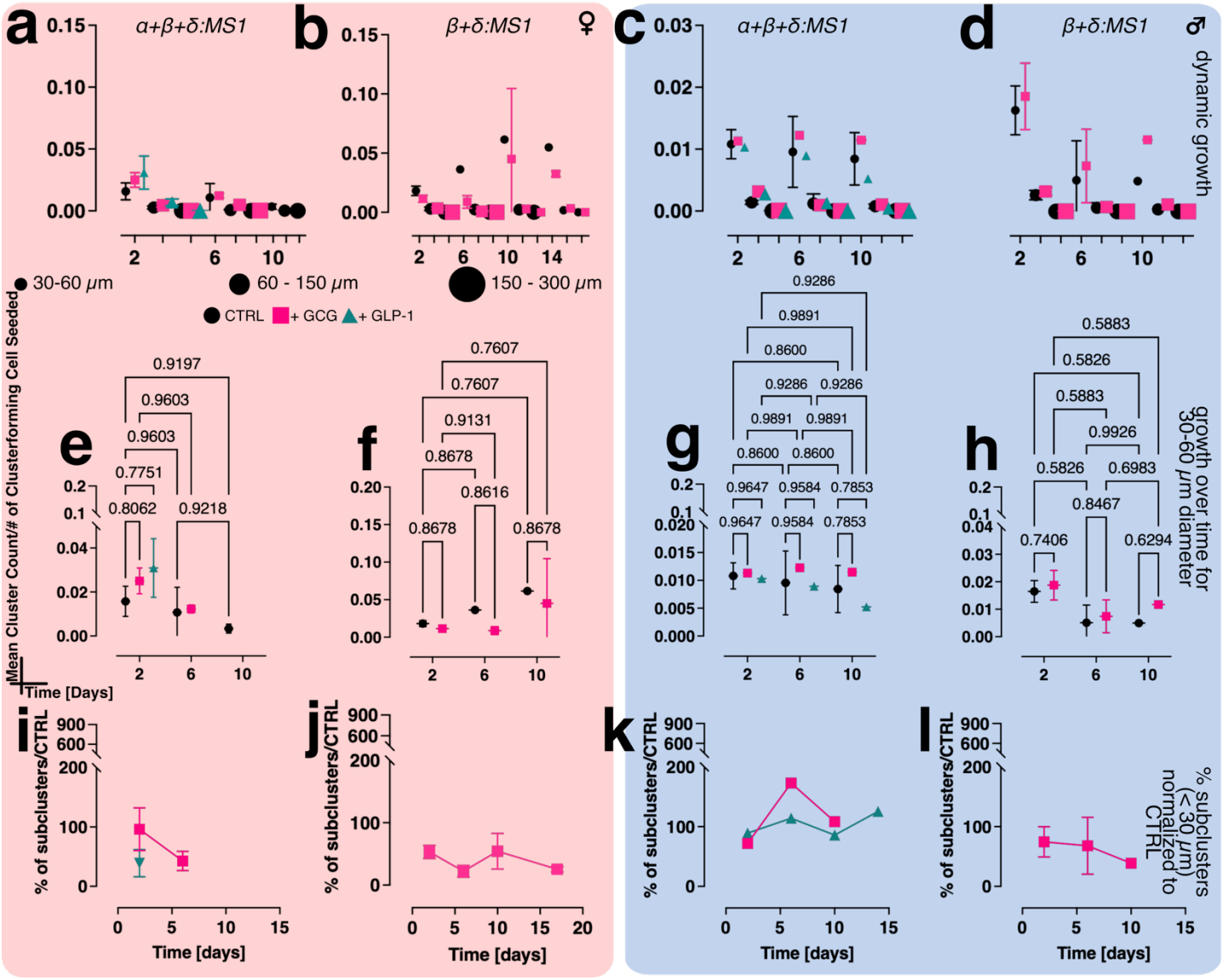

Figure 15: In-culture behavior of pseudo-islets from sex-stratified donors.

In contrast to native islets, pseudo-islets self-assemble following cell seeding. The mean cluster count, normalized to the number of cluster-forming cells seeded, serves as an indicator of cluster morphology: higher normalized counts reflect the formation of numerous small clusters, whereas lower counts indicate fewer but larger aggregates. As an additional measure of cluster stability, the percentage of subclusters (normalized to the control condition, CTRL) was monitored. Values < 100% suggest increased stability (reduced fragmentation), while values > 100% indicate fragmentation. The smallest cluster size (30–60 μm in diameter) was used as a proxy for dynamic cluster behavior. An increase in mean cluster count within this size bin suggests the appearance of new small clusters; if accompanied by increased subcluster percentage, this implies fragmentation of larger clusters. Conversely, a decrease in this bin, particularly when coupled with stable or reduced subcluster percentage, suggests the formation of larger, more stable clusters. (**a–d**) Dynamic cluster growth over time for α+β+δ pseudo-islets (**a**, female and **c**, male) and β+δ pseudo-islets (**b**, female and **d**, male) under CTRL (black), +0.1 μg/mL GCG (pink), and +0.1 μg/mL GLP-1 (teal) conditions. Symbol size represents cluster diameter (small: 30–60 μm; medium: 60–150 μm; large: 150–300 μm). (**e–h**) Mean cluster counts over time (days) for the smallest size bin (30–60 μm), normalized to the number of seeded cluster-forming cells, for α+β+δ (**e**, female; **g**, male) and β+δ (**f**, female; **h**, male) pseudo-islets under CTRL (black), +GCG (pink), and +GLP-1 (teal). (**i–l**) Percentage of subclusters (<30 μm), normalized to CTRL, for α+β+δ (**i**, female; **k**, male) and β+δ (**j**, female; **l**, male) pseudo-islets with +GCG (pink) and +GLP-1 (teal). Statistical comparisons were performed using two-way ANOVA or mixed-effects models, depending on data availability. p-values for all comparisons are indicated, with significance defined as $p < 0.05$. Error bars represent the standard error of the mean (SEM).

Table 6: Pseudo-islet growth and formation across donor sex. Pseudo-islet growth dynamics and subcluster composition (% subclusters) are stratified by donor sex. Data are shown for different cell type combinations, media supplementations, and observation time points (days post-seeding). The interpretation column guides how fluctuations in growth and subcluster proportions can be understood in the context of pseudo-islet formation.

Donor Sex	Cell type combination	Media supplementation	Time post-seeding	Mean cluster count (dynamic growth)	% subclusters	Interpretation
Female	α+β+δ:MS1	None	2-3 days	0.0157	100	Baseline
Male				0.0108	100	
Female		+ GCG		0.0250	96.1	
Male				0.0113	71.9	
Female		+ GLP-1		-	-	
Male				0.0103	89.2	
Female		None	6-7 days	0.0107	100	-
Male				0.0095	100	-
Female		+ GCG		0.0122	42.6	Cluster ⇓ % subcluster ⇓ = fusion into larger clusters
Male				0.0122	172.9	Cluster ⇑ % subcluster ⇑ = increased formation of small aggregates
Female		+ GLP-1		-	-	-
Male				0.0089	114.1	Cluster ⇓ % subcluster ⇑ = fragmentation
Female		None	9-10 days	-	-	-
Male				0.0084	100	-
Female		+ GCG		-	-	-
Male				0.0114	108.3	Cluster ⇓ % subcluster ⇓ = fusion into larger clusters
Female		+ GLP-1		-	-	-
Male				0.0052	85.9	Cluster ⇓ % subcluster ⇓ = fusion into larger clusters
Female	β+δ:MS1	None	2-3 days	0.0181	100	Baseline
Male				0.0165	100	
Female		+ GCG		0.0114	53.2	
Male				0.0188	74.6	
Female		None	6-7 days	0.0362	100	-
Male				0.0051	100	-
Female		+ GCG		0.0088	22.2	Cluster ⇓ % subcluster ⇓ = fusion into larger clusters
Male				0.0074	68	Cluster ⇓ % subcluster ⇓ = fusion into larger clusters
Female		None	9-10 days	0.0615	100	-
Male				0.0049	100	-
Female		+ GCG		0.0450	54.3	Cluster ⇑ % subcluster ⇑ = increased formation of small aggregates
Male				0.0117	38.7	Cluster ⇑ % subcluster ⇓

						= shift toward larger clusters
Female	α+β:MS1	None	2-3 days	0.0029	100	Baseline
Male				0.0147	100	
Female		+ GCG		0.0148	334	
Male				0.0086	33.1	
Female		+ GLP-1		0.0023	370.5	
Male				0.0107	60.5	
Female		None	6-7 days	0.0044	100	-
Male				0.0050	100	-
Female		+ GCG		0.0031	48	Cluster ⇓ % subcluster ⇓ = fusion into larger clusters
Male				0.0049	65	Cluster ⇓ % subcluster ⇑ = fragmentation
Female		+ GLP-1		0.0203	173.8	Cluster ⇑ % subcluster ⇓ = shift toward larger clusters
Male				0.0087	193.2	Cluster ⇓ % subcluster ⇑ = fragmentation
Female		None	9-10 days	0.0035	100	-
Male				-	-	-
Female		+ GCG		-	-	-
Male				-	-	-
Female		+ GLP-1		0.0016	686.6	Cluster ⇓ % subcluster ⇑ = fragmentation
Male				0.0101	-	-

Briefly, our results indicate that both female- and male-derived pseudo-islets respond to GCG and GLP-1 supplementation during early stages of pseudo-islet formation, with evidence of increased aggregation or maturation depending on the condition. However, over longer culture periods (9–10 days), signs of fragmentation emerge, particularly in female-derived pseudo-islets treated with GLP-1. Increased subcluster percentages and a decline in cluster counts indicate this. In male-derived pseudo-islets, fragmentation tends to occur earlier, often by 6–7 days and is especially pronounced in the + GLP-1 condition, whereas + GCG can have stabilizing effects. These findings suggest that the structural trajectory of pseudo-islets is both sex-dependent and hormone-specific, but particularly dependent on the cell combinations used to generate pseudo-islets.

3.3.4.2 Stratification by donor BMI

For native islets, donor BMI strongly influenced fragmentation dynamics. In obese donors, baseline cluster counts were higher (30 μm, $\mu \sim 2.1$) compared to non-obese, reflecting early fragmentation of larger aggregates. Over time, fragmentation increased further, with a marked surge in small islets by day 10 (~ 176 % increase compared to CTRL) (Fig. 14e vs. f). Glucagon enhanced fragmentation at baseline (30 μm, $\mu \sim 2.8$, % subclusters day 2: $\mu = 90.8 \pm 61.3$) but subsequently attenuated late-stage disintegration, yielding stable fragments (~ 70 % increase by day 10 compared to CTRL, % subclusters day 10: $\mu = 88.6 \pm 2.3$) (Fig. 14e and i). GLP-1 provided the most consistent benefit in this group, reducing both fragmentation and subcluster burden across time (30 μm, $\mu \sim 2.1$, % subclusters day 2: $\mu = 82.5 \pm 53.5$, day 10: + ~ 109 % compared to CTRL, % subclusters day 10: $\mu = 84.3 \pm 0.76$) (Fig. 14e and i). In contrast, non-obese donors showed lower baseline fragmentation (30 μm: CTRL $\mu \sim 1.5$, + GCG $\mu \sim 1.6$, + GLP-1 $\mu \sim 1.6$) and relative stability through day 6 (30 μm: CTRL $\mu \sim 1.5$, + GCG $\mu \sim 2$, + GLP-1 $\mu \sim 2.4$), but a pronounced increase in fragmentation by day 10 (increase compared to CTRL: ~ 95 % CTRL, ~ 57 % + GCG, ~ 145 % + GLP-1) (Fig. 14f and j). In this group, GCG promoted progressive instability, while GLP-1 induced the highest degree of fragmentation and subcluster formation (% subclusters day 2 vs. 10: + GCG $\mu = 114 \pm 35.2$ vs. $\mu = 132 \pm 22.7$ and + GLP-1 $\mu = 135 \pm 32.3$ vs. $\mu = 130 \pm 27.8$), particularly at mid-stage culture (Fig. 14f and j).

For pseudo-islets, donor BMI markedly influenced cluster formation dynamics (see Table 7 for details). Non-obese donors displayed pronounced remodeling capacity, characterized by robust early cluster formation in response to supplementation. GCG induced strong early growth associated with transient fragmentation but was followed by a marked decline in subclusters, indicating progressive structural stabilization over time (% subclusters day early vs. late: α+β+δ + GCG $\mu = 141 \pm 33.583$ vs. $\mu = 38 \pm 8.729$, β+δ + GCG: $\mu = 98 \pm 35.199$ vs. $\mu = 19 \pm 11.839$, α+β + GCG: $\mu = 67 \pm 17.417$ vs. $\mu = 60 \pm 14.632$). GLP-1 induced extensive cluster formation with reduced subcluster burden initially but

ultimately led to over-fragmentation at later stages (% subclusters day early vs. late: α+β+δ + GLP-1: μ = 79 ± 15.399 vs. μ = 117 ± 28.018, α+β + GLP-1: μ = 122 ± 35.538 vs. μ = 978 ± 251.876). Over time, non-obese pseudo-islets transitioned from expansion to consolidation, reflecting an active yet stage- and supplementation-dependent remodeling process. In contrast, pseudo-islets from obese donors exhibited higher baseline cluster counts, suggesting dispersion and smaller initial aggregates, but showed limited remodeling thereafter. GCG generally suppressed further cluster formation and occasionally promoted fragmentation (% subclusters day early vs. late: α+β+δ + GCG μ = 65 ± 24.261 vs. μ = 99 ± 0.817), whereas GLP-1 supported moderate growth without inducing notable instability, although subcluster count data here were limited. Collectively, these findings indicate that non-obese donor pseudo-islets retain high plasticity and responsiveness to hormonal stimuli, while obese donor pseudo-islets show reduced adaptability and a tendency toward structural stabilization rather than dynamic reorganization.

Table 7: Pseudo-islet growth and formation across donor BMI. Pseudo-islet growth dynamics and subcluster composition (% subclusters) are stratified by donor BMI, grouped with the cut-off of 30 kg/m^2. Data are shown for different cell type combinations, media supplementations, and observation time points (days post-seeding). The interpretation column guides how fluctuations in growth and subcluster proportions can be understood in the context of pseudo-islet formation.

Donor BMI	Cell type combination	Media supplementation	Time post-seeding	Mean cluster count (dynamic growth)	% subclusters	Interpretation
Non-obese	α+β+δ:MS1	None	2-3 days	0.0046	100	baseline
Obese				0.0064	100	
Non-obese		+ GCG		0.0120	141	Cluster ⇑⇑ % subcluster ⇑⇑ = strong growth
Obese				0.0030	65	Cluster ⇓ % subcluster ⇓ = impaired growth/reduced stability
Non-obese		+ GLP-1		0.0112	15	Cluster ⇑⇑ % subcluster ⇓⇓ = robust growth, fewer subclusters
Obese				0.0073	23	Cluster ⇑ % subcluster ⇓ = moderate growth, reduced subclusters
Non-obese		None	6-7 days	0.0058	100	baseline

Obese				0.0032	100	
Non-obese		+ GCG		0.0120	38	Cluster ⇑⇑ % subcluster ⇓ = enhanced growth
Obese				0.0028	123	Cluster ⇓ % subcluster ⇑⇑ = fragmentation
Non-obese		+ GLP-1		0.0034	43	Cluster ⇓ % subcluster ⇓ = reduced growth, fewer subclusters
Obese				0.0073	-	-
Non-obese		None	9-10 days	0.0014	100	baseline
Obese				0.0042	100	
Non-obese		+ GCG		-	-	-
Obese				0.0042	99	Cluster ⇑ % subcluster ⇒ = moderate growth, unknown stability
Non-obese		+ GLP-1		0.0019	28	Cluster ⇓ % subcluster ⇓⇓ = reduced growth, reduced fragmentation
Obese				-	-	-
Non-obese	β+δ:MS1	None	2-3 days	0.0059	100	baseline
Obese				0.0083	100	
Non-obese		+ GCG		0.0064	98	Cluster ⇑ % subcluster ⇒ = moderate growth
Obese				0.0055	42	Cluster ⇓ % subcluster ⇓ = reduced growth
Non-obese		None	6-7 days	0.0019	100	baseline
Obese				-	-	
Non-obese		+ GCG		0.0011	19	Cluster ⇓⇓ % subcluster ⇓ = impaired growth; likely fragmentation
Obese				0.0043	-	Cluster ⇑ % subcluster ? = modest growth; unknown stability
Non-obese		None	9-10 days	0.0018	100	baseline
Obese				-	-	
Non-obese		+ GCG		-	-	-
Obese				-	-	-

Non-obese	α+β:MS1	None	2-3 days	0.0025	100	baseline
Obese				0.0122	100	
Non-obese		+ GCG		0.0026	67	Cluster ⇓ % subcluster ⇓ = low growth
Obese				-	-	-
Non-obese		+ GLP-1		0.0025	123	Cluster ⇓ % subcluster ⇑⇑ = impaired growth; likely fragmentation
Obese				-	-	-
Non-obese		None	6-7 days	0.0022	100	baseline
Obese				-	-	
Non-obese		+ GCG		0.0019	60	Cluster ⇓ % subcluster ⇓ = low growth; fewer subclusters
Obese				-	-	-
Non-obese		+ GLP-1		0.0034	178	Cluster ⇑ % subcluster ⇑⇑⇑ = strong fragmentation
Obese				-	-	-
Non-obese		None	9-10 days	-	-	-
Obese				-	-	-
Non-obese		+ GCG		-	-	-
Obese				-	-	-
Non-obese		+ GLP-1		0.0037	978	Cluster ⇑ % subcluster ⇑⇑⇑⇑ = extreme fragmentation
Obese				-	-	-

3.3.4.3 Stratification by donor hemoglobin A1c levels

Consistent with the BMI-based analysis, stratification of donors by A1c status, using a cutoff of 5.7 % to define normal vs. elevated levels, revealed a fragmentation pattern indicative of increased plasticity in normal A1c (< 5.7 %) and decreased adaptability for donors of the elevated group (Fig. 14k and l). Normal A1c donors showed progressive fragmentation over time, reflecting the ongoing breakdown of larger aggregates. Both + GCG and + GLP-1 provided transient stabilization at mid-stage (day 6, % subclusters + GCG: $\mu = 68.1 \pm 35.4$, + GLP-1: $\mu = 71 \pm 35.3$), but by day 10, both hormones enhanced

fragmentation and instability (day 10, % subclusters + GCG: μ = 115.3 ± 27.2, + GLP-1: μ = 120.9 ± 28.8) (Fig. 14k and o).

In contrast, islets from donors with elevated A1c (> 5.7%) responded poorly to supplementation. Both GCG and GLP-1 induced fragmentation, most dramatically at day 2 and day 10, with GLP-1 driving particularly high instability at day 6 (Fig. 14l and p). Together, these findings indicate that while normal A1c islets retain dynamic remodeling capacity with temporary stabilization under supplementation, elevated A1c islets are intrinsically more fragile, destabilizing rapidly and severely when exposed to GCG or GLP-1.

For pseudo-islets, clear differences emerged when stratified by donor A1c (see Table 8 for details). Donors with normal A1c (< 5.7 %) displayed dynamic remodeling capacity, with cluster counts stabilizing at mid-stage (6 days in culture) before increasing again at later time points, consistent with fragmentation over time in culture. GCG and GLP-1 both reduced subclusters at baseline, indicating early stabilization, but these effects disappeared with time, as + GCG promoted fragmentation by day 6 and GLP-1 showed variable effects. In contrast, donors with elevated A1c (> 5.7 %) exhibited lower cluster counts at baseline and a blunted trajectory over time, reflecting impaired plasticity. While GCG occasionally reduced subclusters, suggesting transient stabilization, it more often destabilized clusters, particularly in β+δ:MS1 pseudo-islets at day 6. GLP-1 had minimal or inconsistent benefit in this group, with cluster counts largely remaining low and stable across time. Together, these findings indicate that normal A1c donors retain the capacity for time-dependent remodeling, while elevated A1c donors form fewer aggregates that are less able to remodel or stabilize under supplementation.

Table 8: Pseudo-islet growth and formation across donor A1c. Pseudo-islet growth dynamics and subcluster composition (% subclusters) are classified by donor A1c, using a cutoff of 5.7 %. Values below 5.7 % are considered normal, while those above are regarded as elevated or pre-diabetic. Data are presented for various cell type combinations, media supplements, and observation time points (days after seeding). The interpretation column offers guidance on how changes in growth and subcluster proportions can be understood in the context of pseudo-islet formation.

Donor A1c	Cell type combination	Media supplementation	Time post-seeding	Mean cluster count (dynamic growth)	% subclusters	Interpretation

Normal (A1c < 5.7 %)	α+β+δ:MS1	None	2-3 days	0.0059	100	baseline
Elevated (A1c > 5.7 %)				0.0042	100	
Normal (A1c < 5.7 %)		+ GCG		0.0071	64	
Elevated (A1c > 5.7 %)				0.012	117	
Normal (A1c < 5.7 %)		+ GLP-1		0.0057	51	
Elevated (A1c > 5.7 %)				0.018	61	
Normal (A1c < 5.7 %)		None	6-7 days	0.0031	100	-
Elevated (A1c > 5.7 %)				0.0066	100	-
Normal (A1c < 5.7 %)		+ GCG		0.0028	123	Cluster ⇓ % subclusters ⇑⇑ = fragmentation
Elevated (A1c > 5.7 %)				0.012	43	Cluster ⇒ % subclusters ⇓⇓ = stable
Normal (A1c < 5.7 %)		+ GLP-1		0.0052	81	Cluster - % subclusters ⇑ = some fragmentation
Elevated (A1c > 5.7 %)				0.017	-	Cluster ⇒ % subclusters - = stable
Normal (A1c < 5.7 %)		None	9-10 days	0.0031	100	-
Elevated (A1c > 5.7 %)				0.0013	100	-
Normal (A1c < 5.7 %)		+ GCG		0.0042	99	Cluster ⇓ % subclusters ⇑ = some fragmentation
Elevated (A1c > 5.7 %)				-	-	-
Normal (A1c < 5.7 %)		+ GLP-1		0.0019	79	Cluster ⇓ % subclusters ⇑ = some fragmentation
Elevated (A1c > 5.7 %)				-	-	-
Normal (A1c < 5.7 %)	β+δ:MS1	None	2-3 days	0.0074	100	baseline
Elevated (A1c > 5.7 %)				0.0042	100	
Normal (A1c < 5.7 %)		+ GCG		0.0055	63	
Elevated (A1c > 5.7 %)				0.0011	78	
Normal (A1c < 5.7 %)		None	6-7 days	0.0035	100	-

Elevated (A1c > 5.7 %)				0.0002	100	-
Normal (A1c < 5.7 %)		+ GCG		0.0043	-	Cluster ⇓ % subclusters - = cluster merging, stability?
Elevated (A1c > 5.7 %)				0.0011	139	Cluster ⇒ % subclusters ⇑⇑ = fragmentation
Normal (A1c < 5.7 %)		None	9-10 days	0.0114	100	-
Elevated (A1c > 5.7 %)				-	100	-
Normal (A1c < 5.7 %)		+ GCG		0.0109	-	Cluster ⇑⇑ % subclusters - = many small clusters, stability?
Elevated (A1c > 5.7 %)				0.0011	-	Cluster ⇒ % subclusters - = stability?
Normal (A1c < 5.7 %)	α+β:MS1	None	2-3 days	0.0098	100	baseline
Elevated (A1c > 5.7 %)				0.0011	100	
Normal (A1c < 5.7 %)		+ GCG		0.0057	42	
Elevated (A1c > 5.7 %)				0.0011	-	
Normal (A1c < 5.7 %)		+ GLP-1		0.0043	76	
Elevated (A1c > 5.7 %)				0.0007	-	
Normal (A1c < 5.7 %)		None	6-7 days	0.0033	100	-
Elevated (A1c > 5.7 %)				-	-	-
Normal (A1c < 5.7 %)		+ GCG		0.002	44	Cluster ⇓ % subclusters ⇒ = merging into larger clusters
Elevated (A1c > 5.7 %)				-	-	-
Normal (A1c < 5.7 %)		+ GLP-1		0.0034	131	Cluster ⇓ % subclusters ⇑⇑ = fragmentation
Elevated (A1c > 5.7 %)				-	-	-
Normal (A1c < 5.7 %)		None	9-10 days	-	-	-
Elevated (A1c > 5.7 %)				0.0011	-	-
Normal (A1c < 5.7 %)		+ GCG		-	-	-

Elevated (A1c > 5.7 %)				-	-	-
Normal (A1c < 5.7 %)		+ GLP-1		0.0037	-	Cluster ⇓ % subclusters - = merging into larger clusters
Elevated (A1c > 5.7 %)				0.0006	-	Cluster ⇓ % subclusters - = merging into larger clusters

3.3.4.4 Stratification by donor age

Native islets from donors < 50 years showed high baseline fragmentation at day 2, particularly in small islets, consistent with early breakdown of larger aggregates into smaller fragments. Over time, fragmentation declined by day 6, reflecting transient stabilization, but increased again by day 10 (Fig. 14m). However, CTRL condition fragmentation remained below the fragmentation levels observed for + GCG and + GLP-1. Glucagon consistently increased fragmentation, whereas GLP-1 exerted a transient stabilizing effect at early and mid-time points but failed to prevent late-stage fragmentation. Subcluster data confirmed these observations (% subcluster at day 2: + GCG μ = 104.8 ± 41.9, + GLP-1 μ = 70.8 ± 27.6, day 6: + GCG μ = 48.3 ± 41.1, + GLP-1 μ = 61.2 ± 49, day 10: + GCG μ = 119.2 ± 65.5, + GLP-1 μ = 132.1 ± 70.2) (Fig. 14q).

In contrast, islets from donors > 50 years showed lower baseline fragmentation at day 2 and remained relatively stable through day 6, suggesting reduced plasticity compared to younger donors. By day 10, however, fragmentation rose sharply, indicating the breakdown of larger islets. Although not to the same levels as reproductive donors (Fig. 14n). Again, supplementation did not improve outcomes: GCG promoted fragmentation compared to control conditions. However, % subclusters remained stable, although > 100 %, suggesting increased fragmentation compared to CTRL conditions (% subcluster at day 2: + GCG μ = 150.9 ± 53.2, day 6: + GCG μ = 137.7 ± 45, day 10: + GCG μ = 131.7 ± 22.7). GLP-1 consistently promoted fragmentation over time in culture with a sharp increase at day 10. Subcluster

percentages were over 200 % suggesting significantly higher fragmentation rates compared to CTRL and + GCG conditions. However, at day 10, there is a sharp decrease to ~ 130 % (matching + GCG levels), indicative of some stabilization (% subcluster at day 2: + GLP-1 μ = 208.2 ± 67.4, day 6: + GLP-1 μ = 232.8 ± 61.6, day 10: + GLP-1 μ = 131.8 ± 25.4) (Fig. 14r).

For pseudo-islets, distinct differences in cluster formation were observed (see Table 9 for details). Donors < 50 years showed robust cluster formation at baseline (day 2), with high cluster counts indicative of many small aggregates. Over time, the number of clusters declined, reflecting consolidation into fewer, larger structures. Supplementation modulated this trajectory: GCG generally promoted stabilization by reducing fragmentation, whereas GLP-1 had stage-dependent effects. Initially, GLP-1 reduced subclusters but later induced fragmentation before ultimately supporting consolidation at later stages. In contrast, donors > 50 years exhibited markedly reduced cluster formation from the start, with few aggregates that failed to expand or stabilize over time. GCG provided partial rescue at early stages but often at the expense of stability, while GLP-1 had little to no benefit.

Table 9: Pseudo-islet growth and formation across donor age. Pseudo-islet growth dynamics and subcluster composition (% subclusters) are stratified by donor age, grouped with the cut-off of 50 years. Data are shown for different cell type combinations, media supplementations, and observation time points (days post-seeding). The interpretation column guides understanding of fluctuations in growth and subcluster proportions within the context of pseudo-islet formation.

Donor Age	Cell type combination	Media supplementation	Time post-seeding	Mean cluster count (dynamic growth)	% subclusters	Interpretation
< 50 years	α+β+δ:MS1	None	2-3 days	0.0072	100	baseline
> 50 years				0.0016	100	
< 50 years		+ GCG		0.0081	124	
> 50 years				0.0076	-	
< 50 years		+ GLP-1		0.0099	59	
> 50 years				-	-	
< 50 years		None	6-7 days	0.0078	100	-
> 50 years				0.0021	100	-
< 50 years		+ GCG		0.0088	105	Cluster ⇑ % subclusters ⇑ = mild fragmentation

> 50 years				-	-	-
< 50 years		+ GLP-1		0.0096	122	Cluster ⇑ % subclusters ⇑ = fragmentation
> 50 years				-	-	-
< 50 years		None	9-10 days	0.0031	100	-
> 50 years				-	-	-
< 50 years		+ GCG		0.0042	99	Cluster ⇓ % subclusters ⇒ = promoting stability
> 50 years				-	-	-
< 50 years		+ GLP-1		0.0019	79	Cluster ⇓ % subclusters ⇓ = stabilization with fewer larger clusters
> 50 years				-	-	-
< 50 years	β+δ:MS1	None	2-3 days	0.0076	100	baseline
> 50 years				0.0004	100	
< 50 years		+ GCG		0.0055	90	
> 50 years				0.0012	54	
< 50 years		None	6-7 days	0.0035	100	-
> 50 years				0.0002	100	-
< 50 years		+ GCG		0.0043	23	Cluster ⇓ % subclusters ⇓⇓ = formation of fewer, larger clusters
> 50 years				0.0011	204	Cluster ⇑ % subclusters ⇑⇑ = fragmentation
< 50 years		None	9-10 days	0.0018	100	-
> 50 years				-	-	-
< 50 years		+ GCG		0.0043	30	Cluster ⇓ % subclusters ⇓⇓ = formation of fewer, larger clusters
> 50 years				-	-	-
< 50 years	α+β:MS1	None	2-3 days	0.0098	100	baseline
> 50 years				0.0012	100	
< 50 years		+ GCG		0.0057	44	

> 50 years				0.0011	-	
< 50 years		+ GLP-1		0.0043	81	
> 50 years				0.0008	-	
< 50 years		None	6-7 days	0.0033	100	-
> 50 years				0.0002	100	-
< 50 years		+ GCG		0.002	56	Cluster ⇓ % subclusters ⇓ = formation of fewer, larger clusters
> 50 years				-	-	-
< 50 years		+ GLP-1		0.0037	165	Cluster ⇓ % subclusters ⇑ = fragmentation
> 50 years				-	-	-
< 50 years		None	9-10 days	-	-	-
> 50 years				-	-	-
< 50 years		+ GCG		-	-	-
> 50 years				-	-	-
< 50 years		+ GLP-1		0.0037	-	-
> 50 years				-	-	-

To determine whether the observed effects between the different stratification approaches might be driven by donor sex, we examined the sex distribution within each stratification. For BMI-stratified donors, the non-obese group comprised 11 females and 9 males, whereas the obese group consisted of 6 females and 8 males (see Table 10 and Venn (180) diagram in Fig. 16a-c). To assess whether sex and obesity were associated in this cohort, we applied Fisher's exact test, which is well-suited for small sample sizes and evaluates whether the overlap between categorical variables (*e.g.*, sex vs. BMI) exceeds that expected by chance. In this analysis, the observed obesity rates (~ 35 % in females and ~

47 % in males) yielded a p-value of 0.7283, indicating that sex and obesity are likely independent in this donor population.

Table 10: Contingency table for donor sex crossed with donor BMI. To evaluate the contribution of donor sex to the effect seen when donors were stratified by BMI, donor sex and donor BMI groups were crossed, resulting in the following contingency table.

Donor Sex	Non-obese	Obese	Total
Female	11	6	17
Male	9	8	17
Total	20	14	34

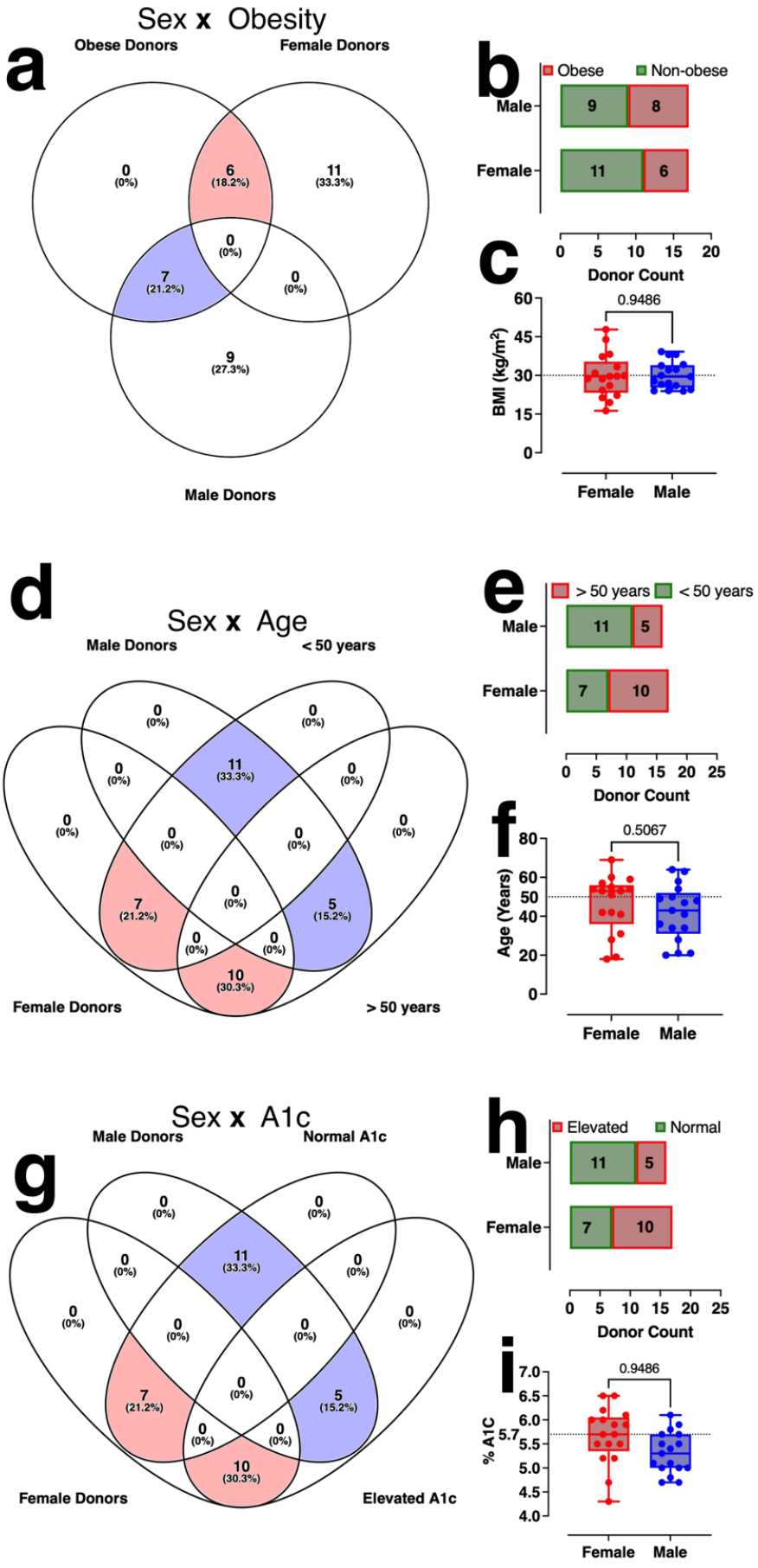
Sex x Obesity
a
Obese Donors
Female Donors
Male Donors
0 (0%)
6 (18.2%)
11 (33.3%)
0 (0%)
7 (21.2%)
0 (0%)
9 (27.3%)
b
Obese
Non-obese
Male
Female
9
8
11
6
0 5 10 15 20
Donor Count
c
0.9486
BMI (kg/m²)
60
45
30
15
0
Female
Male
d
Sex x Age
Male Donors
< 50 years
Female Donors
> 50 years
11 (33.3%)
7 (21.2%)
5 (15.2%)
10 (30.3%)
e
> 50 years
< 50 years
Male
Female
11
5
7
10
0 5 10 15 20 25
Donor Count
f
0.5067
Age (Years)
80
60
50
40
20
0
Female
Male
g
Sex x A1c
Male Donors
Normal A1c
Female Donors
Elevated A1c
11 (33.3%)
7 (21.2%)
5 (15.2%)
10 (30.3%)
h
Elevated
Normal
Male
Female
11
5
7
10
0 5 10 15 20 25
Donor Count
i
0.9486
% A1C
7.0
6.5
6.0
5.7
5.5
5.0
4.5
4.0
Female
Male

Figure 16: Human Islet Donor Cohort Overview and Cross Analysis. Four donor characteristics: sex, BMI, age, and A1c were picked to stratify donors. Each of these characteristics was additionally crossed with sex to identify potential cross-correlations. (**a-c**) Donor sex crossed with donor BMI. (**a**) Venn diagram showing the overlap between male and female donors with the obese group. (**b**) female/male donor counts, grouped by BMI (non-obese (green) vs. obese (red)). (**c**) donor cohort BMI values (y-axis) over gender (x-axis), with grouping value at 30 kg/m^2. Each point corresponds to one donor. (**d-f**) female/male donor counts, grouped by age (< 50 years (green) vs. > 50 years (red)). (**d**) Venn diagram showing the overlap between male and female donors with the age groups. Red fields highlight the female overlap and blue fields the male overlap. (**e**) donor cohort age values (y-axis) over gender (x-axis), with grouping value at 50 years. Each point corresponds to one donor. (**g-i**) female/male donor counts, grouped by A1c (< 5.7 % (green) vs. > 5.7 % (red)). (**g**) Venn diagram showing the overlap between male and female donors with the A1c groups. Red fields highlight the female overlap and blue fields the male overlap. (**h**) donor cohort A1c values (y-axis) over gender (x-axis), with grouping value at 5.7 %. Each point corresponds to one donor. Group comparison was performed by Fisher's exact test; p-values are indicated on the graph. 0.05 was chosen as the cutoff for statistical significance. Error bars represent SEM.

We performed the same comparison to donor sex for donor age and A1c as well (Table 11 and 12). The < 50 years group comprised 7 females and 11 males, whereas the > 50 years group consisted of 10 females and 5 males (see Table 11 and Venn (62) diagram in Fig. 16d-e). Fisher's exact test analysis revealed that ~ 59 % of females were > 50 years, for males this was only ~ 30 % with a p-value of 0.1663. This indicates that although the age distribution is quite different for the sexes, sex and age are likely independent in this donor population.

For the A1c groups, 7 females and 11 males had normal A1c, whereas 10 females and 5 males had elevated A1c values (see Table 12 and Venn (62) diagram in Fig. 16g-i). Fisher's exact test analysis revealed that ~ 59 % of females had elevated A1c, for males this was only ~ 30 % with a p-value of 0.1663. This indicates that although the A1c levels are quite different for the sexes, with more female donors being in the pre-diabetic range, sex and A1c are likely independent characteristics in this donor population.

Table 11: Contingency table for donor sex crossed with donor age. To evaluate the contribution of donor sex to the effect seen when donors were stratified by age, donor sex and donor age groups were crossed, resulting in the following contingency table.

Donor Sex	< 50 years	> 50 years	Total
Female	7	10	17
Male	11	5	16
Total	18	15	33

Table 12: Contingency table for donor sex crossed with donor A1c. To evaluate the contribution of donor sex to the effect seen when donors were stratified by A1c, donor sex and donor A1c groups were crossed, resulting in the following contingency table.

Donor Sex	Normal	Elevated	Total
Female	7	10	17
Male	11	5	16
Total	18	15	33

3.4 Discussion

The present findings demonstrate that donor characteristics markedly modulate the structural dynamics of both native and pseudo-islets in response to GCG or GLP-1 supplementation. Pseudo-islets thereby represent a versatile experimental system to investigate how external factors and intrinsic determinants, such as the specific cellular composition of the islet, shape islet organization and stability.

Because a fraction of β-cells can show CD9+ staining, CD9 was not used for phenotype calling, and distinction into β-cells and non-β-cells was done based on HIC1-8G12 positivity. Further, the FMO (A488 + PE - CD9) control validates that the β-cell gate remains biologically well-defined and “clean” of δ-cells (Appendix Fig. 1b).

Native islet behavior in culture is strongly influenced by donor characteristics (Fig. 14). For pseudo-islets, donor characteristics play a minor role. Here, the cellular makeup of the pseudo-islets was found to have a stronger effect on the in-culture behavior (Fig. 15). This is particularly well demonstrated by the functional omission of a certain cell type (absence model) (Section 3.3.3, Fig. 13). In the α-cell absence model, GCG supplementation led to reduced mean cluster counts, which is consistent with fewer, but larger clusters (compaction) effectively promoting cluster stabilization and expansion. This is consistent with GCG, normally secreted by the here-absent α-cells, being a paracrine cue that enhances cAMP/PKA signaling and hence is associated with survival (181). The selective GCG effect in obese and reproductive-age donors may reflect context-dependent differences in GCGR expression or differences in metabolic state and age, amplifying GCG responsiveness in these groups.

Interestingly, in the β-cell absence model, GLP-1 addition did not change clustering metrics, suggesting either no effect on this phenotype under these conditions or that any GLP-1–mediated influence is β-cell dependent. It has been shown that human β-cells show the highest functional GLP-1R signaling, removing them likely removes the dominant effector pathway for GLP-1–driven cAMP/adhesion

dynamics (182,183). Besides this genetic explanation, one must consider that long-term culture in a β-cell-depleted context may have induced changes in receptor expression or that GLP-1s effect is quick and transient and might therefore be missed. Further, effects that do not visualize themselves in terms of morphology, such as survival, proliferation, or extracellular matrix (ECM) remodeling, were not considered here. GLP-1 might influence viability, apoptosis, or cytoskeletal programs without changing gross cluster number.

Further supporting the notion that cellular composition has a dominant influence over donor characteristics in the context of pseudo-islets are the experiments modulating cell–cell ratios (Fig. 13u and v). When α-cell numbers were increased to match β-cell numbers in α+β+δ pseudo-islets, fewer but larger clusters were formed (Fig. 13v, pink), indicative of enhanced compaction. This likely reflects the higher levels of endogenous GCG produced by the expanded α-cell population, which modulates intercellular organization through paracrine signaling. Increasing δ-cell numbers to match β-cells led to even greater compaction, consistent with the inhibitory role of SST in dampening intra-islet signaling (Fig.13v, orange).

In α+β pseudo-islets at physiological ratios, GCG supplementation increased cluster counts, consistent with a more dispersed system (Fig. 13u, normal, black vs. pink). In contrast, when the α:β ratio was inverted, dispersion increased significantly under CTRL conditions, likely due to elevated endogenous GCG secretion from the increased α-cell population. Interestingly, exogenous GCG supplementation under these α-enriched conditions induced compaction rather than further dispersion. This suggests a threshold effect at which GCG signaling transitions from promoting dispersion to favoring consolidation. This may reflect a self-limiting property of GCG (184). Moreover, this effect appears composition-dependent, as increasing α-cell count in α+β+δ pseudo-islets (Fig. 13v, β=α, pink) resulted in compaction relative to CTRL but dispersion relative to δ-cell enriched pseudo-islets (β=δ, orange). This observation implies that δ cells, and consequently SST release, likely stimulated by GCG itself, modulated pseudo-

islet organization by counterbalancing GCG-driven dispersion through inhibitory feedback mechanisms.

Donor characteristics exerted a pronounced influence on the in-culture behavior of native islets. The observed differences are biologically plausible and consistent with expected physiological variability, underscoring the importance of donor stratification in interpreting islet culture outcomes. The strong influence of sex is consistent with accumulating evidence that endocrine cell function is shaped by sex-specific physiology. Female islets may require a greater degree of plasticity to adapt to frequent and cyclical hormonal fluctuations associated with the menstrual cycle, pregnancy, and menopause. These recurrent endocrine transitions may have evolved to favor dynamic regulatory programs in female islets, thereby conferring greater responsiveness to external cues (89,92). In contrast, male islets, which are exposed to relatively stable hormonal milieus, may rely on less flexible mechanisms of adaptation, leading to different patterns of islet fragmentation and remodeling under identical supplementation conditions. The additional effect of BMI further highlights the interplay between systemic metabolic state and intrinsic islet behavior, as obesity and insulin resistance impose chronic stress that may accentuate or blunt responsiveness to exogenous signals (167,168).

Mechanistically, the sex-specific differences likely arise from the influence of steroid hormones on β- and α-cell function (185,186). Estrogen signaling has been shown to enhance β-cell survival, increase insulin biosynthesis, and attenuate glucagon secretion, thereby contributing to improved glucose homeostasis under metabolic stress (89,153,186–188). Conversely, androgen exposure may exacerbate β-cell vulnerability and modulate glucagon release through distinct transcriptional programs (88,189,190). These sex-linked pathways may explain why female islets are more dynamic in their structural and functional responses to GCG or GLP-1. In addition, the observed role of BMI aligns with studies showing that obesity alters islet transcriptomic and secretory profiles, including genes related to stress adaptation, incretin signaling, and paracrine hormone interactions (167,191–193).

In contrast to native islets, pseudo-islets displayed markedly reduced sensitivity to donor-specific characteristics. While some influence of sex and BMI was observed, these effects were less pronounced and inconsistent across conditions. Instead, the cellular composition of pseudo-islets emerged as the primary determinant of their response to hormone supplementation. This observation suggests that, in reconstituted systems, the intercellular architecture and relative proportions of α-, β-, and δ-cells exert greater control over the collective outcome than do donor-specific features from which the cells were derived. The pseudo-islet environment may therefore override, or at least buffer, the imprint of donor variability, highlighting the central role of paracrine crosstalk and cellular make-up in shaping responsiveness to environmental perturbations (194).

While pseudo-islets offer clear advantages in experimental control and reduced dependence on donor-specific variability, they also have inherent limitations compared to native islets. The process of pseudo-islet generation involves multiple preparatory steps before a stable and functional structure is reached, introducing opportunities for technical variability. Moreover, pseudo-islets represent a simplified and incomplete version of the native islet microenvironment. They lack key non-endocrine components such as vasculature, innervation, immune cells, and/or stromal elements, all of which play integral roles in nutrient exchange, paracrine signaling, and stress adaptation (195). As discussed in the introduction and illustrated in Fig. 5, the pseudo-islet model could be expanded to include these additional cellular elements, potentially increasing physiological relevance. Nonetheless, even with such enhancements, pseudo-islets remain an artificial and minimalistic system. As with any experimental approach, the chosen model should be guided by the specific research question. In this study, the goal was to dissect the contribution of defined endocrine cell types and hormones to islet growth and fragmentation. Hence, a system of limited complexity and high manipulability was well-suited. However, investigations focusing on integrated islet physiology may be better addressed using native islets, particularly when donor cohorts are carefully stratified.

Taken together, these results suggest that native islets maintain donor-specific signatures that strongly dictate functional and structural responses to hormonal stimuli. Pseudo-islets, however, represent a system in which intra-islet cell composition becomes the predominant determinant. This distinction underscores the need to carefully account for biological context when interpreting outcomes from native vs. engineered islet systems, where donor characteristics dominate in the former and cellular composition in the latter. Such considerations are particularly critical when extrapolating findings to human physiology and disease modeling.

Chapter 4 Glucagon and GLP-1 Accelerate Pseudo-Islet Assembly and Unmask Sex-Specific Islet Fragmentation Dynamics

Kaya Keutler[1], Stella Prady[1], Pamela Canaday[2], Craig Dorrell[3], and Carsten Schultz[1]

[1]Oregon Health & Science University (OHSU), Department of Chemical Physiology and Biochemistry, 3181 SW Sam Jackson Park Road, Portland, Oregon 97239, USA, [2]Oregon Health & Science University (OHSU), Flow Cytometry and Monoclonal Antibody Shared Resource, 3181 SW Sam Jackson Park Road, Portland, Oregon 97239, USA, [3]Oregon Health & Science University (OHSU), Department of Pediatrics, Papé Family Pediatric Research Institute, Stem Cell Center, Pediatric Blood & Cancer Biology Program, 3181 SW Sam Jackson Park Road, Portland, Oregon 97239, USA

4.1 Abstract

Pancreatic hormones are best known for their role in regulating blood sugar levels as well as islet cell function and proliferation. However, their impact on maintaining and inducing cell aggregation in culture remains underexplored. In this study, we investigated the effects of glucagon (GCG) and glucagon-like peptide 1 (GLP-1) on the formation and integrity of human islet clusters. Native human islets were dissociated and sorted into pure α-, β-, and δ-cell populations using antibody-based fluorescence-activated cell sorting (FACS). The sorted cells were then co-cultured with mouse endothelial MS1 cells in suspension to generate pseudo-islets of varying cell composition. Hormonal supplementation with GCG or GLP-1 was administered versus a blank during the tissue culture phase. Hormone-treated pseudo-islets formed faster, dependent on the cellular composition and the sex of the donor. In parallel, we also exposed native islets, maintained in suspension without prior dissociation or sorting, to hormone supplementation. These islets exhibited accelerated fragmentation under hormone treatment compared to controls, again dependent on donor sex, with islets from female donors fragmenting faster

than from male donors. These findings suggest that GCG and GLP-1 enhance pseudo-islet formation and affect the structural integrity of native islets in a sex-specific manner, offering insights into islet biology and implications for diabetes research and therapy.

4.2 Article Highlights

We established a manipulatable, expandable human pseudo-islet platform to investigate islet morphogenesis, architecture, and intercellular signaling. We examined the contribution of individual α-, β-, and δ-cell populations and assessed how glucagon (GCG) and glucagon-like peptide-1 (GLP-1) modulate islet integrity in culture. In native islets, hormonal supplementation attenuated fragmentation in male donors but accelerated it in females. In pseudo-islets, cellular composition was the predominant determinant of maturation versus fragmentation, with donor sex exerting a secondary influence. We present methodological guidelines for generating and maintaining human pseudo-islets, thereby providing a framework to optimize donor selection, culture conditions, and experimental design in diabetes research.

4.3 Introduction

Islets of Langerhans and their secreted hormones are key regulators of glucose homeostasis in mammals. Dysregulation of these cells is the hallmark of diabetes. Therefore, factors that influence the function and well-being of the islet have been the focus for developing new therapeutic strategies beyond insulin supplementation.

Apart from insulin, glucagon-like-peptide 1 (GLP-1) is among the most studied and has led to the approval of diabetes and weight control drugs such as Ozempic. GLP-1 works primarily through the GLP-1 receptor (GLP-1R, a G-protein coupled receptor), which in the islet is exclusively expressed by β-cells (196). GLP-1 has been shown to promote β-cell replication by inducing the expression of cell cycle

regulators such as cyclin D1. This effect is mediated through a signaling network involving cAMP/protein kinase A (PKA), phosphoinositide 3-kinase (PI3K) (197), and mitogen-activated protein kinase (MAPK)/extracellular signal-regulated kinase (ERK). For instance, GLP-1 increases cyclin D1 mRNA and protein levels in β-cells, facilitates the G0/G1-S phase transition, and enhances proliferation (198). In addition to promoting β-cell proliferation, GLP-1 also exerts anti-apoptotic functions by activating survival signaling networks, including the PI3K/AKT pathway, which inhibits the activation of pro-apoptotic proteins like caspase-3 and BAD (197). GLP-1 increases β-cell mass in the islet, partially through the induction of β-cell proliferation as detailed above, but also through inducing the conversion of α-cells into β-cells. This process involves the expression of fibroblast growth factor 21 (FGF21), facilitating the transdifferentiation process (199,200). Additionally, GLP-1 promotes insulin secretion by β-cells as well as suppresses glucagon secretion by α-cells. This is a glucose-dependent action through cAMP and the exchange protein activated by cAMP (EPAC) (201).

These data support the hypothesis that local production of GLP-1 from pancreatic α-cells on demand may be beneficial to protect and regenerate β-cells. This is also suggested by the observation that healthy islets secrete more GLP-1 following culture with high glucose (199), which is a known stressor. Similar results have been previously described in rodents, where α-cells were found to produce more GLP-1 following β-cell injury. This has been thought of as an adaptive mechanism as well as a way to boost insulin secretion from remaining β-cells (202).

In addition to GLP-1, α-cell-secreted glucagon (GCG) modulates β-cell function by regulating microtubule (MT) stability, impacting insulin secretion, and overall islet performance. In islets with a higher α/β-cell ratio, β-cells exhibit a less stable MT network that is associated with enhanced insulin release in response to high glucose and depolarizing stimuli, a response that is recapitulated by direct GCG stimulation (203–205). Mechanistically, GCG and GLP-1 activate cAMP production in β-cells, promoting both the nucleation of new MTs at the Golgi apparatus (thereby supporting insulin secretory granule

biosynthesis) and the destabilization of existing MTs, which increases the pool of releasable insulin granules by potentiating Ca^{2+} influx and elevating granule sensitivity to Ca^{2+}. Furthermore, β-cells in closer proximity to α-cells show more pronounced MT destabilization and insulin secretion, highlighting a spatial aspect of paracrine signaling that underlies the functional heterogeneity of islets (204,205). Further, as indicated by cell line co-culture to form pseudo-islets, α-cell secreted hormones reduce oxidative stress and hence act protectively for β-cell mass (206).

The importance of α-β-cell paracrine regulation is also indicated by the identification of GLP-1R nanodomains on the contact sites of α-cells and β-cells. At those contact sites, pre-internalization of GLP-1R at low glucose levels primes these β-cells for rapid and enhanced Ca^{2+} signaling and insulin secretion upon high-glucose stimulation. β-cells adjacent to α-cells exhibit earlier Ca^{2+} rises and nearly double the insulin release compared to those neighboring other β-cells (207).

GLP-1 and GCG also regulate islet size and architecture. Studies in transgenic mouse models have identified transcription factors such as Elk-1 and Egr-1, downstream of Ca^{2+} signaling, as key controllers of islet development and mass. Dysregulation of these pathways impairs islet architecture and glucose homeostasis. Therefore, both incretin and GCG signaling are critical for islet assembly during development and for preserving islet integrity in adulthood (77,208,209).

Human islet architecture is distinct from that of rodents, although arguments have been made that within human islets, microdomains follow the rodent islet organization of β-cells in the core and α-cells in the mantle (45,210,211). However, little is known about the placement of δ-cells and the connection/placement of blood vessels. Although islets only represent 1–2 % of the pancreatic mass, they receive 6–20% of the direct arterial blood flow to the pancreas (212). Based on measurements in the perfused rodent pancreas, Samols *et al.* observed a β → α → δ sequence, implying that δ-cells occupy the final (most downstream) positions along the islet capillary network, *i.e.,* immediately adjacent to the draining vessels (213). Using immunohistochemistry, Braun *et al.* indicated that within isolated human

islets (that hence lack vascularization), δ-cells reside close to cell-free areas (possibly corresponding to openings from blood vessels) (43). It has been suggested that the islet is extremely vascularized, with each β-cell connected to a blood vessel or at least no more than one cell apart from a blood vessel (46), which ensures that insulin is directly released into the bloodstream (46,47,214).

Over the last two to three decades, researchers have made substantial progress in characterizing the islet microenvironment and its signaling networks. However, these insights remain circumstantial because no model allows real-time study of islet organoid formation with manipulatable components. Without such a system, it is impossible to explain why native islets diverge in behavior from immortalized cell lines or to pinpoint which cell types or hormones drive those differences. Therefore, we have developed a pseudo-islet platform built from primary human cells that enables controlled assembly and manipulation of specific endocrine cell populations, providing a tool to dissect cell-type– and hormone-specific effects on islet development and function.

In this study, we demonstrate that immortalized pancreatic cell lines exhibit enhanced growth when the culture media was supplemented with glucagon or GLP-1. This effect was found to be mediated via their respective G protein–coupled receptors. However, when native human islets were exposed to the same hormones, they did not show improved viability. Instead, their previously observed (179,215,216) in culture fragmentation was accelerated in female but not male donor islets. To dissect these divergent responses, we established a controllable pseudo-islet model derived from human donor islets. These engineered pseudo-islets regain the growth benefit observed in cell lines upon hormone supplementation, revealing that the extent of this benefit depends on cellular composition, without sex-specific differences.

4.4 Methods

4.4.1 Tissue culture of pancreatic cell lines.

Mouse Insulinoma 6 (MIN6) cells were a kind gift from Dr. Miyazakis's lab (Osaka, Japan). MIN6 cells were cultured in DMEM with 4.5 g/L glucose (Gibco, REF# 11965-092) supplemented with 70 μM β-mercaptoethanol (Gibco, REF# 21985-023) before use. Cells were passaged once per week and used within passages 17-30.

αTC1 clone 9 cells were a kind gift from the lab of Dr. Grompe (Portland, OR, USA). αTC1 cells were cultured in DMEM with 1 g/L glucose (Gibco, REF# 11885084) that was supplemented with 15 mM HEPES (Cytivia, REF #AJ30727929), NEAA (Gibco, REF #11140-050), and 100 mg BSA (Sigma, REF# A7906). Cells were passaged every three days and used within passages 4-13.

4.4.2 Monitoring cell growth in response to media supplementation.

Pancreatic hormone-secreting cell lines (MIN6 (passages 17-30), and aTC1 cl. 9 (passages 4-13)) were used to monitor cell growth. Cells were kept in high-glucose DMEM (4.5 g/L glucose, Gibco, REF# 11965-092) and low-glucose DMEM (1 g/L glucose, Gibco, REF# 11885084), respectively. For supplementation, hormones were purchased from Sigma Aldrich and used at the concentrations described in Table 13.

To generate a growth curve, cells were seeded in 12-well plates (Falcon, LOT #353043) at a density of 0.1 x 10^6 cells/mL. Cell growth was determined by manually counting the cells in each well (triplicate per day) on T2-T6 post-seeding with a hemocytometer. Cells were diluted with trypan blue (Sigma, REF #T8154). Additionally, cell counts were determined semi-automated using a Keyence EPI-microscope and FIJI software to analyze the generated images. For this imaging, on the respective days, cells were stained with 10 μg/mL Hoechst (REF#TG2611041) for 10 min, at 5 % CO2 and 37 °C. After

washing, whole wells were imaged and analyzed using FIJI following the pipeline described in Supplemental Fig. 5.

Manually and semi-automatically, cell-count results were correlated by calculating the number of cells per area. For manually counted cells, the area corresponded to the number of cells counted for each square of the hemocytometer (1 mm^2). Cells in an entire well (380 mm^2) were counted semi-automatically. Manually counted cell numbers were compared to semi-automatically counted cells by multiplying by the dilution factor and then the area of the whole well.

Table 13: Overview of compounds and hormones used

Media Supplementation	Final Concentration
GLP-1 (human)	0.1 μg/mL
Glucagon (GCG, human, G3265)	0.1 μg/mL
Somatostatin (SST)	100 nM
Exendin 9-39 (GLP-1R antagonist, E7269)	0.1 μg/mL
GLP-1R agonist (G8038)	0.1 μg/mL
GCGRIIα	1 μM

4.4.3 Handling of human pancreatic islets.

Human pancreatic islets were provided by the NIDDK-funded Integrated Islet Distribution Program (IIDP) (RRID:SCR _014387) at City of Hope, NIH Grant # U24DK098085, and the JDRF-funded IIDP Islet Award Initiative (Study # BS562P & BS562). Additionally, human islets for research were provided by the Alberta Diabetes Institute IsletCore at the University of Alberta in Edmonton (http://www.bcell.org/adi-isletcore.html) with the assistance of the Human Organ Procurement and Exchange (HOPE) program, Trillium Gift of Life Network (TGLN), and other Canadian organ procurement organizations. Islet isolation was approved by the Human Research Ethics Board at the University of Alberta (Pro00013094) (179). All donors' families gave informed consent for the use of pancreatic tissue

in research. Islets from both distribution programs were shipped overnight and processed on the receiving day. If that was not possible, they were stored at 4 °C for no more than seven days. Native islets, when used as controls for pseudo-islets, were maintained in 1x CMRL 1066 media (Corning, REF# MT15110CV) supplemented with 10 % FBS, 10 mM HEPES (Cytivia, REF#AJ30727929), and 2 % L-glutamine (Gibco, REF#25030-081) with 1 % Pen/Strep (Gibco, REF# 15140122) and 1 μg/mL Amphoticerin B (Sigma, A2942, CAS # 1397-89-3) added just before use in culture. Human donor characteristics are listed in Appendix Table S1.

4.4.4 Tissue sources and pancreatic cell isolation.

Human pancreatic islets from normal donors were obtained from the NIDDK-funded Integrated Islet Distribution Program (IIDP) at City of Hope (Study # BS562P & BS562). These were collected from approved, consented cadaveric organ donors from whom at least one other organ has been approved for transplantation and are exempt from human studies approval. Specimens were dispersed to single-cell suspensions by an 8–15 min digestion in 0.05% trypsin-EDTA (Gibco, REF#25-300-054) at 37 °C with dispersal by a p1000 micropipette every 3 min. The progress of the dispersion was checked by light microscopy. Undispersed tissue was removed with a 40-μm cell strainer (Fisherbrand, REF#22-363-547), and dissociated cells were stored on ice in holding buffer (CMRL1066 + 2% FBS + 0.1 mg/mL trypsin inhibitor (Sigma, REF#T9128) and 0.1 mg/mL DNAse I (Roche, REF#10104159001) before antibody labelling for FACS. The number of samples analyzed was primarily determined by material availability, but it was chosen to be sufficient for statistical analysis.

4.4.5 FACS of dissociated human islets into pure α-, β-, and δ-cell populations.

Dissociated cells were resuspended in holding buffer (CMRL1066 + 2% FBS + 0.1 mg/mL trypsin inhibitor (Sigma, REF#T9128) and 0.1 mg/mL DNAse I (Roche, REF#10104159001)) before the addition of antibodies. The antibodies used were: HIC1-2B4 A488 conjugated (Novus Biologicals, REF# NBP1-

18946AF488) at a 1:100 dilution, HIC1-8G12 PE conjugated (provided by the Grompe lab) at 1:50 dilution, and anti-CD9 APC conjugated to APC (Thermo Fisher Invitrogen, MA1-10307) at a 1:20 dilution. Single antibody controls, FMO-APC, and all combined samples were incubated at 4°C for at least 20 min. After washing with cold CMRL1066, cells were resuspended in holding buffer, and 1 % propidium iodine (Sigma, REF#P4864) was added for live/dead distinction. Cell doublets were excluded by pulse width measurement, and propidium iodide staining was used to label dead cells for exclusion. Analysis was performed on a Cytopeia inFluxV-GS (Becton-Dickinson, BD) or a BD Symphony S6.

4.4.6 Generation of pseudo-islets.

Freshly sorted pancreatic cells were used to generate pseudo-islets. Pure cell populations were spun down directly after sorting and resuspended in 300 μL of media (CMRL1066 + 2% FBS + 1 % Pen/strep, + 1 μg/mL Amphoticerin B). Based on the obtained cell numbers, concentrations in cells/μL were calculated and used to mix cells in specific ratios. If not indicated otherwise, cells were combined in a 5:1 ratio for β:α, 16:1 for β:δ, and 3:1 for α:δ. Additionally, pseudo-islet mixtures were combined with MS1 cells in a 1:10 ratio, with ten MS1 cells (kindly provided by the Grompe Lab, CRL-2279) for every one endocrine cell (unless otherwise specified). Cell mixtures were seeded in ultra-low attachment, flat-bottom 6-well plates (Corning, REF# CLS3471) in 3 mL of media (CMRL1066 + 2% FBS + 1 % Pen/strep, + 1 μg/mL Amphoticerin B). Cluster formation was allowed to happen for up to 14 days with hormone (0.1 μg/mL GCG or GLP-1) addition and culture media refill (100 μL/well to account for evaporation) every other day. Cluster formation was monitored by using a Keyence EPI-microscope in brightfield mode and FIJI software (see Appendix Fig. 4) to analyze the generated images.

4.4.7 Supplementation of pancreatic cell lines, native islets, and pseudo-islets.

For media supplementation, compounds listed in Table 1 were used in the concentrations described in column “Final Concentration”. Compounds were added every other day for the duration of the

experiment. In case of native and pseudo-islets, 100 μL of media were refilled every other day to account for evaporation and to replenish nutrients, Pen/strep, and Amphotericin B to prevent contamination.

4.4.8 GSIS analysis.

Samples (pseudo-islet mixtures and native donor islets) were removed from media and equilibrated by incubation for 1 h at 37°C, 5 % CO2 in KRHB + 2.8 mM glucose (pre-incubation). Cells were then transferred to fresh buffer (KRHB + 2.8 mM (basal) or 22.2 mM (stimulated)) glucose for 1 h at 37 °C, 5 % CO2. After incubation, buffers were collected and stored at 4 °C for subsequent ELISA analysis (Promega, Lumit, Insulin Kit REF#CS3037A05 and Glucagon Kit REF#W8020). Additionally, total human insulin and glucagon content was measured from an aliquot of RIPA-lysed (RIPA, ThermoFisher REF # 89900 + Protease Inhibitors, cOmplete™ Protease Inhibitor Cocktail tablets, Sigma, REF # 11697498001) clusters by human insulin/glucagon ELISA (Promega, Lumit). Statistical analyses of the results were performed using Graphpad Prism 10.5 (for analysis of variance tests) and Microsoft Excel (for mean and standard deviation).

4.4.9 Immunofluorescent labeling of native and pseudo-islets.

Native and pseudo-islets destined for immunohistochemistry were either fixed and stored or processed immediately for antibody staining. For storage, islets were fixed in 4 % paraformaldehyde (PFA) at RT for 15 min, then quenched with 30 mM glycine for 1 min. After centrifugation at 300 × g for 4 min, RT to pellet the islets, the SN was discarded, and the pellet was resuspended in 20 % (w/v) PEG 400 in PBS (storage solution) to fully cover the islets. These preparations were then stored at – 20 °C until use.

For direct staining, islets were fixed in 4 % PFA at RT for 1 h, pelleted at 300 × g for 4 min, and blocked in PBS containing 10 % FBS and 0.1 % Triton X-100 for 1 h. Following another 300 × g spin to remove

blocking solution, islets were incubated without agitation in primary antibody mix—anti-insulin (ThermoFisher, REF#, 1:500), anti-GCGR (Abcam, REF#ab75240,1:250), and anti-GLP-1R (Iowa DSHB, REF#Mab 7F38,1:30)—in blocking buffer for 3–4 d at 4 °C. After a brief wash spin (300 × g, 4 min, RT), islets were incubated in secondary antibodies (Cy3-conjugated donkey anti-guinea pig (Jackson ImmunoResearch, REF#706-165-148), Alexa 488 goat anti-rabbit (Invitrogen, REF#A11034), and Alexa 647 goat anti-mouse (Invitrogen, REF#A21235), each at 1:1,000 in blocking buffer) at RT for 3 h or at 4 °C for up to 24 h. Finally, islets were spun once more, resuspended in ~ 20 µL blocking buffer, and mounted on slides beneath a drop of DAPI-containing mounting medium (ThermoFisher, REF#P36966). Coverslips were applied and, once dry, slides were imaged on an Olympus F1200 confocal microscope using 405 nm, 488 nm, 559 nm, and 635 nm laser line excitation. Islets that were stored at – 20 °C were processed the same way for antibody staining, except for including additional washing steps beforehand to completely remove the storage solution.

4.4.10 Software.

For image processing, both FIJI (Appendix Fig. 4) and CellProfiler (Appendix Fig. 5) were used. To further streamline image analysis, FIJI macros were written for cell growth monitoring, native islet cluster counts, and pseudo-islet cluster counts. These scripts were deposited on GitHub and can be found under https://doi.org/10.5281/zenodo.16757638. CellProfiler pipelines were generated for each channel combination and are also available on GitHub (https://doi.org/10.5281/zenodo.16757674). For basic calculations, such as mean and standard deviation, Microsoft Excel was used. For complex statistical evaluation, GraphPad Prism 10.5 was used.

4.4.11 Statistical Analysis and Reproducibility.

Donors were stratified by sex (female vs. male) to account for sex-specific differences; no other donor characteristics (*e.g.,* BMI, age, A1C) were used for grouping. For native islets, each condition was

assayed in two technical replicates unless otherwise noted. Pseudo-islet experiments followed the same scheme with two technical replicates per condition whenever sort yields permitted. In total, experimental results from 10 female and 14 male donors served as biological replicates. All statistical comparisons were made by two-way ANOVA with Benjamini–Hochberg correction for multiple testing.

4.5 Results

4.5.1 GCG and GLP-1 promote the growth of pancreatic cell lines

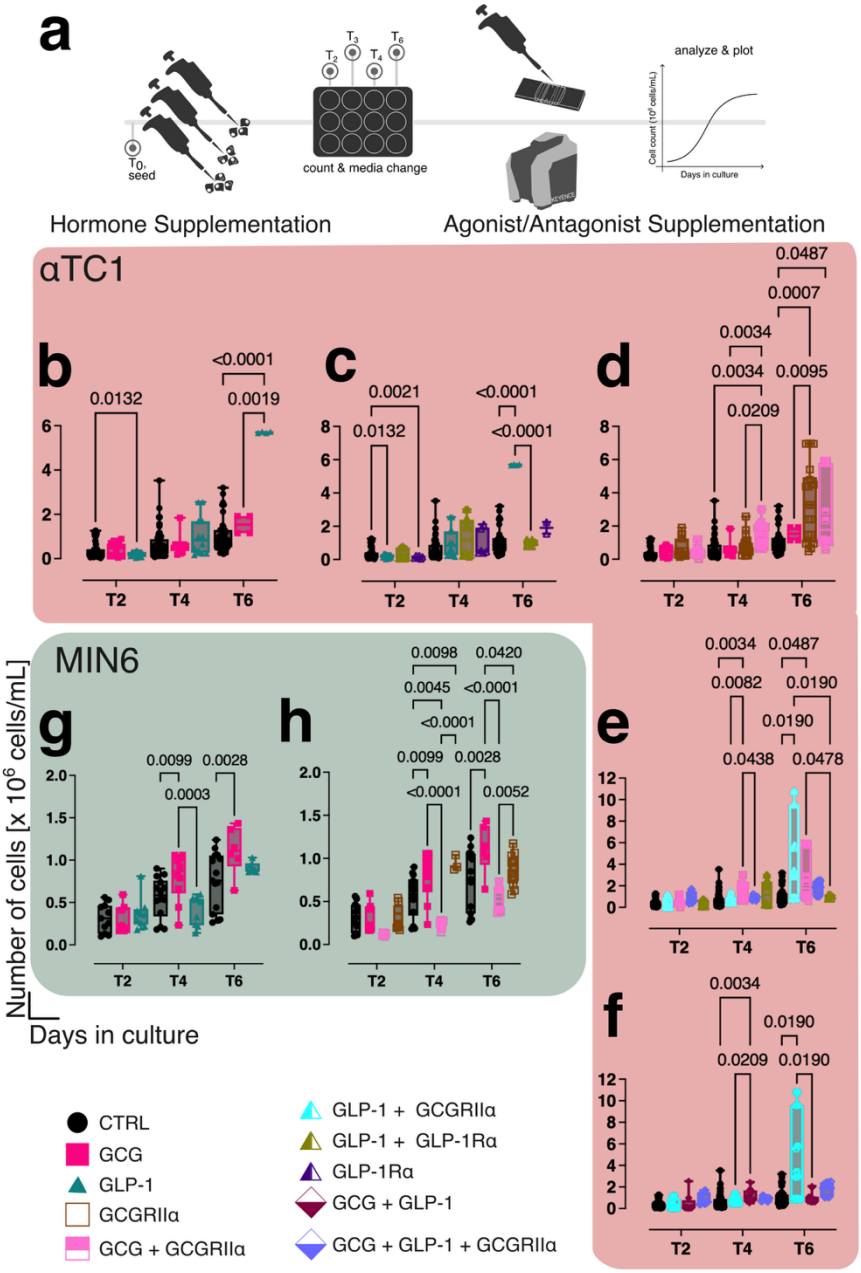

Figure 17: Hormone supplementation influences the Growth of pancreatic cell lines. (**a**) Pancreatic cell lines, MIN6 representing β-cells and αTC1 representing α-cells, were seeded in 12-well plates and supplemented with single pancreatic hormones or combinations thereof. Growth monitoring was carried out for up to 6 days post-seeding with media exchange, hormone addition, and cell counts every day starting from T2 post-seeding (T3 and T5 counts are not shown for a better overview). (**b-f**) αTC1 cells (red panel) supplemented with 0.1 μg/mL of hormones (GCG (pink) or GLP-1(teal)), 0.1 μg/mL of GLP-1Ragx (GLP-1R antagonist, purple triangle), 1 μM GCGRIIα (GCGR antagonist, brown) or combinations thereof (see legend for color associations). **g & h**) MIN6 cells (green panel) supplemented with 0.1 μg/mL of hormones (GCG (pink) or GLP-1(teal)), 1 μM GCGRIIα (GCGR antagonist, brown) or combinations thereof (see legend for color associations). Black represents CTRL conditions, which is the respective cell type in regular media without any additional supplementations. Statistical analysis was done by two-way ANOVA or mixed model (data dependent) for matched values in subcolumns. The Benjamini-Hochberg correction was used to adjust for multiple comparisons. P-values < 0.05 (considered the cutoff for statistical significance) are listed on the graphs.

MIN6 (β-cell) and αTC1 clone 9 (α-cell) lines were maintained in medium supplemented with 0.1 μg/mL GCG and/or GLP-1. Both peptides significantly increased cell growth compared with controls, as assessed by increases in Trypan Blue exclusion and Hoechst-stained cell counts. For quantification, cells at each condition (CTRL, + GCG, + GLP-1) were seeded into a 12-well cell culture plate, and cell numbers were assessed on days 2, 4, and 6 post-seeding (see Fig. 17a). The observed increase in cellular growth was consistent with current literature as summarized by Zheng *et al.* (217). However, the magnitude of the response depended on the cell type: GCG elicited the greatest proliferation in MIN6 cells, whereas GLP-1 drove the strongest increase in αTC1 clone 9 cells. To dissect receptor-mediated mechanisms, we treated cells with selective agonists and antagonists for the GCGR and GLP-1R receptors. Antagonism of GCGR with the small molecule GCGRIIα (a selective, non-competitive, high-affinity GCGR antagonist) abolished the proliferative effect observed with GCG, without deviating from control conditions when given alone. Further, inhibition of GLP-1R by Exendin 9-39 blocked GLP–1–induced α-cell growth, whereas Exendin 9-39 alone had no impact on basal proliferation of αTC1 clone 9 cells (Fig.17).

4.5.2 Media supplementation with GCG and GLP-1 alters the fragmentation of native human islets in culture in a donor-sex-dependent manner

We next repeated the cell culture experiments using native human islets. Islet cells did not proliferate without or in response to 0.1 μg/mL GCG or GLP-1, consistent with the reported minimal replicative capacity of adult β-cells *ex vivo* (218). However, isolated primary islets are known to fragment over time

in standard culture (as exemplary indicated in Fig. 18a), with a rapid shift toward smaller islet particles occurring within the first 24 h (47,179,215). Fragmentation proceeded even faster when we maintained islets in culture for up to 10 d with cluster counts at 2-3, 6-7, and 9-10 d post-seeding (Fig. 18b (female) and c (male)). When we supplemented native human islets with GCG or GLP-1, this fragmentation was significantly accelerated compared with untreated controls. This was reflected by an increase in 30 μm diameter cluster counts from 2 to 10 d post-seeding, with percent increases of 87.1 % in females and 130.9 % in males under control conditions, 68.2 % in females and 85.8 % in males with GCG, and 137.2 % in females and 99.8 % in males with GLP-1 (Fig. 18d (male) and Fig. 18g (female)). Additionally, changes in the proportion of subclusters (< 30 μm diameter; Fig. 18e (male) and Fig. 18h (female)), expressed as a percentage of control, further supported ongoing fragmentation. In males, subcluster abundance in the + GCG condition was elevated at 2 d (114.2 %) but declined by 6 and 10 d (77.5 % and 86.3 %, respectively). A similar pattern was observed with + GLP-1 (117.8 %, 91.2 %, and 83.6 %). In contrast, female islets showed consistently elevated sub-cluster proportions. With + GCG, values

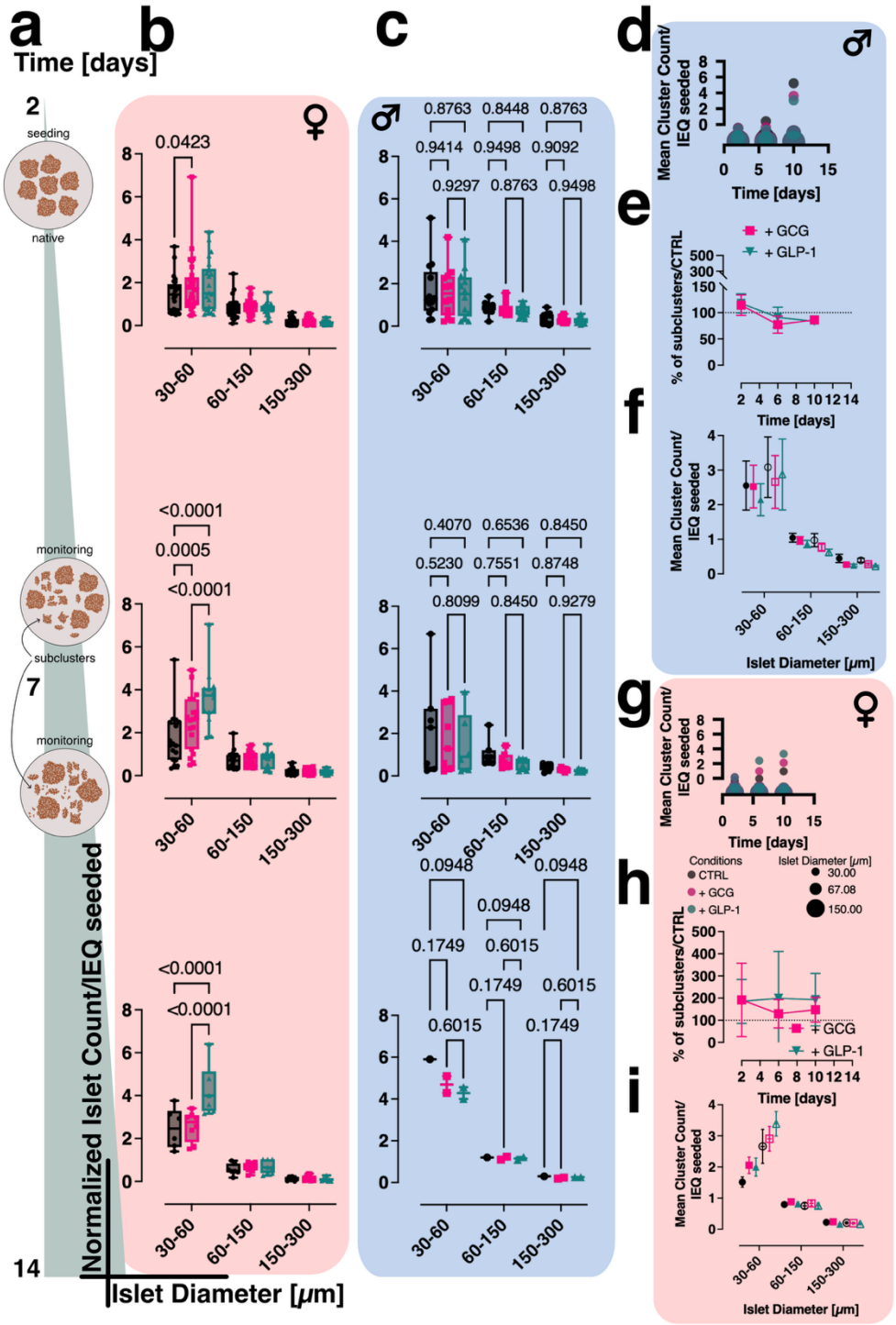

were 192 % at 2 d, 129 % at 6 d, and 147.6 % at 10 d. With + GLP-1, subclusters remained high across all time points (184.7 %, 199.4 %, and 193 %). Both cluster and subcluster counts were assessed by the analysis of EPI microscopy-captured images with a FIJI pipeline described in Appendix Fig. 4. Therefore, hormone-treated islets exhibited an exaggerated loss of structural integrity during long-term culture when treated with α-cell-derived hormones.

Figure 18: Response to hormone supplementation of native islets is influenced by donor sex. Growth and formation of native islets were monitored by light microscopy, monitoring islet diameter [μm] for up to 10 days post-seeding. (**a**) Experimental timeline and modeling of expected behavior in culture. (**b**) Top row: 2-3 days post-seeding, middle: 6-7 days, and bottom: 9-10 days. Data pooled by donor gender (n = 35 replicates for female donors (**b**) and n = 16 replicates for male donors (**c**)). Hormone supplementation with 0.1 μg/mL of either GCG (pink) or GLP-1 (teal) compared to CTRL condition in black. (**d**) and **g**) mean cluster counts for cluster sizes of 30 μm – 150 μm normalized to the number of islet equivalents (IEQ) seeded, over time in culture for male (**d**) and female (**g**) donors. Spheres are colored by condition (black = CTRL, pink = + GCG, and teal = + GLP-1), and the size corresponds to the size in islet diameter (μm). e) and h) Subclusters, defined as clusters < 30 μm, expressed as % of control condition and plotted over time in culture for + GCG (pink) and + GLP-1 (teal) for male (**e**) and female (**h**) donors. (**f**) and (**i**) mean cluster count/IEQ seeded for islet diameter ranging from 30 – 150 μm. Filled symbols for CTRL (black), + GCG (pink), and + GLP-1 (teal) correspond to clusters counted 2-3 days post-seeding. Clear symbols for CTRL (black border), + GCG (pink border), and + GLP-1 (teal border) correspond to clusters counted 6-7 days post-seeding. Statistical analysis was done by two-way ANOVA with a Benjamini-Hochberg correction for multiple comparisons. All p-values are indicated on graphs, space-permitting; otherwise, only significant p-values are shown; $p < 0.05$ was selected as being statistically significant.

The effect of hormone supplementation on islet fragmentation was donor sex–dependent. In female islets, supplementation with GCG and GLP-1 led to increases in 30 μm diameter cluster counts to 78.3 % and 157.5 % of control values, respectively (Fig. 18g and i). In contrast, male islets showed more modest responses, with values reaching 65.6 % (+ GCG) and 76.2 % (+ GLP-1) of control (Fig. 18d and f). A similar trend was observed in the proportion of subclusters, where female islets exhibited elevated fragmentation under both treatments (μ = 158.3% with GCG and μ = 186.5% with GLP-1, relative to control; Fig. 18h). In comparison, male islets fragmented over time but remained at or below control levels, with subcluster proportions of μ = 88.8 % (+ GCG) and μ = 92.3 % (+ GLP-1) (Fig. 18e). All other donor-to-donor differences, such as age, ethnicity, BMI, and A1C, were ignored, and donors were only pooled based on their sex. Islets from male donors maintained a fragmentation profile like untreated control islets or showed improvement despite the presence of GCG or GLP-1, whereas female islets exhibited markedly increased fragmentation in response to both treatments. Therefore, our data indicate that GCG and GLP-1 promote structural destabilization of human islet clusters in a sex-dependent manner.

4.5.3 Primary human islet cells form pseudo-islets and respond to pancreatic hormone supplementation

Native human islets did not exhibit growth or any other beneficial effect in response to GCG or GLP-1. However, they represent fully differentiated tissue and do not mimic the dynamic process of islet formation. In contrast, cell lines that form clusters during proliferation are considered non-physiological. To address this limitation, we developed a pseudo-islet model that recapitulates the early assembly of islets from primary human α-, β-, and δ-cells. This model not only enables the study of cell-cell interactions and hormone effects during islet reconstitution but also provides a standardized, human cell–based platform for functional studies.

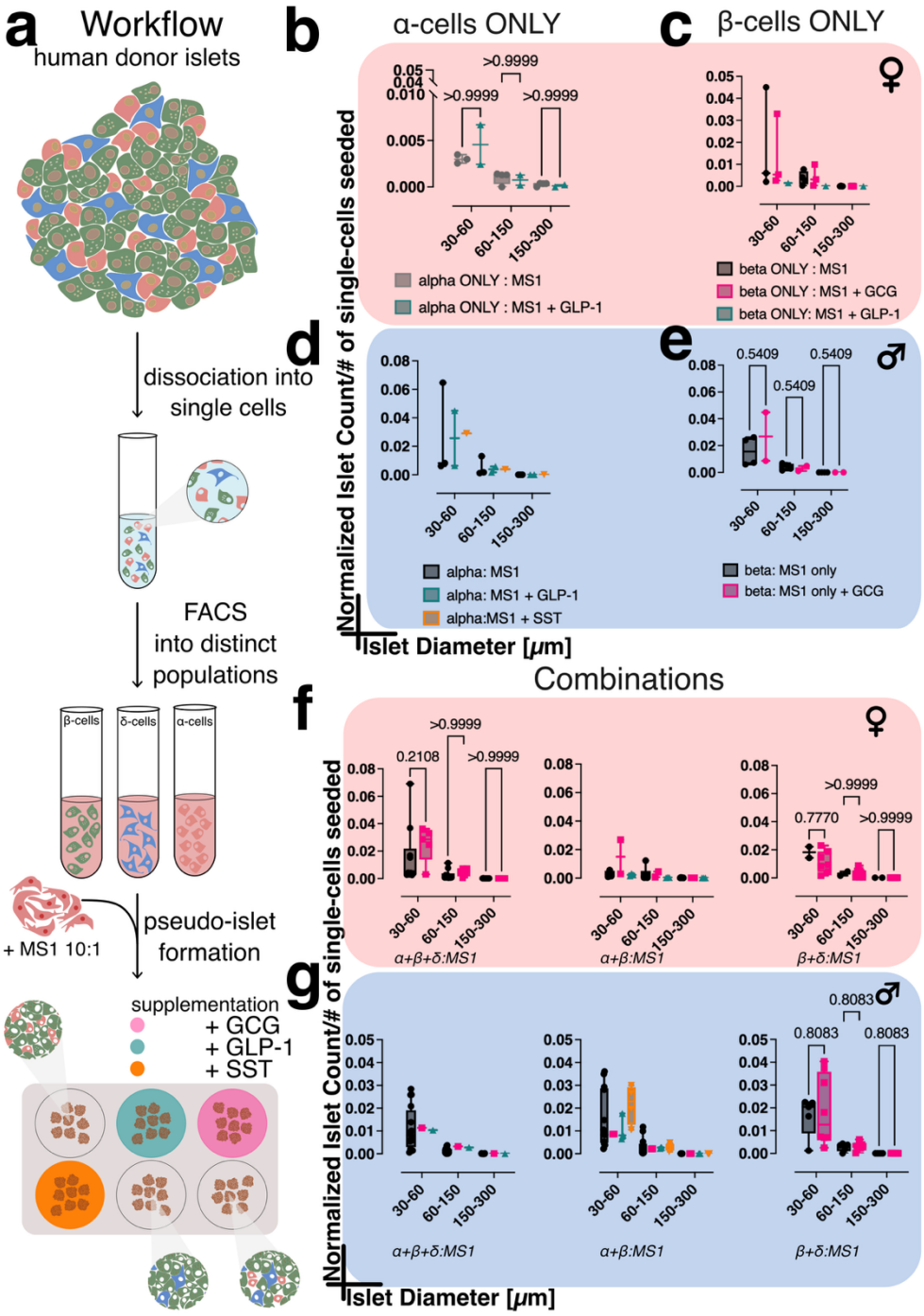

We generated pseudo-islets after dissociating native human islets into single cells and sorting them into pure α-, β-, and δ-cell fractions by fluorescence-activated cell sorting (FACS) using a pre-established procedure from the Grompe lab (170) (Fig. 19a, Appendix Fig. 2).

To support three-dimensional re-aggregation, we mixed defined combinations of endocrine cells with MS1 pancreatic endothelial cells at a 1:10 endocrine:non-endocrine ratio, a method known to promote free-floating pseudo-islets with enhanced structure and function in

Figure 19: Human-donor-derived α-cells, β-cells, and combinations thereof form cell clusters (pseudo-islets) that are responsive to pancreatic hormone supplementation. (**a**) Workflow: Human donor islets derived from male and female donors were dissociated into single cells, stained with HIC1-2B4 AF488 (pan-endocrine marker), HIC1-8G12 PE (non-β-endocrine cell marker), and CD9 APC (predominantly δ-cell marker), and sorted into distinct α-, β-, and δ-cell populations via FACS. These populations were used to form pseudo-islets from single populations (**b**) and (**d**) for α-cells ONLY and (**c**) and (**e**) for β-cells ONLY) or combinations thereof (**f** and **g**). Pseudo-islets were formed in ultra-low attachment 6-well plates and combined in a 1:10 ratio of endocrine to Mile Sven 1 (MS1) cells (mouse pancreatic endothelial cells). Hormone supplementation: 0.1 μg/mL GCG (pink), 0.1 μg/mL GLP-1 (teal), and 100 nM somatostatin (SST, orange), compared to the control (CTRL, black), with supplements administered every other day. Growth and formation of pseudo-islets depicted in all subpanels are from 2-3 days post-seeding via EPI-light microscopy. Donors pooled by sex; panels (**b**), (**c**), and (**f**) correspond to female donors and panels (**d**), (**e**), and (**g**) to male donors. Statistical analysis was done by two-way ANOVA with a Benjamini-Hochberg correction for multiple comparisons. P-values are indicated for each comparison; $p < 0.05$ was considered the cutoff for statistical significance.

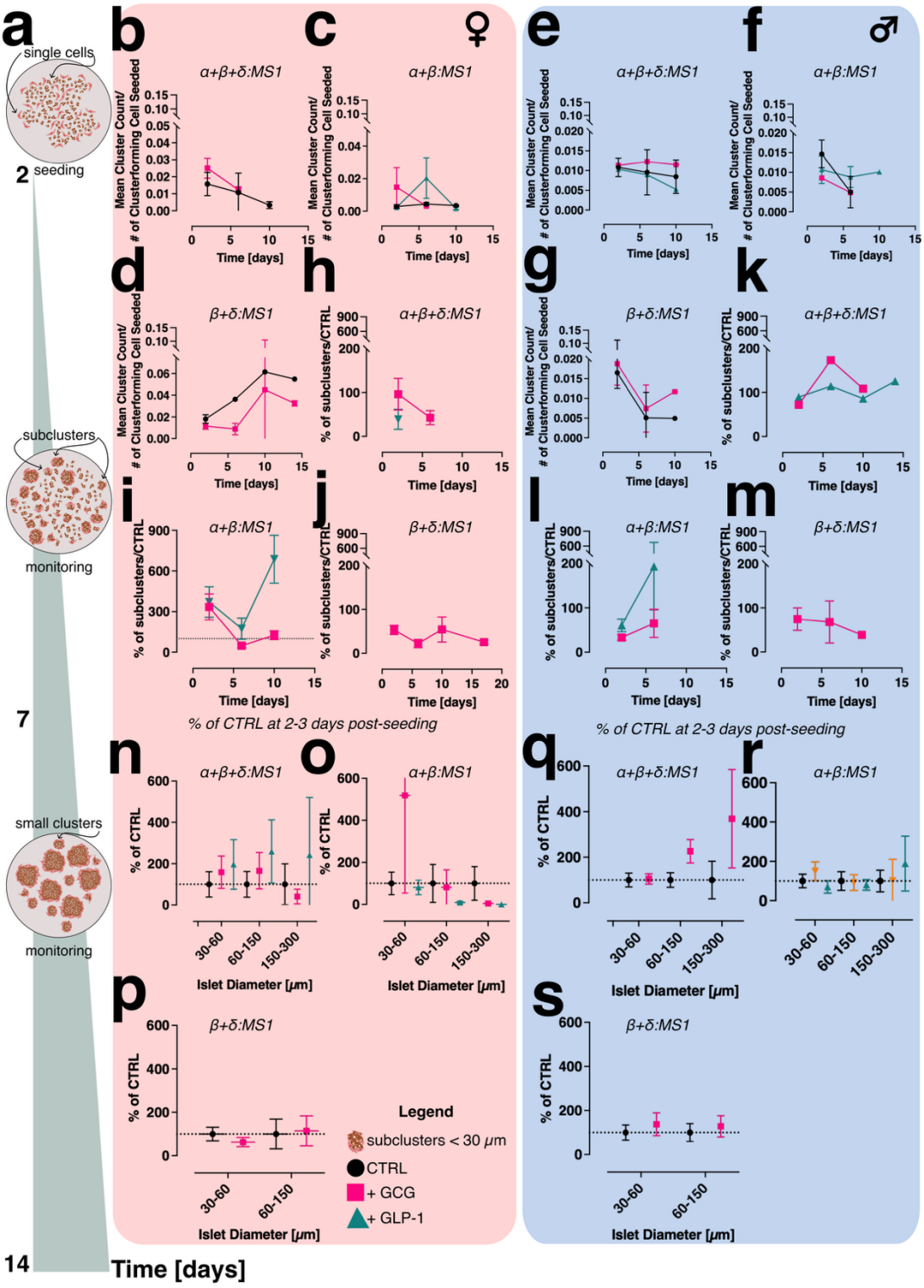

Figure 20: Pseudo-Islet formation is influenced by cell composition, hormone supplementation and donor sex. (**a**) Modeling of the changes occurring to pseudo-islets as they mature in culture over time. (**b**), (**c**), and (**d**) female "dynamic growth" curves. (**e**), (**f**), (**g**) Male "dynamic growth" curves. Both expressed as mean cluster count/seeded cluster-forming cell number. (**h-j**) (Female) and (**k-m**) (male)) % of subclusters normalized to control for pseudo-islet mixtures as depicted. (**n-p**) (Female) and (**q-s**) (male)) pseudo-islet growth at 2-3 days post-seeding expressed as % CTRL. Statistical analysis was done by two-way ANOVA with a Benjamini-Hochberg correction for multiple comparisons. P-values are indicated for each comparison; $p < 0.05$ was considered the cutoff for statistical significance. Error bars represent the SEM.

ultra-low attachment plates (219) (Fig. 19a). We anticipated that pseudo-islets would form over time from clustering of single cells, beginning as small subclusters (< 30 μm) and growing into larger clusters within defined size bins (30–60, 60–150, or 150–300 μm) (Fig. 20a). However, pseudo-islet behavior in culture was less intuitive to interpret compared to native islets due to differences in normalization. Native islet cluster counts were normalized to IEQs seeded per well, with values <1 indicating loss or fusion, >1 indicating fragmentation, and interpretation further refined by subcluster percentage. In contrast, pseudo-islet cluster counts were normalized to the number of

single cells seeded. Here, changes in cluster counts and subcluster percentages reflected fragmentation, fusion, or maturation. A summary of interpretative scenarios is provided in Chapter 3, Table 6.

Pseudo-islets were found to form robust, compact spheroids as observed by brightfield microscopy (examples included in Chapter 3, Section 3.3.2, Fig. 13). Those containing β-cells displayed the most islet-like morphology, characterized by a spheroid structure with well-rounded edges and an amber hue under brightfield microscopy. However, pseudo-islets also formed from pure β- or α-cells (Fig. 19b–e) or their combinations (Fig. 19f–g). Supplementation with GCG or GLP-1 altered pseudo-islet formation and growth compared to unsupplemented controls. These effects depended on cellular composition, donor sex, and the type of supplementation. In female-derived β+δ pseudo-islets, cluster size shifted progressively toward smaller aggregates under both conditions, with complete loss of 150–300 μm clusters by day 10 (+ GCG) or day 14 (control) (see Chapter 3, Fig. 15). Subcluster percentages remained below 100 % under + GCG (Fig. 20j), suggesting maintenance of intermediate-sized clusters. In contrast, male-derived β+δ pseudo-islets retained larger clusters (60–150 and 150–300 μm) over time, with minimal fragmentation; subcluster percentages remained lower under + GCG than control (Fig. 20m). To complement size bin analyses, dynamic growth curves (30–300 μm) were used. In female pseudo-islets, + GCG suppressed growth by up to 120 % compared to control (Fig. 20d). In males, both conditions showed an early decline, but + GCG later promoted recovery (62.2 % by day 10; Fig. 20g). Full interpretations for other combinations are summarized in Chapter 3 Table 6.

Like native islets, pseudo-islets show sex-specific differences, although more nuanced. Our results indicate that both female- and male-derived pseudo-islets respond to GCG and GLP-1 supplementation during early stages of pseudo-islet formation, with evidence of increased aggregation or maturation depending on the condition. However, over longer culture periods (9–10 d), signs of fragmentation

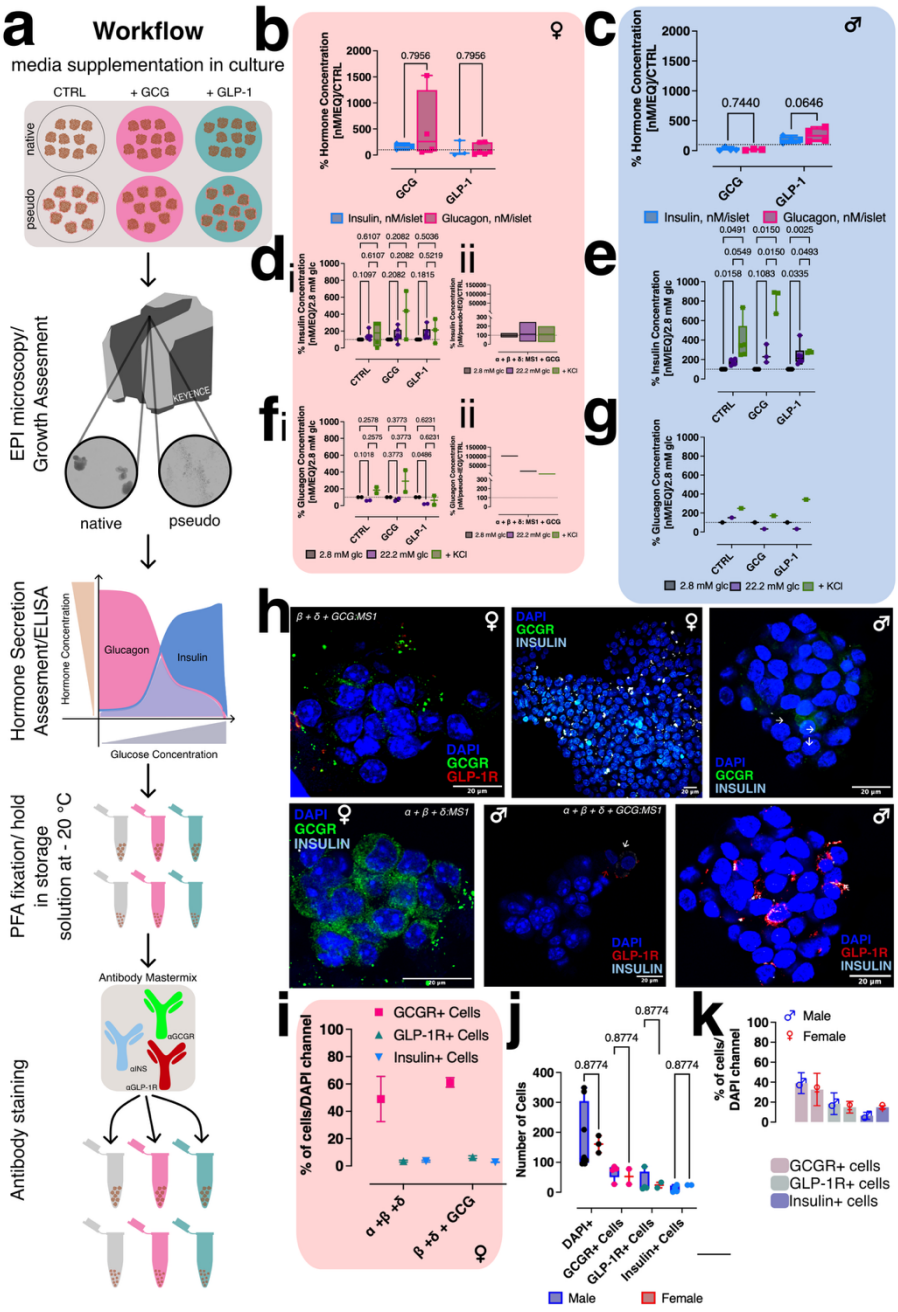

emerge, particularly in female-derived pseudo-islets treated with GLP-1 (Fig. 20i). Increased subcluster percentages and a decline in cluster counts indicate this. In male-derived pseudo-islets, fragmentation tends to occur earlier, often by 6–7 d, and is especially pronounced in the + GLP-1 condition (Fig. 20e and f). These findings suggest that the structural trajectory of pseudo-islets is cell composition-dependent, sex-dependent, and hormone-specific, with early hormone-induced stabilization in some combinations giving way to later-stage fragmentation.

Figure 21: Sex-specific functional responses and receptor expression in native and pseudo-islets. (**a**) Workflow schematic: functional characterization of native and pseudo-islets for hormone secretion and receptor expression. (**b** and **c**) total hormone content for glucagon (pink) and insulin (blue) for native islets from female and male donors, respectively. (**d_i** and **e**) mean insulin concentration assayed from native islet supernatant (SN) in response to 2.8 mM (black), 22.2 mM glucose (purple), and 30 mM KCl (green) for female and male donor islets. (**fi** and **g**) mean glucagon concentration assayed from native islet SN in response to 2.8 mM (black), 22.2 mM glucose (purple), and 30 mM KCl (green) for female and male donor islets. (**d_{ii}** and **f_{ii}**) mean insulin and glucagon concentration, measured from SN of pseudo-islets formed from α+β+δ-cells (+/- GCG) at 2.8 mM glucose (black), 22.2 mM glucose (purple), and 30 mM KCl (green) for female donors only. For all ELISA results, values are normalized/IEQ used in the experiment and expressed as % of response to 2.8 mM glucose or CTRL. (**h**) Representative immunofluorescent images for native and pseudo-islets from female and male donors stained with DAPI (blue), GCGR (neon green), GLP-1R (dark red), and insulin (white). (**i**) Percentage of GCGR+, GLP-1R+, and insulin+ cells normalized to DAPI+ (=total cells) for pseudo-islets derived from female donors. (**j**) cell count comparison between native islets from female (red) and male (blue) donors. (**k**) cell counts from (**j**) expressed as % of DAPI+ cells for female (red) and male (blue) donors. Statistical analysis by two-way ANOVA with a Benjamini-Hochberg correction for multiple comparisons. P-values are indicated for each comparison; $p < 0.05$ was considered the cutoff for statistical significance. Error bars represent the SEM.

4.5.4 Sex-specific analysis of islet hormone secretion and receptor expression in native and pseudo-islets

Cultured native and pseudo-islets were assessed following the workflow outlined in Fig. 21a. For native islets, fragmentation was monitored, while for pseudo-islets, formation was observed. Brightfield images were acquired every 2–3 days using EPI light microscopy. After 7 days, intact native islets and formed pseudo-islets were manually harvested for functional assays of hormone secretion. Insulin and glucagon secretion were quantified using the Promega Lumit detection kits (Appendix Fig. 3). After functional assessment, remaining islets were fixed in PFA and processed for immunofluorescent staining to detect glucagon receptor (GCGR) and glucagon-like peptide-1 receptor (GLP-1R) expression. Antibodies were used at concentrations previously validated by the Hodson laboratory (220), and the staining protocol was generously provided by Dr. M. Golson (private communication).

To identify β-cells, co-staining for insulin and GLP-1R was performed following the current understanding in the literature that GLP-1R expression is restricted to insulin-producing β-cells (1). This approach doubled as a validation of the observed staining, as INSULIN+ cells were expected to overlap with GLP-1R+ cells.

Native islets from both female (n=9, Fig. 21b) and male (n=3, Fig. 21c) donors showed no significant differences in total insulin or glucagon content under culture conditions supplemented with either glucagon (+ GCG) or GLP-1 (+ GLP-1), suggesting that exogenous hormone supplementation does not alter hormone synthesis in native islets. Hormone secretion was normalized to the number of IEQ and measured at basal glucose (2.8 mM), high glucose (22.2 mM), and in the presence of 30 mM KCl to assess maximal depolarization-induced release (stimulation protocol detailed in Appendix Fig. 3). Basal glucose-induced secretion was used as a baseline to express % of hormone secretion in response to high glucose and 30 mM KCl. Islets from female donors exhibited no significant difference in insulin (Fig. 21d_i) or glucagon (Fig. 21f_i) secretion across these conditions. In contrast, male donor islets

showed a canonical secretory pattern, with stepwise increases in insulin release in response to increasing glucose concentrations, and a peak following KCl stimulation (Fig. 21e). Aside from the CTRL condition, a similar canonical pattern was observed for glucagon secretion. Here, decreasing values are expected with increasing glucose concentration. The + KCl condition is still expected to reflect total hormone release. However, not enough data could be collected from male donors to generate a strong data foundation. For pseudo-islets, data availability was even more scarce, considering the elaborate path of their generation. Despite that, some female donor-derived pseudo-islets could be analyzed for both insulin and glucagon secretion (Fig. 21d_{ii} and f_{ii}, respectively). Here, secretion levels were normalized per pseudo-IEQ used in the experiment and expressed as % secretion of the control (= α+β+δ:MS1). Again, a canonical pattern represents increased insulin release with increasing glucose concentration but decreased glucagon release under the same conditions.

Receptor expression: To better understand the differences between islets from male and female donors, we quantified receptor expression levels by immunohistochemistry (Fig. 21a). Native and pseudo-islets were immunostained and imaged by confocal microscopy using single-plane and z-stack acquisition. Representative slices from z-stack projections are shown in Fig. 21h. Image processing and quantitative analysis were conducted using Fiji and a custom pipeline implemented in CellProfiler (see Appendix Fig. 5). Nuclei were identified by DAPI staining and expanded by 15 pixels to approximate cytoplasmic boundaries. Fluorescent signals for GCGR, GLP-1R, and insulin were mapped onto DAPI-positive regions, and only cells with overlapping signals in the cytoplasmic region were classified as positive for each marker. Cell counts were quantified for each condition and normalized to the total number of DAPI+ nuclei. Both native and pseudo-islets from male and female donors exhibited similar cellular GPCR composition, with approximately 40 % GCGR+ cells, 20 % GLP-1R+ cells, and 15 % INSULIN+ cells (Fig. 21j and k). Notably, pseudo-islets displayed more intense immunostaining than native islets, presumably due to improved antigen accessibility (Fig. 21i).

4.6 Summary

Collectively, our findings reveal several novel insights into islet biology. First, in MIN6 and αTC1 cell line experiments, GCG selectively enhanced β-cell (MIN6) proliferation without affecting α-cell (αTC1) growth, underscoring the distinct responses of different islet cell types. By using selective antagonists for the glucagon receptor (GCGR) and GLP-1 receptor (GLP-1R), we confirmed that these effects are mediated directly through their respective receptors, thereby establishing a mechanistic basis for hormone-driven islet cell expansion.

When translated to human islets, hormone supplementation uncovered a sex dependence in the structural stability of native islets, while in reconstituted pseudo-islets, the growth response to GCG and GLP-1 was less dependent on the donor sex but varied with time and according to the cellular composition of the pseudo-islet.

After evaluating islet preparations from multiple donors and isolation centers, we established the following best practices to generate healthy pseudo-islets. Native islets should have minimal culture time before shipment (each islet offer specifies duration) and must not be precultured before FACS. Reserve a subset of fresh islets as native controls before dissociation to account for heterogeneity. Process incoming islets on the day of receipt whenever possible; otherwise, store at 4 °C, in shipping media, and use within seven days. Dissociate using 0.05 % trypsin-EDTA (other digestion methods may harm antibody epitopes), monitoring under light microscopy to stop digestion once only single cells remain and no large clusters persist. After sorting, immediately resuspend cells in fresh media containing penicillin/streptomycin and amphotericin B to prevent contamination. Standard cell culture plates promote adhesion; therefore, seed cells in ultra-low attachment plates together with MS1 endothelial cells at a 1:10 endocrine-to-MS1 ratio. MS1 cells support 3D reaggregation but have been reported not to proliferate in suspension. Clusters begin forming within 2–3 days and continue maturing up to 14 days,

depending on the cellular composition of the pseudo-islet. Additionally, most combinations show the complete spectrum of islet diameters measured (30-300 μm) at the first 2-3 days post-seeding timepoint, suggesting that pseudo-islet formation occurs quickly. Therefore, we would suggest including an earlier observation time point. Sometimes, for example, for both male and female β+δ combinations, longer culture yields larger pseudo-islets but may increase functional stress.

Hormone supplementation effects were sex-dependent. Female donor–derived native islets fragmented in response to hormone supplementation and should not be cultured with supplements. Male donor–derived native islets, in contrast, benefited from supplementation, which slowed fragmentation relative to controls. For pseudo-islets, β+δ combinations showed the most consistent cluster formation. In female donor–derived pseudo-islets, β+δ clusters remained stable for up to 10 days without significant fragmentation. Glucagon supplementation was tolerated, but unsupplemented conditions yielded better outcomes. In male donor–derived β+δ pseudo-islets, early time points were optimal, with robust cluster formation within the first 5 days. Glucagon supplementation improved stability and is preferred over unsupplemented conditions.

Certain combinations were more prone to fragmentation and should be avoided or time-limited. In male donor–derived α+β+δ pseudo-islets, GLP-1 supplementation promoted fragmentation, whereas control and GCG-treated conditions remained stable up to 10 days, with GCG being preferred. Male donor–derived α+β pseudo-islets fragmented under all conditions and should be used, if at all, within the first 3 days of culture. In contrast, female donor–derived α+β pseudo-islets formed clusters with both GCG and GLP-1 supplementation, with GLP-1 yielding more mature aggregates. However, culture duration should not exceed 7 days, as fragmentation becomes evident by days 9–10.

4.7 Discussion

We demonstrate that supplementation with GCG and GLP-1 differentially affects growth, native islet fragmentation in culture, and pseudo-islet formation, with the magnitude of the effect depending on the specific cell type(s) present. In pancreatic cell lines, GLP-1 supplementation was growth beneficial for both α- and β-cells, whereas GCG supplementation appeared to selectively support β-cells (Fig. 17). This cell type-specificity is likely explained by the endogenous secretion of GCG by α-cells, which may saturate GCGR signaling in these cells, rendering additional GCG ineffective. Conversely, β-cells that do not have endogenous GCG remain sensitive to exogenous GCG.

Supporting this interpretation, the beneficial effects of GCG on β-cells were abolished when GCGR was pharmacologically inhibited using GCGRIIα. This highlights that the observed improvements in β-cell growth following GCG supplementation are dependent on intact GCGR signaling.

In αTC1 cells, GCG alone (at 0.1 μg/mL; ≈ 30 nM) produced only a modest proliferative effect, compared to GLP-1 at the same concentration. When both hormones were combined, GCG competed for GLP-1R binding (EC_{50} for GLP-1R–mediated cAMP production is ~ 36 nM (221)), thereby displacing GLP-1 and acting as a partial agonist. This likely suppressed the robust growth otherwise induced by GLP-1. When the GCGR antagonist GCGRIIα was added at 1 μM, GCGR signaling was fully blocked, diverting both exogenous GCG and any endogenous ligand to GLP-1R, and this diversion elicited a strong proliferative response even in the absence of added GLP-1. Therefore, in the presence of both GCG (~ 30 nM) and 1 μM GCGRIIα, GCG cannot signal through GCGR and instead engages GLP-1R. However, because GCGs intrinsic efficacy at GLP-1R is lower than that of GLP-1, it slightly blunts the maximal proliferative signal seen with GCGRIIα alone. Yet, it still drives substantially greater growth than GCG treatment by itself.

Interestingly, sex-specific differences emerged in response to both islet culture and hormone supplementation. Fragmentation rates differed between male and female donors. Male native islets benefited from both GCG and GLP-1 supplementation, as they slowed fragmentation compared to control conditions. However, female-derived native islets seemed to fragment faster under supplemented conditions, with + GLP-1 being the most fragmentation-prone condition. Female native islets being more sensitive to hormone supplementation and responding with faster fragmentation could represent a physiological adaptation unique to female islets. Estrogen and other sex hormones have been shown to enhance β-cell survival, proliferation, and insulin secretion, particularly under stress conditions (89,186). Across their lifespan, females experience substantial hormonal fluctuations during the menstrual cycle, pregnancy, and menopause. The capacity for dynamic reorganization of islet architecture, including fast aggregation and reaggregation, may therefore serve a protective or regulatory function in response to these hormonal shifts. While the precise mechanistic link between hormone-driven plasticity and islet dynamics remains to be defined, these findings underscore the importance of considering sex as a biological variable in islet physiology and highlight the potential for sex-specific therapeutic strategies in diabetes.

Pseudo-islet in culture behavior was less sex-specific and driven more by the cellular makeup of the pseudo-islets, although male-donor-derived and female-donor-derived pseudo-islets did show differences.

Both female- and male-derived pseudo-islets respond to GCG and GLP-1 supplementation during early stages of pseudo-islet formation, with evidence of increased fragmentation or maturation depending on the condition. Pseudo-islets derived from female donors exhibited early and faster cluster formation, as indicated by higher cluster counts (more clusters/cluster-forming cell) at 2-3 days post-seeding compared to male-donor-derived pseudo-islets. Male-donor-derived pseudo-islets showed overall lower mean cluster counts (fewer clusters/cluster-forming cell), which indicates that each cluster contained

more cells. Over longer culture periods (9–10 d), signs of fragmentation emerge, particularly in female-derived pseudo-islets treated with GLP-1. Increased subcluster percentages and a decline in cluster counts indicate this. In male-derived pseudo-islets, fragmentation tends to occur earlier, often by 6–7 days. This is also most pronounced in the + GLP-1 condition. In contrast, GCG supplementation was mostly beneficial for pseudo-islet formation and helped shift toward larger clusters. These findings are consistent with prior co-culture studies, which demonstrated that the presence of GCG- and GLP–1–secreting cells enhances β-cell insulin secretion, proliferation, and resilience to cytotoxic insults (222). However, our study adds the nuance that the supplementation benefit is highly dependent on donor sex and, most importantly, the cellular composition of the islet being formed.

Although hormone supplementation led to notable changes in islet morphology, we did not observe any corresponding differences in hormone secretion from native islets, regardless of sex. This indicates that the structural changes induced by GCG or GLP-1 are not functionally harmful and may in fact reflect a degree of functional resilience in islet hormone output. It is important to consider that islet structure and function are not always tightly linked; alterations such as fragmentation or changes in cluster size may represent adaptive responses to the culture environment rather than early signs of dysfunction. These morphological adaptations could support survival or remodeling without compromising secretory capacity. Additionally, our current assays may not capture subtle changes in function, or the time frame of our culture conditions may be too short to reveal delayed functional effects. Therefore, while morphology was affected, these changes do not appear to impair endocrine function under the conditions tested.

Differences in receptor expression, as visualized in Fig. 21f, were originally hypothesized as the cause of seeing differences in the way cell lines, islets, and pseudo-islets respond. However, although they provide additional insight into the cellular composition and availability of the receptors, there does not seem to be a significant difference between female and male donors. Pseudo-islets exhibited more

intense GCGR and GLP-1R staining compared to native islets. This may be due to selection bias introduced during FACS sorting, which enriches for endocrine cells and therefore increases the relative density of receptor-expressing cells in pseudo-islets. It is also possible that improved epitope accessibility in smaller pseudo-islets enhances staining intensity, consistent with their more compact structure and reduced extracellular matrix components.

Finally, when comparing our data on receptor-expressing populations with published datasets, we note that previous reports using mass cytometry (CyTOF) have often described higher proportions of GCGR+ and GLP-1R+ cells (35) (Appendix Fig. 2a). However, these differences likely stem from methodological discrepancies, as our study employed FACS-based quantification, which may underrepresent certain populations due to gating thresholds or epitope availability.

Overall, our findings emphasize the importance of selecting the appropriate model system based on the biological process under investigation. Native islets represent the mature, final state of islet architecture and are therefore limited in their utility for studying the effects of hormone supplementation during islet formation. In contrast, pseudo-islets provide a dynamic and controllable model that more accurately captures early stages of reaggregation and cellular adaptation. Our results further underscore the need to consider sex, cellular context, and methodological approach when evaluating islet function and receptor expression.

Chapter 5 Discussion

5.1 Common Themes

The work presented in this dissertation investigates mechanisms that regulate insulin secretion (Chapter 2) and islet organization (Chapters 3 and 4), progressing from molecular receptor signaling to the influence of donor-specific factors on human islet biology. Although each chapter explores a distinct experimental dimension, several unifying concepts emerge that collectively emphasize the contextual nature of β-cell regulation, the limitations of model systems, and the importance of donor variability in shaping islet behavior.

Insulin secretion from pancreatic β-cells is a tightly controlled process that requires fine-tuning to maintain glucose homeostasis. One mechanism contributing to this regulation is the network of GPCRs expressed by β-cells. Chapter 2 focused on TAAR1, a low-abundance but functionally relevant GPCR, and its endogenous ligands, TAs. Our findings indicate that TAs may serve as autocrine signaling molecules that modulate insulin secretion in a glucose-dependent manner. However, this regulation proved both amine- and context-dependent.

We find that PEA acted as a weak partial agonist at TAAR1, producing glucose- and dose-dependent increases in insulin secretion. In contrast, TYR displayed a more complex, bidirectional response pattern that likely reflects engagement of multiple signaling pathways, including potential cross-talk with adrenergic receptors. Notably, the EC_{50} values derived from our β-cell assays were higher than those reported in heterologous overexpression systems, underscoring the influence of assay context and receptor reserve on apparent ligand potency.

Using mice, we generated both *in vivo* and *in vitro* results. Unexpectedly, we find that they did not align perfectly: TAAR1-KO mice exhibited impaired glucose tolerance (Fig. 11d and e), yet isolated β-cells

from these animals failed to show clear differences in Ca^{2+} signaling (Fig. 11g-j). Upon further investigation, we identified that the mouse strain used (C57BL6/J) carried a loss-of-function mutation in Nnt, a mitochondrial enzyme required for redox balance and insulin secretion (127–129). This background defect likely masked TAAR1-specific effects. Furthermore, previous reports indicate that the impact of this defect is age-dependent, which likely explains why TAAR1-dependent effects were detectable in our younger *in vivo* cohort but absent in the older *in vitro* cohort (127). These findings highlight a broader theme: the challenge of translating rodent data to human systems, particularly when strain-specific mutations confound interpretation.

Recognizing the translational limitations of rodent models, Chapter 3 shifted focus to human islets to examine how donor-specific features and environmental cues (exogenous hormone supplementation) interact to influence islet behavior. Using native islets from multiple donors, we demonstrated that their structural and functional responses to GCG and GLP-1 supplementation were strongly modulated by donor characteristics, including sex, BMI, A1c, and age.

These findings reveal that human islets retain a distinct donor “signature,” which dictates how they respond to external stimuli. Donor variability manifested in measurable differences in islet fragmentation, morphology, and cluster dynamics, reflecting intrinsic physiological adaptations shaped by metabolic and hormonal background. For example, islets from donors with higher BMI displayed altered responsiveness consistent with a stressed metabolic phenotype, while sex differences suggested differential hormonal priming.

However, the inherent complexity of native islets makes it difficult to disentangle the contribution of individual cell populations. To address this, we developed pseudo-islets as a reductionist yet physiologically relevant model system. By reaggregating sorted endocrine cells from human donors, we could systematically vary cell-type composition while maintaining functional integrity. In contrast to native islets, pseudo-islets exhibited diminished influence of donor characteristics. Instead, their behavior was

predominantly governed by their cellular make-up, that is, by the relative presence or absence of α-, β-, and δ-cells. The composition of pseudo-islets determined how they responded to hormone supplementation (GCG or GLP-1), revealing that islet architecture and paracrine communication are central regulators of collective islet behavior.

Diving in deeper, chapter 4 further dissected donor-dependent effects by examining sex as a biological variable in both native and pseudo-islet systems. We observed that female-derived islets exhibited greater structural plasticity and a higher degree of fragmentation and remodeling in response to GCG and GLP-1 supplementation. This behavior likely reflects an intrinsic adaptability of female β-cells to cyclical hormonal fluctuations associated with reproductive physiology. In contrast, male islets appeared more structurally stable but less dynamically responsive.

Interestingly, these sex-dependent differences were less pronounced in pseudo-islets, suggesting that the process of reaggregation and standardized cellular composition may mitigate or “reset” donor-imprinted characteristics. Mechanistically, differences in GCGR and GLP-1R expression were initially hypothesized to underlie sex-specific responses, but our data did not support this (Fig. 21). This indicates that other factors, such as downstream signaling divergence, receptor cross-talk, or epigenetic modulation, may drive sex-dependent islet plasticity.

Taken together, the findings across Chapters 2–4 converge on three overarching themes: 1) GPCR networks, exemplified by TAAR1, fine-tune β-cell function through autocrine and context-dependent signaling. 2) Human islet responses are strongly influenced by donor-specific characteristics, emphasizing the importance of proper donor stratification and careful interpretation of variability; and 3) in reconstituted pseudo-islet systems, cellular composition and paracrine organization emerge as the primary determinants of functional outcomes.

5.2 Future Directions

Several lines of investigation emerge from these findings. First, TAAR1 research should be refined using animal models with intact glucose homeostasis to minimize background strain–related confounders, such as *Nnt* mutations in our case. Ideally, a β-cell–specific TAAR1 KO should be developed to isolate islet-autonomous effects and distinguish them from TAAR1s' central actions. Second, rigorous donor stratification remains essential in human islet research, as sex, BMI, A1c, and age strongly influence responsiveness. Translationally, GCG and GLP-1 supplementation may stabilize native islets or enhance pseudo-islet integrity, though such interventions must be adapted to donor-specific characteristics and pseudo-islet composition. Finally, future work should investigate the mechanistic basis of sex- and hormone-dependent differences, as receptor expression alone does not appear to account for the distinct effects of GCG and GLP-1. Identifying downstream signaling pathways and molecular drivers of female islet plasticity may uncover protective mechanisms with therapeutic relevance for diabetes pathophysiology.

Beyond the biological aspects, the complexity and sensitivity of pseudo-islet generation highlight a pressing need for predictive tools that can anticipate experimental outcomes. Given the intricate, multistep workflow and numerous points at which variability may arise, approaches capable of estimating success before experimentation would greatly enhance reproducibility and resource efficiency. Currently, parameters such as donor purity or the number of IEQs ordered provide limited predictive value. A promising future direction is to harness the extensive donor metadata routinely collected by islet distribution centers. While this thesis primarily considered sex, BMI, A1c, and age, additional variables, such as blood group, medical history, blood glucose, genetic variants, and demographic factors (among others), could be leveraged to generate individualized "donor signatures." Machine learning models trained on these multidimensional datasets could predict endocrine cell yields or sorting outcomes,

thereby informing donor selection and experimental design. Ultimately, such an approach could transform pseudo-islet research by reducing variability, minimizing waste of valuable human material, and accelerating the translation of *in vitro* findings toward clinically relevant applications.

5.3 Concluding Remarks

This dissertation highlights the multifaceted regulation of insulin secretion and islet organization across molecular, cellular, and physiological levels. In Chapter 2, we established that TAAR1 and its ligands act as autocrine modulators of insulin secretion, integrating amine-specific and glucose-dependent cues. However, system- and species-dependent differences underscore the importance of experimental context and genetic background.

Chapters 3 and 4 extended this perspective to human islets, revealing that donor characteristics exert substantial influence on islet structure and responsiveness, and that sex, in particular, shapes islet plasticity. By contrast, pseudo-islet models reduce donor variability and enable dissection of how cellular composition governs collective behavior. These complementary systems, native and engineered, together illustrate that biological context fundamentally defines islet function.

In summary, insulin secretion and islet organization cannot be fully understood through a single model or variable. GPCR-mediated autocrine signaling, donor-specific factors, and cell-type composition collectively determine islet responses to environmental challenges. A comprehensive understanding of these interconnected layers will be essential for translating experimental findings into improved strategies for preserving or restoring β-cell function in diabetes.

References

1. Fisher R. American Diabetes Association Releases 2023 Standards of Care in Diabetes to Guide Prevention, Diagnosis, and Treatment for People Living with Diabetes.

2. Cryer PE, Davis SN, Shamoon H. Hypoglycemia in Diabetes. Diabetes Care. 2003 June 1;26(6):1902–12.

3. Rutter GA, Pullen TJ, Hodson DJ, Martinez-Sanchez A. Pancreatic β-cell identity, glucose sensing and the control of insulin secretion. Biochemical Journal. 2015 Mar 1;466(2):203–18.

4. Unger RH, Cherrington AD. Glucagonocentric restructuring of diabetes: a pathophysiologic and therapeutic makeover. J Clin Invest. 2012 Jan 3;122(1):4–12.

5. Atkinson MA, Eisenbarth GS, Michels AW. Type 1 diabetes. The Lancet. 2014 Jan;383(9911):69–82.

6. Porte, Jr D. Clinical importance of insulin secretion and its interaction with insulin resistance in the treatment of type 2 diabetes mellitus and its complications. Diabetes Metab Res Rev. 2001 May;17(3):181–8.

7. Nathan DM. Diabetes: Advances in Diagnosis and Treatment. JAMA. 2015 Sept 8;314(10):1052.

8. Bosco D, Armanet M, Morel P, Niclauss N, Sgroi A, Muller YD, et al. Unique Arrangement of - and -Cells in Human Islets of Langerhans.

9. Ravier M a, Gu M, Charollais A, Gjinovci A, Wollheim CB, Willecke K, et al. Insulin Oscillations , and Basal Insulin Release. Diabetes. 2005;54(June):1798–807.

10. Hauge-Evans AC, Anderson RL, Persaud SJ, Jones PM. Delta cell secretory responses to insulin secretagogues are not mediated indirectly by insulin.

11. Rorsman P, Huising MO. The somatostatin-secreting pancreatic δ-cell in health and disease HHS Public Access. Nat Rev Endocrinol. 2018;14(7):404–14.

12. AC HE, AJ K, D C, CC R, IC R, MJ L, et al. Somatostatin secreted by islet delta-cells fulfills multiple roles as a paracrine regulator of islet function. Diabetes. 2009 Feb;58(2):403–11.

13. El K, Gray SM, Capozzi ME, Knuth ER, Jin E, Svendsen B, et al. GIP mediates the incretin effect and glucose tolerance by dual actions on a-cells and b-cells. Sci Adv. 2021;7:1–10.

14. Henquin J claude. Triggering and Amplifying Pathways of Regulation of Insulin Secretion by Glucose. Diabetes. 2000;49:1751–60.

15. Ahrén B. Autonomic regulation of islet hormone secretion - Implications for health and disease. Diabetologia. 2000 Apr 13;43(4):393–410.

16. Thorens B. Neural regulation of pancreatic islet cell mass and function. Diabetes Obesity Metabolism. 2014 Sept;16(S1):87–95.

17. Husted AS, Trauelsen M, Rudenko O, Hjorth SA, Schwartz TW. GPCR-Mediated Signaling of Metabolites. Cell Metabolism. 2017 Apr;25(4):777–96.

18. Winzell MS, Ahrén B. G-protein-coupled receptors and islet function—Implications for treatment of type 2 diabetes. Pharmacology & Therapeutics. 2007 Dec;116(3):437–48.

19. Fridlyand LE, Philipson LH. Pancreatic Beta Cell G-Protein Coupled Receptors and Second Messenger Interactions: A Systems Biology Computational Analysis. Cai T, editor. PLoS ONE. 2016 May 3;11(5):e0152869.

20. Shilleh AH, Viloria K, Broichhagen J, Campbell JE, Hodson DJ. GLP1R and GIPR expression and signaling in pancreatic alpha cells, beta cells and delta cells. Peptides. 2024 May 1;175:171179.

21. Campbell JE, Drucker DJ. Islet α cells and glucagon—critical regulators of energy homeostasis. Nat Rev Endocrinol. 2015 June;11(6):329–38.

22. Moede T, Leibiger IB, Berggren PO. Alpha cell regulation of beta cell function. Diabetologia. 2020 Oct;63(10):2064–75.

23. Kowluru A. GPCRs, G Proteins, and Their Impact on β-cell Function. In: Terjung R, editor. Comprehensive Physiology [Internet]. 1st ed. Wiley; 2020 [cited 2025 Sept 22]. p. 453–90. Available from: https://onlinelibrary.wiley.com/doi/10.1002/cphy.c190028

24. Drucker DJ. GLP-1-based therapies for diabetes, obesity and beyond. Nat Rev Drug Discov. 2025 Aug;24(8):631–50.

25. Drucker DJ. Mechanisms of Action and Therapeutic Application of Glucagon-like Peptide-1. Cell Metabolism. 2018 Apr;27(4):740–56.

26. Arrojo E Drigo R, Ali Y, Diez J, Srinivasan DK, Berggren PO, Boehm BO. New insights into the architecture of the islet of Langerhans: a focused cross-species assessment. Diabetologia. 2015 Oct;58(10):2218–28.

27. Félix-Martínez GJ, Godínez-Fernández JR. Comparative analysis of reconstructed architectures from mice and human islets. Islets. 2022 Dec 31;14(1):23–35.

28. Villaca CBP, Mastracci TL. Pancreatic Crosstalk in the Disease Setting: Understanding the Impact of Exocrine Disease on Endocrine Function. In: Prakash YS, editor. Comprehensive Physiology [Internet]. 1st ed. Wiley; 2024 [cited 2025 Sept 12]. p. 5371–87. Available from: https://onlinelibrary.wiley.com/doi/10.1002/cphy.c230008

29. Rorsman P, Ashcroft FM. Pancreatic β-Cell Electrical Activity and Insulin Secretion: Of Mice and Men. Physiological Reviews. 2018 Jan 1;98(1):117–214.

30. Rorsman P, Ashcroft FM. Pancreatic β-cell electrical activity and insulin secretion: Of mice and men. Physiological Reviews. 2018;98(1):117–214.

31. Strowski MZ, Blake AD. Function and expression of somatostatin receptors of the endocrine pancreas. Mol Cell Endocrinol. 2008 May 14;286(1–2):169–79.

32. Ren H, Li Y, Xie B, Qian W, Yu Y, Chang T, et al. δ-α cell-to-cell interactions modulate pancreatic islet Ca2+ oscillation modes [Internet]. bioRxiv; 2024 [cited 2025 July 9]. p. 2024.08.21.608986. Available from: https://www.biorxiv.org/content/10.1101/2024.08.21.608986v1

33. Hauge-Evans AC, King AJ, Carmignac D, Richardson CC, Robinson ICAF, Low MJ, et al. Somatostatin Secreted by Islet δ-Cells Fulfills Multiple Roles as a Paracrine Regulator of Islet Function. Diabetes. 2009 Feb;58(2):403–11.

34. Weitz J, Menegaz D, Caicedo A. Deciphering the Complex Communication Networks That Orchestrate Pancreatic Islet Function. Diabetes. 2021 Jan 1;70(1):17–26.

35. Cabrera O, Berman DM, Kenyon NS, Ricordi C, Berggren PO, Caicedo A. The unique cytoarchitecture of human pancreatic islets has implications for islet cell function [Internet]. Vol. 14, PNAS February. 2006 p. 2334–9. Available from: www.pnas.orgcgidoi10.1073pnas.0510790103

36. Da Silva Xavier G. The Cells of the Islets of Langerhans. Journal of Clinical Medicine. 2018;7(3):54.

37. Montet X, Lamprianou S, Vinet L, Meda P, Fort A. Islets of Langerhans. Islam SMd (Editor), editor. Springer Reference; 2015. 59–77 p.

38. Wierup N, Svensson H, Mulder H, Sundler F. The ghrelin cell: A novel developmentally regulated islet cell in the human pancreas. Regulatory Peptides. 2002;107(1–3):63–9.

39. Brereton MF, Vergari E, Zhang Q, Clark A. Alpha-, Delta- and PP-cells: Are They the Architectural Cornerstones of Islet Structure and Co-ordination? http://dx.doi.org/101369/0022155415583535. 2015 July 27;63(8):575–91.

40. J L, P D, LC W, PL R, JC T. Pancreatic polypeptide. A review. Archives of surgery (Chicago, Ill : 1960). 1981;116(10):1256–64.

41. Kim A, Miller K, Jo J, Kilimnik G, Wojcik P, Hara M. Islet architecture: A comparative study. Islets. 2009;1(2):129–36.

42. Brissova M. Assessment of Human Pancreatic Islet Architecture and Composition by Laser Scanning Confocal Microscopy. Journal of Histochemistry and Cytochemistry. 2005;53(9):1087–97.

43. Braun M, Ramracheya R, Amisten S, Bengtsson M, Moritoh Y, Zhang Q, et al. Somatostatin release, electrical activity, membrane currents and exocytosis in human pancreatic delta cells. Diabetologia. 2009 Aug 1;52(8):1566–78.

44. Adams MT, Blum B. Determinants and dynamics of pancreatic islet architecture. Islets. 14(1):82–100.

45. Lehrstrand J, Davies WIL, Hahn M, Korsgren O, Alanentalo T, Ahlgren U. Illuminating the complete ß-cell mass of the human pancreas- signifying a new view on the islets of Langerhans. Nat Commun. 2024 Apr 18;15(1):3318.

46. Richards OC, Raines SM, Attie AD. The role of blood vessels, endothelial cells, and vascular pericytes in insulin secretion and peripheral insulin action. Endocr Rev. 2010 June;31(3):343–63.

47. Cleaver O, Dor Y. Vascular instruction of pancreas development. Development. 2012 Aug 15;139(16):2833–43.

48. Bosco D, Armanet M, Morel P, Niclauss N, Sgroi A, Muller YD, et al. Unique arrangement of alpha- and beta-cells in human islets of Langerhans. Diabetes. 2010 May;59(5):1202–10.

49. Rodriguez-Diaz R, Abdulreda MH, Formoso AL, Gans I, Ricordi C, Berggren PO, et al. Innervation patterns of autonomic axons in the human endocrine pancreas. Cell Metab. 2011 July 6;14(1):45–54.

50. Scharfmann R, Staels W, Albagli O. The supply chain of human pancreatic β cell lines. Journal of Clinical Investigation. 2019 Sept 3;129(9):3511–20.

51. Hart NJ, Weber C, Price N, Banuelos A, Schultz M, Huey B, et al. Insulinoma-derived pseudo-islets for diabetes research. American Journal of Physiology - Cell Physiology. 2021 Aug 1;321(2):C247–56.

52. Potdar P, Kharat A, Sanap A, Kheur S, Bhonde R. Pancreatic β cell models for screening insulin secretagogues and cytotoxicity. J of Applied Toxicology. 2025 Jan;45(1):89–106.

53. Meier RPH, Ben Nasr M, Fife BT, Finger EB, Fiorina P, Luo X, et al. Best practices in islet transplantation in mice. American Journal of Transplantation. 2025 July;25(7):1399–409.

54. Wagner LE, Melnyk O, Duffett BE, Linnemann AK. Mouse models and human islet transplantation sites for intravital imaging. Front Endocrinol. 2022 Oct 5;13:992540.

55. Gloyn AL, Ibberson M, Marchetti P, Powers AC, Rorsman P, Sander M, et al. Every islet matters: improving the impact of human islet research. Nat Metab. 2022 Aug 11;4(8):970–7.

56. Imai Y, Soleimanpour SA, Tessem JS. Editorial: Study of pancreatic islets based on human models to understand pathogenesis of diabetes. Front Endocrinol. 2023 Jan 9;13:1128653.

57. Scharfmann R, Rachdi L, Ravassard P. Concise Review: In Search of Unlimited Sources of Functional Human Pancreatic Beta Cells. Stem Cells Translational Medicine. 2013 Jan 1;2(1):61–7.

58. Sali S, Azzam L, Jaro T, Ali AAG, Mardini A, Al-Dajani O, et al. A perfect islet: reviewing recent protocol developments and proposing strategies for stem cell derived functional pancreatic islets. Stem Cell Res Ther. 2025 Mar 31;16(1):160.

59. Félix-Martínez GJ, Godínez-Fernández JR. A primer on modelling pancreatic islets: from models of coupled β-cells to multicellular islet models. Islets. 2023 Dec 31;15(1):2231609.

60. Dwulet JM, Briggs JK, Benninger RKP. Small subpopulations of β-cells do not drive islet oscillatory [Ca2+] dynamics via gap junction communication. Rubin J, editor. PLoS Comput Biol. 2021 May 3;17(5):e1008948.

61. Glieberman AL, Pope BD, Zimmerman JF, Liu Q, Ferrier JP, Kenty JHR, et al. Synchronized stimulation and continuous insulin sensing in a microfluidic human Islet on a Chip designed for scalable manufacturing. Lab on a Chip. 2019;19(18):2993–3010.

62. Yin J, Meng H, Lin J, Ji W, Xu T, Liu H. Pancreatic islet organoids-on-a-chip: how far have we gone? J Nanobiotechnol. 2022 Dec;20(1):308.

63. Regeenes R, Rocheleau JV. Twenty years of islet-on-a-chip: microfluidic tools for dissecting islet metabolism and function. Lab Chip. 2024;24(5):1327–50.

64. Huang Y, Huang Z, Tang Z, Chen Y, Huang M, Liu H, et al. Research Progress, Challenges, and Breakthroughs of Organoids as Disease Models. Front Cell Dev Biol [Internet]. 2021 Nov 16 [cited 2025 July 11];9. Available from: https://www.frontiersin.org/journals/cell-and-developmental-biology/articles/10.3389/fcell.2021.740574/full

65. Lancaster MA, Renner M, Martin CA, Wenzel D, Bicknell LS, Hurles ME, et al. Cerebral organoids model human brain development and microcephaly. Nature. 2013 Sept;501(7467):373–9.

66. McCracken KW, Catá EM, Crawford CM, Sinagoga KL, Schumacher M, Rockich BE, et al. Modelling human development and disease in pluripotent stem-cell-derived gastric organoids. Nature. 2014 Dec;516(7531):400–4.

67. Sato T, Vries RG, Snippert HJ, van de Wetering M, Barker N, Stange DE, et al. Single Lgr5 stem cells build crypt-villus structures in vitro without a mesenchymal niche. Nature. 2009 May;459(7244):262–5.

68. Huch M, Gehart H, van Boxtel R, Hamer K, Blokzijl F, Verstegen MMA, et al. Long-term culture of genome-stable bipotent stem cells from adult human liver. Cell. 2015 Jan 15;160(1–2):299–312.

69. Takasato M, Er PX, Chiu HS, Maier B, Baillie GJ, Ferguson C, et al. Kidney organoids from human iPS cells contain multiple lineages and model human nephrogenesis. Nature. 2015 Oct;526(7574):564–8.

70. Wassmer CH, Lebreton F, Bellofatto K, Bosco D, Berney T, Berishvili E. Generation of insulin-secreting organoids: a step toward engineering and transplanting the bioartificial pancreas. Transplant International. 2020;33(12):1577–88.

71. Darrigrand JF, Isaacson A, Spagnoli FM. Generation of human iPSC-derived pancreatic organoids to study pancreas development and disease [Internet]. 2024 [cited 2025 July 10]. Available from: http://biorxiv.org/lookup/doi/10.1101/2024.10.24.620102

72. Rezania A, Bruin JE, Arora P, Rubin A, Batushansky I, Asadi A, et al. Reversal of diabetes with insulin-producing cells derived in vitro from human pluripotent stem cells. Nat Biotechnol. 2014 Nov;32(11):1121–33.

73. Li Y, Xu M, Chen J, Huang J, Cao J, Chen H, et al. Ameliorating and refining islet organoids to illuminate treatment and pathogenesis of diabetes mellitus. Stem Cell Research & Therapy. 2024 June 27;15(1):188.

74. Benninger RKP, Head WS, Zhang M, Satin LS, Piston DW. Gap junctions and other mechanisms of cell-cell communication regulate basal insulin secretion in the pancreatic islet. Journal of Physiology. 2011;589(22):5453–66.

75. Rocheleau JV, Remedi MS, Granada B, Head WS, Koster JC, Nichols CG, et al. Critical role of gap junction coupled KATP channel activity for regulated insulin secretion. PLoS Biology. 2006;4(2):221–7.

76. Hofer M, Lutolf MP. Engineering organoids. Nat Rev Mater. 2021 Feb 19;6(5):402–20.

77. Holter MM, Saikia M, Cummings BP. Alpha-cell paracrine signaling in the regulation of beta-cell insulin secretion. Frontiers in Endocrinology. 2022 July 26;13:934775.

78. Yosten GLC. Alpha cell dysfunction in type 1 diabetes. Peptides. 2018;100:54–60.

79. Lewis PL, Wells JM. Engineering-inspired approaches to study β-cell function and diabetes. Stem Cells. 2021 May 1;39(5):522–35.

80. Hart NJ, Powers AC. Use of human islets to understand islet biology and diabetes: progress, challenges and suggestions. Diabetologia. 2019 Feb;62(2):212–22.

81. Ricordi C, Lacy PE, Finke EH, Olack BJ, Scharp DW. Automated Method for Isolation of Human Pancreatic Islets.

82. Kayton NS, Poffenberger G, Henske J, Dai C, Thompson C, Aramandla R, et al. Human islet preparations distributed for research exhibit a variety of insulin-secretory profiles. American Journal of Physiology-Endocrinology and Metabolism. 2015 Apr 1;308(7):E592–602.

83. Tuttle RL, Gill NS, Pugh W, Lee JP, Koeberlein B, Furth EE, et al. Regulation of pancreatic β-cell growth and survival by the serine/threonine protein kinase Akt1/PKBα. Nat Med. 2001 Oct;7(10):1133–7.

84. Butler AE, Janson J, Bonner-Weir S, Ritzel R, Rizza RA, Butler PC. beta-Cell Deficit and Increased beta-Cell Apoptosis in Humans With Type 2 Diabetes.

85. Henquin JC, Rahier J. Pancreatic alpha cell mass in European subjects with type 2 diabetes. Diabetologia. 2011 July;54(7):1720–5.

86. Kanat M, Winnier D, Norton L, Arar N, Jenkinson C, DeFronzo RA, et al. The Relationship Between β-Cell Function and Glycated Hemoglobin. Diabetes Care. 2011 Apr 1;34(4):1006–10.

87. Bozkurt L, Göbl CS, Leitner K, Pacini G, Kautzky-Willer A. HbA1c during early pregnancy reflects beta-cell dysfunction in women developing GDM. BMJ Open Diab Res Care. 2020 Nov;8(2):e001751.

88. Bruns CM, Baum ST, Colman RJ, Eisner JR, Kemnitz JW, Weindruch R, et al. Insulin Resistance and Impaired Insulin Secretion in Prenatally Androgenized Male Rhesus Monkeys. The Journal of Clinical Endocrinology & Metabolism. 2004 Dec;89(12):6218–23.

89. Nadal A, Alonso-Magdalena P, Soriano S, Ropero AB, Quesada I. The role of oestrogens in the adaptation of islets to insulin resistance. J Physiol. 2009 Nov 1;587(Pt 21):5031–7.

90. Ma M, Jiang T, Wen Z, Zhang D, Xiu L. Gender Differences in Relation to Body Composition, Insulin Resistance, and Islet Beta Cell Function in Newly Diagnosed Diabetic or Pre-Diabetic Patients. DMSO. 2023 Mar;Volume 16:723–32.

91. Kautzky-Willer A, Leutner M, Harreiter J. Sex differences in type 2 diabetes. Diabetologia. 2023 June;66(6):986–1002.

92. Bruns CM, Kemnitz JW. Sex Hormones, Insulin Sensitivity, and Diabetes Mellitus. ILAR Journal. 2004 Jan 1;45(2):160–9.

93. Godsland IF. Oestrogens and insulin secretion. Diabetologia. 2005 Nov;48(11):2213–20.

94. Moyce BL, Dolinsky VW. Maternal β-Cell Adaptations in Pregnancy and Placental Signalling: Implications for Gestational Diabetes. IJMS. 2018 Nov 5;19(11):3467.

95. Ernst S, Demirci C, Valle S, Velazquez-Garcia S, Garcia-Ocaña A. Mechanisms in the adaptation of maternal β-cells during pregnancy. Diabetes Management. 2011 Mar;1(2):239–48.

96. Salazar-Petres ER, Sferruzzi-Perri AN. Pregnancy-induced changes in β-cell function: what are the key players? The Journal of Physiology. 2022 Mar;600(5):1089–117.

97. Bitoska I, Krstevska B, Milenkovic T, Subeska-Stratrova S, Petrovski G, Jovanovska Mishevska S, et al. Effects of Hormone Replacement Therapy on Insulin Resistance in Postmenopausal Diabetic Women. Open Access Maced J Med Sci. 2016 Feb 1;4(1):83–8.

98. Mauvais-Jarvis F, Manson JE, Stevenson JC, Fonseca VA. Menopausal Hormone Therapy and Type 2 Diabetes Prevention: Evidence, Mechanisms, and Clinical Implications. Endocrine Reviews. 2017 June 1;38(3):173–88.

99. Borowsky B, Adham N, Jones KA, Raddatz R, Artymyshyn R, Ogozalek KL, et al. Trace amines: identification of a family of mammalian G protein-coupled receptors. Proceedings of the National Academy of Sciences of the United States of America. 2001;98(16):8966–71.

100. Bunzow JR, Sonders MS, Arttamangkul S, Harrison LM, Zhang G, Quigley DI, et al. Amphetamine, 3,4-Methylenedioxymethamphetamine, Lysergic Acid Diethylamide, and Metabolites of the Catecholamine Neurotransmitters Are Agonists of a Rat Trace Amine Receptor. Molecular Pharmacology. 2001;60(6).

101. Miller GM. The emerging role of trace amine-associated receptor 1 in the functional regulation of monoamine transporters and dopaminergic activity. Journal of Neurochemistry. 2011;116(2):164–76.

102. Lindemann L, Ebeling M, Kratochwil NA, Bunzow JR, Grandy DK, Hoener MC. Trace amine-associated receptors form structurally and functionally distinct subfamilies of novel G protein-coupled receptors. Genomics. 2005;85(3):372–85.

103. Regard JB, Kataoka H, Cano DA, Camerer E, Yin L, Zheng YW, et al. Probing cell type–specific functions of Gi in vivo identifies GPCR regulators of insulin secretion [Internet]. American Society for Clinical Investigation; 2007 [cited 2025 Sept 3]. Available from: https://www.jci.org/articles/view/32994/pdf

104. Liberles SD, Buck LB. A second class of chemosensory receptors in the olfactory epithelium. Nature. 2006;442(7103):645–50.

105. Raab S, Wang H, Uhles S, Cole N, Alvarez-Sanchez R, Künnecke B, et al. Incretin-like effects of small molecule trace amine-associated receptor 1 agonists. Molecular Metabolism. 2016 Jan;5(1):47–56.

106. Espinoza S, Gainetdinov RR. Neuronal Functions and Emerging Pharmacology of TAAR1. BC Medical Journal. 2011;53(8):404–8.

107. Revel FG, Moreau JL, Pouzet B, Mory R, Bradaia A, Buchy D, et al. A new perspective for schizophrenia: TAAR1 agonists reveal antipsychotic- and antidepressant-like activity, improve cognition and control body weight. Mol Psychiatry. 2013 May;18(5):543–56.

108. Revel FG, Moreau JL, Gainetdinov RR, Ferragud A, Velázquez-Sánchez C, Sotnikova TD, et al. Trace amine-associated receptor 1 partial agonism reveals novel paradigm for neuropsychiatric therapeutics. Biological Psychiatry. 2012;72(11):934–42.

109. Berry M. The Potential of Trace Amines and Their Receptors for Treating Neurological and Psychiatric Diseases. Reviews on Recent Clinical Trials. 2007 Jan;2(1):3–19.

110. Berry MD. Mammalian central nervous system trace amines. Pharmacologic amphetamines, physiologic neuromodulators. Journal of Neurochemistry. 2004;90(2):257–71.

111. Grandy DK. Trace amine-associated receptor 1-Family archetype or iconoclast? Pharmacology and Therapeutics. 2007;116(3):355–90.

112. Michael ES, Covic L, Kuliopulos A. Trace amine–associated receptor 1 (TAAR1) promotes antidiabetic signaling in insulin-secreting cells. Journal of Biological Chemistry. 2019 Mar;294(12):4401–11.

113. Kim H, Toyofuku Y, Lynn FC, Chak E, Uchida T, Mizukami H, et al. Serotonin regulates pancreatic beta cell mass during pregnancy. Nat Med. 2010 July;16(7):804–8.

114. Rubí B, Ljubicic S, Pournourmohammadi S, Carobbio S, Armanet M, Bartley C, et al. Dopamine D2-like Receptors Are Expressed in Pancreatic Beta Cells and Mediate Inhibition of Insulin Secretion. Journal of Biological Chemistry. 2005 Nov;280(44):36824–32.

115. Nakamura T, Yoshikawa T, Noguchi N, Sugawara A, Kasajima A, Sasano H, et al. The expression and function of histamine H_3 receptors in pancreatic beta cells. British J Pharmacology. 2014 Jan;171(1):171–85.

116. Zucchi R, Chiellini G, Scanlan TS, Grandy DK. Trace amine-associated receptors and their ligands. British Journal of Pharmacology. 2006;149(8):967–78.

117. Underhill SM, Hullihen PD, Chen J, Rizzo CF ferrer MA, Ingram SL, Amara SG. Amphetamines signal through intracellular TAAR1 receptors coupled to G α 13 and G α S in discrete subcellular domains. Molecular Psychiatry [Internet]. 2019; Available from: http://dx.doi.org/10.1038/s41380-019-0469-2

118. Xie Z, Miller GM. Beta-phenylethylamine alters monoamine transporter function via trace amine-associated receptor 1: implication for modulatory roles of trace amines in brain. J Pharmacol Exp Ther. 2008 May;325(2):617–28.

119. Regard JB, Kataoka H, Cano DA, Camerer E, Yin L, Zheng YW, et al. Probing cell type–specific functions of Gi in vivo identifies GPCR regulators of insulin secretion. Journal of Clinical Investigation. 2007 Nov 8;117(12):4034–43.

120. Bradaia A, Trube G, Stalder H, Norcross RD, Ozmen L, Wettstein JG, et al. The selective antagonist EPPTB reveals TAAR1-mediated regulatory mechanisms in dopaminergic neurons of the mesolimbic system. Proceedings of the National Academy of Sciences of the United States of America. 2009;106(47):20081–6.

121. Rutigliano G, Accorroni A, Zucchi R. The Case for TAAR1 as a Modulator of Central Nervous System Function. Front Pharmacol. 2018 Jan 10;8:987.

122. Berry MD, Gainetdinov RR, Hoener MC, Shahid M. Pharmacology of human trace amine-associated receptors: Therapeutic opportunities and challenges. Pharmacology and Therapeutics. 2017;180.

123. Espinoza S, Leo D, Sotnikova TD, Shahid M, Kääriäinen TM, Gainetdinov RR. Biochemical and Functional Characterization of the Trace Amine-Associated Receptor 1 (TAAR1) Agonist RO5263397. Front Pharmacol. 2018 June 21;9:645.

124. Nakashima K, Kanda Y, Hirokawa Y, Kawasaki F, Matsuki M, Kaku K. MIN6 Is Not a Pure Beta Cell Line but a Mixed Cell Line with Other Pancreatic Endocrine Hormones. Endocrine Journal. 2009;56(1):45–53.

125. Wolinsky TD, Swanson CJ, Smith KE, Zhong H, Borowsky B, Seeman P, et al. The Trace Amine 1 receptor knockout mouse: an animal model with relevance to schizophrenia. Genes, Brain and Behavior. 2007;6(7):628–39.

126. Decker AM, Brackeen MF, Mohammadkhani A, Kormos CM, Hesk D, Borgland SL, et al. Identification of a Potent Human Trace Amine-Associated Receptor 1 Antagonist. ACS Chem Neurosci. 2022 Apr 6;13(7):1082–95.

127. Nicholson A, Reifsnyder PC, Malcolm RD, Lucas CA, MacGregor GR, Zhang W, et al. Diet-induced Obesity in Two C57BL/6 Substrains With Intact or Mutant Nicotinamide Nucleotide Transhydrogenase (Nnt) Gene. Obesity. 2010;18(10):1902–5.

128. Fergusson G, Éthier M, Guévremont M, Chrétien C, Attané C, Joly E, et al. Defective insulin secretory response to intravenous glucose in C57Bl/6J compared to C57Bl/6N mice. Molecular Metabolism. 2014 Dec;3(9):848–54.

129. Nemoto S, Kubota T, Ohno H. Metabolic differences and differentially expressed genes between C57BL/6J and C57BL/6N mice substrains. Ryabinin AE, editor. PLoS ONE. 2022 Dec 22;17(12):e0271651.

130. Harkness JH, Shi X, Janowsky A, Phillips TJ. Trace Amine-Associated Receptor 1 Regulation of Methamphetamine Intake and Related Traits. Neuropsychopharmacology : official publication of the American College of Neuropsychopharmacology. 2015;40(February):2175–84.

131. Poueymirou WT, Auerbach W, Frendewey D, Hickey JF, Escaravage JM, Esau L, et al. F0 generation mice fully derived from gene-targeted embryonic stem cells allowing immediate phenotypic analyses. Nat Biotechnol. 2007 Jan;25(1):91–9.

132. Lenzen S, Nahrstedt H, Panten U. Monoamine oxidase in pancreatic islets, exocrine pancreas, and liver from rats. Characterization with clorgyline, deprenyl, pargyline, tranylcypromine, and amezinium. Naunyn-Schmiedeberg's Arch Pharmacol. 1983 Nov;324(3):190–5.

133. Ganic E, Johansson JK, Bennet H, Fex M, Artner I. Islet-specific monoamine oxidase A and B expression depends on MafA transcriptional activity and is compromised in type 2 diabetes. Biochemical and Biophysical Research Communications. 2015 Dec;468(4):629–35.

134. Huang YH, Ito A, Arai R. Immunohistochemical Localization of Monoamine Oxidase Type B in Pancreatic Islets of the Rat. J Histochem Cytochem. 2005 Sept;53(9):1149–58.

135. Adeghate E. The Effect of Diabetes Mellitus on the Morphology and Physiology of Monoamine Oxidase in the Pancreas. NeuroToxicology. 2004 Jan;25(1–2):167–73.

136. Müller M, Walkling J, Seemann N, Rustenbeck I. The Dynamics of Calcium Signaling in Beta Cells—A Discussion on the Comparison of Experimental and Modelling Data. IJMS. 2023 Feb 6;24(4):3206.

137. Hellman B, Gylfe E, Bergsten P, Grapengiesser E, Lund PE, Berts A, et al. Glucose induces oscillatory Ca2+ signalling and insulin release in human pancreatic beta cells. Diabetologia. 1994;37:11–20.

138. Bertram R, Sherman A, Satin LS. Electrical Bursting, Calcium Oscillations, and Synchronization of Pancreatic Islets. In: Islam MdS, editor. The Islets of Langerhans [Internet]. Dordrecht: Springer Netherlands; 2010 [cited 2025 Sept 9]. p. 261–79. (Advances in Experimental Medicine and Biology; vol. 654). Available from: http://link.springer.com/10.1007/978-90-481-3271-3_12

139. Kukkonen JP, Jansson CC, Åkerman KEO. Agonist trafficking of $G_{i/o}$ -mediated α_{2A} -adrenoceptor responses in HEL 92.1.7 cells. British J Pharmacology. 2001 Apr;132(7):1477–84.

140. Jacobson DA, Shyng SL. Ion Channels of the Islets in Type 2 Diabetes. Journal of Molecular Biology. 2020 Mar;432(5):1326–46.

141. Hauke S, Keutler K, Laguerre A, Carbo MA, Rada J, Grandy D, et al. Trace Amines are Essential Metabolites for the Autocrine Regulation of β -Cell Signaling and Insulin Secretion [Internet]. Biochemistry; 2024 [cited 2025 Dec 16]. Available from: http://biorxiv.org/lookup/doi/10.1101/2024.03.21.585773

142. Pinckaers NET, Blankesteijn WM, Mircheva A, Shi X, Opperhuizen A, Schooten FJV, et al. In Vitro Activation of Human Adrenergic Receptors and Trace Amine-Associated Receptor 1 by Phenethylamine Analogues Present in Food Supplements. Nutrients. 2024 May 22;16(11):1567.

143. Zilberg G, Parpounas AK, Warren AL, Yang S, Wacker D. Molecular basis of human trace amine-associated receptor 1 activation. Nat Commun. 2024 Jan 2;15(1):108.

144. Braun M, Ramracheya R, Rorsman P. Autocrine regulation of insulin secretion. Diabetes, obesity & metabolism. 2012;14:143–51.

145. Gilliam LK, Palmer JP, Taborsky GJ. Tyramine-Mediated Activation of Sympathetic Nerves Inhibits Insulin Secretion in Humans. The Journal of Clinical Endocrinology & Metabolism. 2007 Oct 1;92(10):4035–8.

146. Revel FG, Moreau J l, Pouzet B, Mory R, Bradaia A, Buchy D, et al. A new perspective for schizophrenia: TAAR1 agonists reveal antipsychotic- and antidepressant-like activity, improve cognition and control body weight. Molecular Psychiatry. 2012;18(January):1–14.

147. Henquin JC. Glucose-induced insulin secretion in isolated human islets: Does it truly reflect β-cell function in vivo? Molecular Metabolism. 2021 June;48:101212.

148. Davis JC, Alves TC, Helman A, Chen JC, Kenty JH, Cardone RL, et al. Glucose Response by Stem Cell-Derived β Cells In Vitro Is Inhibited by a Bottleneck in Glycolysis. Cell Reports. 2020 May;31(6):107623.

149. Henquin JC, Dufrane D, Nenquin M. Nutrient Control of Insulin Secretion in Isolated Normal Human Islets. Diabetes. 2006 Dec 1;55(12):3470–7.

150. Shiroi A, Yoshikawa M, Yokota H, Fukui H, Ishizaka S, Tatsumi K, et al. Identification of Insulin-Producing Cells Derived from Embryonic Stem Cells by Zinc-Chelating Dithizone. STEM CELLS. 2002 July;20(4):284–92.

151. Gannon M, Kulkarni RN, Tse HM, Mauvais-Jarvis F. Sex differences underlying pancreatic islet biology and its dysfunction. Molecular Metabolism. 2018 Sept;15:82–91.

152. Tiano JP, Mauvais-Jarvis F. Importance of oestrogen receptors to preserve functional β-cell mass in diabetes. Nat Rev Endocrinol. 2012 June;8(6):342–51.

153. Mauvais-Jarvis F. Role of Sex Steroids in β Cell Function, Growth, and Survival. Trends in Endocrinology & Metabolism. 2016 Dec;27(12):844–55.

154. Ihm SH, Matsumoto I, Sawada T, Nakano M, Zhang HJ, Ansite JD, et al. Effect of Donor Age on Function of Isolated Human Islets. Diabetes. 2006 May 1;55(5):1361–8.

155. Ihm SH, Moon HJ, Kang JG, Park CY, Oh KW, Jeong IK, et al. Effect of aging on insulin secretory function and expression of beta cell function-related genes of islets. Diabetes Research and Clinical Practice. 2007 Sept;77(3):S150–4.

156. Cnop M, Igoillo-Esteve M, Hughes SJ, Walker JN, Cnop I, Clark A. Longevity of human islet *α* - and *β* -cells. Diabetes Obesity Metabolism. 2011 Oct;13(s1):39–46.

157. Aguayo-Mazzucato C. Functional changes in beta cells during ageing and senescence. Diabetologia. 2020 Oct;63(10):2022–9.

158. Arrojo E Drigo R, Jacob S, García-Prieto CF, Zheng X, Fukuda M, Nhu HTT, et al. Structural basis for delta cell paracrine regulation in pancreatic islets. Nat Commun. 2019 Aug 16;10(1):3700.

159. Moin ASM, Cory M, Gurlo T, Saisho Y, Rizza RA, Butler PC, et al. Pancreatic alpha-cell mass across adult human lifespan. European Journal of Endocrinology. 2020 Feb;182(2):219–31.

160. Henquin JC. Influence of organ donor attributes and preparation characteristics on the dynamics of insulin secretion in isolated human islets. Physiol Rep. 2018 Mar;6(5):e13646.

161. Ying W, Fu W, Lee YS, Olefsky JM. The role of macrophages in obesity-associated islet inflammation and β-cell abnormalities. Nat Rev Endocrinol. 2020 Feb;16(2):81–90.

162. Linnemann AK, Davis DB. Glucagon-like peptide-1 and cholecystokinin production and signaling in the pancreatic islet as an adaptive response to obesity. J of Diabetes Invest. 2016 Apr;7(S1):44–9.

163. Wan S, An Y, Fan W, Teng F, Jiang Z. Comparative transcriptomic analysis reveals the underlying molecular mechanism in high-fat diet-induced islet dysfunction. Bioscience Reports. 2023 July 26;43(7):BSR20230501.

164. Flaquer A, Baumbach C, Kriebel J, Meitinger T, Peters A, Waldenberger M, et al. Mitochondrial Genetic Variants Identified to Be Associated with BMI in Adults. Yao YG, editor. PLoS ONE. 2014 Aug 25;9(8):e105116.

165. Bensellam M, Jonas JC, Laybutt DR. Mechanisms of β-cell dedifferentiation in diabetes: recent findings and future research directions. Journal of Endocrinology. 2018 Feb;236(2):R109–43.

166. Gannon M. Sex differences underlying pancreatic islet biology and its dysfunction.

167. Gianotti L, Belcastro S, D'Agnano S, Tassone F. The Stress Axis in Obesity and Diabetes Mellitus: An Update. Endocrines. 2021 Sept 6;2(3):334–47.

168. Atanes P, Ashik T, Persaud SJ. Obesity-induced changes in human islet G protein-coupled receptor expression: Implications for metabolic regulation. Pharmacology & Therapeutics. 2021 Dec;228:107928.

169. Matteo Ciccone M. Endothelial Function in Pre-diabetes, Diabetes and Diabetic Cardiomyopathy: A Review. J Diabetes Metab [Internet]. 2014 [cited 2025 Oct 6];05(04). Available from: https://www.omicsonline.org/open-access/endothelial-function-in-prediabetes-diabetes-and-diabetic-cardiomyopathy-2155-6156.1000364.php?aid=25586

170. Dorrell C, Schug J, Canaday PS, Russ HA, Tarlow BD, Grompe MT, et al. Human islets contain four distinct subtypes of β cells. Nat Commun. 2016 July 11;7(1):11756.

171. Dorrell C, Schug J, Lin CF, Canaday PS, Fox AJ, Smirnova O, et al. Transcriptomes of the major human pancreatic cell types. Diabetologia. 2011 Nov;54(11):2832.

172. Dorrell C, Abraham SL, Lanxon-Cookson KM, Canaday PS, Streeter PR, Grompe M. Isolation of major pancreatic cell types and long-term culture-initiating cells using novel human surface markers. Stem Cell Research. 2008 Sept 1;1(3):183–94.

173. Muraro MJ, Dharmadhikari G, Grün D, Groen N, Dielen T, Jansen E, et al. A Single-Cell Transcriptome Atlas of the Human Pancreas. Cell Systems. 2016 Oct;3(4):385-394.e3.

174. Dorrell C, Schug J, Canaday PS, Russ HA, Tarlow BD, Grompe MT, et al. Human islets contain four distinct subtypes of β cells. Nature Communications. 2016;7:1–9.

175. Robert JMH, Amoussou NG, Mai HL, Logé C, Brouard S. Tetraspanins: useful multifunction proteins for the possible design and development of small-molecule therapeutic tools. Drug Discovery Today. 2021 Jan;26(1):56–68.

176. Functional Proteomics Screen Enables Enrichment of Distinct Cell Types from Human Pancreatic Islets. PLOS ONE. 2015 Feb 23;10(2):e0115100.

177. Li X, Yang KY, Chan VW, Leung KT, Zhang XB, Wong AS, et al. Single-Cell RNA-Seq Reveals that CD9 Is a Negative Marker of Glucose-Responsive Pancreatic β-like Cells Derived from Human Pluripotent Stem Cells. Stem Cell Reports. 2020 Nov;15(5):1111–26.

178. Quesada I, Tudurí E, Ripoll C, Nadal Á. Physiology of the pancreatic α-cell and glucagon secretion: role in glucose homeostasis and diabetes. Journal of Endocrinology. 2008 Oct;199(1):5–19.

179. Lyon JG, Carr AL, Smith NP, Marfil-Garza B, Spigelman AF, Bautista A, et al. Human research islet cell culture outcomes at the Alberta Diabetes Institute IsletCore. Islets. 2024 Dec 31;16(1):2385510.

180. Oliveros, Juan Carlos. Venny 2.1.0. [cited 2025 Sept 2]. An interactive tool for comparing lists with Venn's diagrams. Available from: https://bioinfogp.cnb.csic.es/tools/venny/

181. Zeigerer A, Sekar R, Kleinert M, Nason S, Habegger KM, Müller TD. Glucagon's Metabolic Action in Health and Disease. In: Terjung R, editor. Comprehensive Physiology [Internet]. 1st ed. Wiley; 2021 [cited 2025 Oct 15]. p. 1759–83. Available from: https://onlinelibrary.wiley.com/doi/10.1002/cphy.c200013

182. Buteau J. GLP-1 receptor signaling: effects on pancreatic β-cell proliferation and survival. Diabetes & Metabolism. 2008 Feb;34:S73–7.

183. Marzook A, Tomas A, Jones B. The Interplay of Glucagon-Like Peptide-1 Receptor Trafficking and Signalling in Pancreatic Beta Cells. Front Endocrinol. 2021 May 10;12:678055.

184. Leibiger B, Moede T, Muhandiramlage TP, Kaiser D, Sanchez PV, Leibiger IB, et al. Glucagon regulates its own synthesis by autocrine signaling. Proc Natl Acad Sci USA. 2012 Dec 18;109(51):20925–30.

185. Castell AL, Goubault C, Ethier M, Fergusson G, Tremblay C, Baltz M, et al. β Cell mass expansion during puberty involves serotonin signaling and determines glucose homeostasis in adulthood. JCI Insight. 2022 Nov 8;7(21):e160854.

186. Mauvais-Jarvis F, Clegg DJ, Hevener AL. The Role of Estrogens in Control of Energy Balance and Glucose Homeostasis. Endocrine Reviews. 2013 June 1;34(3):309–38.

187. Brownrigg GP, Xia YH, Chu CMJ, Wang S, Chao C, Zhang JA, et al. Sex differences in islet stress responses support female β cell resilience. Mol Metab. 2023 Jan 20;69:101678.

188. Qadir MMF, Elgamal RM, Song K, Kudtarkar P, Sakamuri SSVP, Katakam PV, et al. Sex-specific regulatory architecture of pancreatic islets from subjects with and without type 2 diabetes. EMBO J. 2024 Nov 20;43(24):6364–82.

189. Navarro G, Allard C, Xu W, Mauvais-Jarvis F. The role of androgens in metabolism, obesity, and diabetes in males and females. Obesity. 2015 Apr;23(4):713–9.

190. Harada N, Yoda Y, Yotsumoto Y, Masuda T, Takahashi Y, Katsuki T, et al. Androgen signaling expands β-cell mass in male rats and β-cell androgen receptor is degraded under high-glucose conditions. American Journal of Physiology-Endocrinology and Metabolism. 2018 Mar 1;314(3):E274–86.

191. Chan JY, Bensellam M, Lin RCY, Liang C, Lee K, Jonas J, et al. Transcriptome analysis of islets from diabetes-resistant and diabetes-prone obese mice reveals novel gene regulatory networks involved in beta-cell compensation and failure. The FASEB Journal. 2021 June;35(6):e21608.

192. Wigger L, Barovic M, Brunner AD, Marzetta F, Schöniger E, Mehl F, et al. Multi-omics profiling of living human pancreatic islet donors reveals heterogeneous beta cell trajectories towards type 2 diabetes. Nat Metab. 2021 June 28;3(7):1017–31.

193. Galvin SG, Kay RG, Foreman R, Larraufie P, Meek CL, Biggs E, et al. The Human and Mouse Islet Peptidome: Effects of Obesity and Type 2 Diabetes, and Assessment of Intraislet Production of Glucagon-like Peptide-1. J Proteome Res. 2021 Sept 3;20(9):4507–17.

194. Ng XW, Chung YH, Piston DW. Intercellular Communication in the Islet of Langerhans in Health and Disease. Comprehensive Physiology. 2021 June 30;11(3):2191–225.

195. Morriseau TS, Doucette CA, Dolinsky VW. More than meets the islet: aligning nutrient and paracrine inputs with hormone secretion in health and disease. American Journal of Physiology-Endocrinology and Metabolism. 2022 May 1;322(5):E446–63.

196. Tornehave D, Kristensen P, Rømer J, Knudsen LB, Heller RS. Expression of the GLP-1 Receptor in Mouse, Rat, and Human Pancreas. J Histochem Cytochem. 2008 Sept 1;56(9):841–51.

197. Kapodistria K, Tsilibary EP, Kotsopoulou E, Moustardas P, Kitsiou P. Liraglutide, a human glucagon-like peptide-1 analogue, stimulates AKT-dependent survival signalling and inhibits pancreatic β-cell apoptosis. Journal of Cellular and Molecular Medicine. 2018;22(6):2970–80.

198. Friedrichsen BN, Neubauer N, Lee YC, Gram VK, Blume N, Petersen JS, et al. Stimulation of pancreatic β-cell replication by incretins involves transcriptional induction of cyclin D1 via multiple signalling pathways. Journal of Endocrinology. 2006 Mar 1;188(3):481–92.

199. Lee YS, Lee C, Choung JS, Jung HS, Jun HS. Glucagon-Like Peptide 1 Increases b-Cell Regeneration by Promoting a- to b-Cell Transdifferentiation. 2018;67.

200. Thorel F, Népote V, Avril I, Kohno K, Desgraz R, Chera S, et al. Conversion of adult pancreatic alpha-cells to beta-cells after extreme beta-cell loss. Nature. 2010 Apr 22;464(7292):1149–54.

201. Baggio LL, Drucker DJ. Biology of incretins: GLP-1 and GIP. Gastroenterology. 2007 May;132(6):2131–57.

202. Campbell SA, Johnson J, Light PE. Evidence for the existence and potential roles of intra-islet glucagon-like peptide-1. Islets. 13(1–2):32–50.

203. Ho KH, Barmaver SN, Hu R, Yagan M, Ahmed HK, Kaverina I, et al. Pancreatic islet α cells regulate microtubule stability in neighboring β cells to tune insulin secretion and induce functional heterogeneity in individual mouse and human islets [Internet]. bioRxiv; 2024 [cited 2024 Nov 18]. p. 2024.10.21.619544. Available from: https://www.biorxiv.org/content/10.1101/2024.10.21.619544v1

204. Bracey KM, Gu G, Kaverina I. Microtubules in Pancreatic β Cells: Convoluted Roadways Toward Precision. Front Cell Dev Biol [Internet]. 2022 July 8 [cited 2025 May 18];10. Available from:

https://www.frontiersin.org/journals/cell-and-developmental-biology/articles/10.3389/fcell.2022.915206/full

205. Trogden KP, Lee J, Bracey KM, Ho KH, McKinney H, Zhu X, et al. Microtubules regulate pancreatic β-cell heterogeneity via spatiotemporal control of insulin secretion hot spots. Zaidi M, Barton M, Hodson DJ, Bogan JS, editors. eLife. 2021 Nov 16;10:e59912.

206. Wieland FC, Sthijns MMJPE, Geuens T, Van Blitterswijk CA, Lapointe VLS. The Role of Alpha Cells in the Self-Assembly of Bioengineered Islets. Tissue Engineering - Part A. 2021 Aug;27(15–16):1055–63.

207. Ast J, Nasteska D, Fine NHF, Nieves DJ, Koszegi Z, Lanoiselée Y, et al. Revealing the tissue-level complexity of endogenous glucagon-like peptide-1 receptor expression and signaling. Nat Commun. 2023 Jan 18;14(1):301.

208. Thiel G, Rössler OG. Glucose Homeostasis and Pancreatic Islet Size Are Regulated by the Transcription Factors Elk-1 and Egr-1 and the Protein Phosphatase Calcineurin. Int J Mol Sci. 2023 Jan 3;24(1):815.

209. Campbell JE, Newgard CB. Mechanisms controlling pancreatic islet cell function in insulin secretion. Nature Reviews Molecular Cell Biology. 2021 Feb;22(2):142–58.

210. Bosco D, Armanet M, Morel P, Niclauss N, Sgroi A, Muller YD, et al. Unique Arrangement of _-and ␣-Cells in Human Islets of Langerhans.

211. Cabrera O, Berman DM, Kenyon NS, Ricordi C, Berggren PO, Caicedo A. The unique cytoarchitecture of human pancreatic islets has implications for islet cell function. Proceedings of the National Academy of Sciences of the United States of America. 2006 Feb;103(7):2334–9.

212. Aamodt KI, Powers AC. Signals in the pancreatic islet microenvironment influence β-cell proliferation. Diabetes, Obesity and Metabolism. 2017;19(S1):124–36.

213. Samols E, Weir GC, Bonner-Weir S. Intraislet Insulin-Glucagon-Somatostatin Relationships. In: Lefebvre PJ, editor. Glucagon II [Internet]. Berlin, Heidelberg: Springer Berlin Heidelberg; 1983. p. 133–73. Available from: https://doi.org/10.1007/978-3-642-69019-8_9

214. Dybala MP, Hara M. In Vivo and In Situ Approach to Study Islet Microcirculation: A Mini-Review. Front Endocrinol. 2021 May 10;12:602620.

215. Lehmann R, Zuellig RA, Kugelmeier P, Baenninger PB, Moritz W, Perren A, et al. Superiority of small islets in human islet transplantation. Diabetes. 2007 Mar;56(3):594–603.

216. Abdelli S, Ansite J, Roduit R, Borsello T, Matsumoto I, Sawada T, et al. Intracellular Stress Signaling Pathways Activated During Human Islet Preparation and Following Acute Cytokine Exposure. Diabetes. 2004 Dec 1;53:2815–23.

217. Zheng Z, Zong Y, Ma Y, Tian Y, Pang Y, Zhang C, et al. Glucagon-like peptide-1 receptor: mechanisms and advances in therapy. Sig Transduct Target Ther. 2024 Sept 18;9(1):1–29.

218. Efrat S. Ex-vivo Expansion of Adult Human Pancreatic Beta-Cells. Rev Diabet Stud. 2008;5(2):116–22.

219. Green AD, Vasu S, Moffett RC, Flatt PR. Co-culture of clonal beta cells with GLP-1 and glucagon-secreting cell line impacts on beta cell insulin secretion, proliferation and susceptibility to cytotoxins. Biochimie. 2016 June;125:119–25.

220. Tong JCL, Frazer-Morris C, Shilleh AH, Viloria K, de Bray A, Nair AM, et al. Localized GLP1 receptor pre-internalization directs pancreatic alpha cell to beta cell communication. Cell Metab. 2025 Aug 5;37(8):1698-1714.e5.

221. Müller TD, Finan B, Bloom SR, D'Alessio D, Drucker DJ, Flatt PR, et al. Glucagon-like peptide 1 (GLP-1). Mol Metab. 2019 Sept 30;30:72–130.

222. Wang YJ, Golson ML, Schug J, Traum D, Liu C, Vivek K, et al. Single-Cell Mass Cytometry Analysis of the Human Endocrine Pancreas. Cell Metab. 2016 Oct 11;24(4):616–26.

Appendix

Appendix Table S 1: Donor clinical parameters. All donors are identified by donor ID, 8 digits for IIDP-derived donors and R-XXX (3 digits) for ADI-derived donors. Donors are grouped by sex (with 17 of each gender). Additionally, donor age, BMI, and % A1C are listed. Percent β-cells, α-cells, and δ-cells represent the cell percentage yield post-FACS. Donors listed as N/A were not sorted, and only native islets were used in experiments.

Donor ID	Gender	Type	Age	BMI	% A1C	% β-cells	% α-cells	% δ-cells
36823227	Female	No Disease (ND)	41	38.2	5.2	17.34	1.48	3.26
37350251	Female	ND	53	29.9	5.2	N/A*	N/A	N/A
$R525_{ADI}$	Female	ND	51	47.8	6.5	N/A	N/A	N/A
40709610	Female	ND	55	28.6	5.7	N/A	N/A	N/A
39980165	Female	ND	60	29.6	6.2	23.3	5.8	1.93
40992344	Female	ND	42	33.3	5.5	N/A	N/A	N/A
44337332	Female	ND	31	16.3	6	8.66	8.47	2.7
43583143	Female	ND	19	22.3	6	6.98	0.95	8.33
43463703	Female	ND	54	28.7	5.7			
$R551_{ADI}$	Female	ND	57	26	4.3	5.1	0.21	10.9
$R546_{ADI}$	Female	ND	42	29.7	5.9	18.14	8.87	3.5
$R537_{ADI}$	Female	ND	18	37.3	5.5			
$R532_{ADI}$	Female	ND	28	24.3	5.5	16.1	0.2	1.2
$R510_{ADI}$	Female	ND	53	21.3	5.9	7.29	0.42	0.77
47290391	Female	ND	54	30.9	4.7	N/A	N/A	N/A
$R552_{ADI}$	Female	ND	69	19.5	6.5	N/A	N/A	N/A
$R575_{ADI}$	Female	ND	59	43.9	6.1	N/A	N/A	N/A
39708909	Male	ND	21	38.1	5	33.6	22	1.76
38750927	Male	ND	34	24.5	5.4	12.02	27.1	3.5
36510137	Male	ND	63	32.1	6.1	N/A	N/A	N/A
$R549_{ADI}$	Male	ND	54	26.5	5.1	8.8	0.3	0.13
28501433	Male	ND	48	32.3	5.7	28	24	2
43079887	Male	ND	43	24.1	4.7	12	18	0.24

42355911	Male	ND	64	29.5	5.7	28.7	9.2	3.8
40380406	Male	ND	47	34.2	5.5	10.4	6.6	5.8
$R495_{ADI}$	Male	ND	50	33.8	5.8	7.58	0.43	2.93
43897604	Male	ND	41	27.8	5.3	0.57	0.18	0.22
42160709	Male	ND	49	26	4.8	20.13	6.47	5.85
42008301	Male	ND	36	30	5	12.6	6	4.2
41299360	Male	ND	20	24	5.1	15.5	6.3	5.7
39708909	Male	ND	21	38.1	5	12.7	12.1	4.9
37638596	Male	ND	34	27	5.5	20.1	3.6	2.1
$R501_{ADI}$	Male	ND	28	23.9	4.7	14.81	2.21	0.15
46795533	Male	ND	58	39.2	5.9	N/A	N/A	N/A

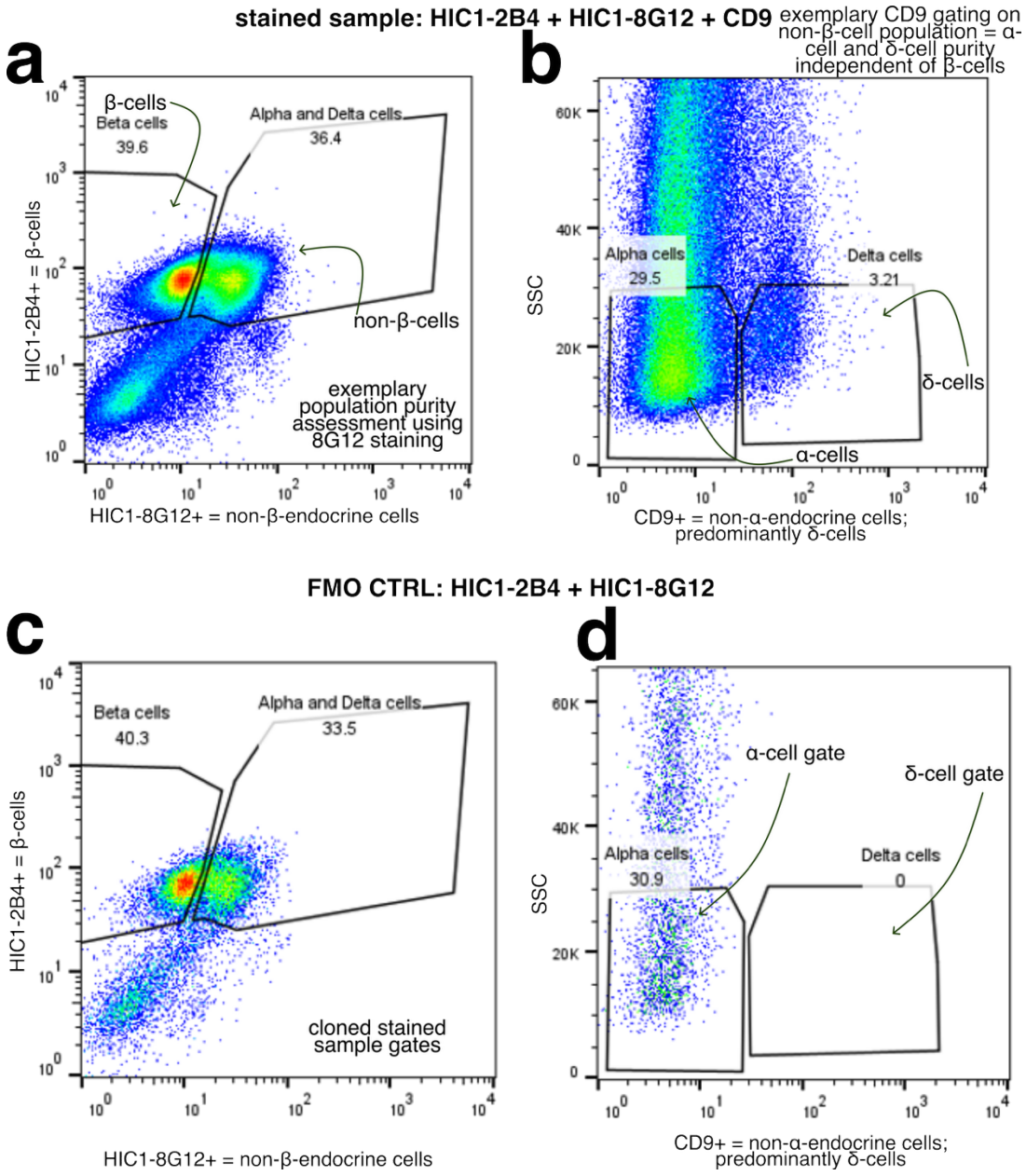

Appendix Figure 1: FACS population purity assessment overview. FACS populations are defined by staining with three antibodies. To investigate potential cross-contamination between the populations, the stained sample (all three antibodies present) was compared to the fluorescence minus one (FMO) control (no CD9 staining). (**a & b**) The stained sample was separated into endocrine and non-endocrine cells using 8G12 as the ground truth discriminator. (**a**) β-cells are defined as 2B4 + 8G12 – cells, whereas non-β-cells are 2B4 + 8G12 +. (**b**) To further subdivide the non-β-cells into α-cells and δ-cells, side scatter (SSC) (y-axis) vs. CD9 (x-axis) was used. (**c & d**) 2B4 + gates were cloned from the stained sample to the FMO sample, visualizing the endocrine vs. non-endocrine distribution in that sample (**c**). (**d**) Using the same gates and axis from (b) on the FMO shows the absence of δ-cells (CD9+).

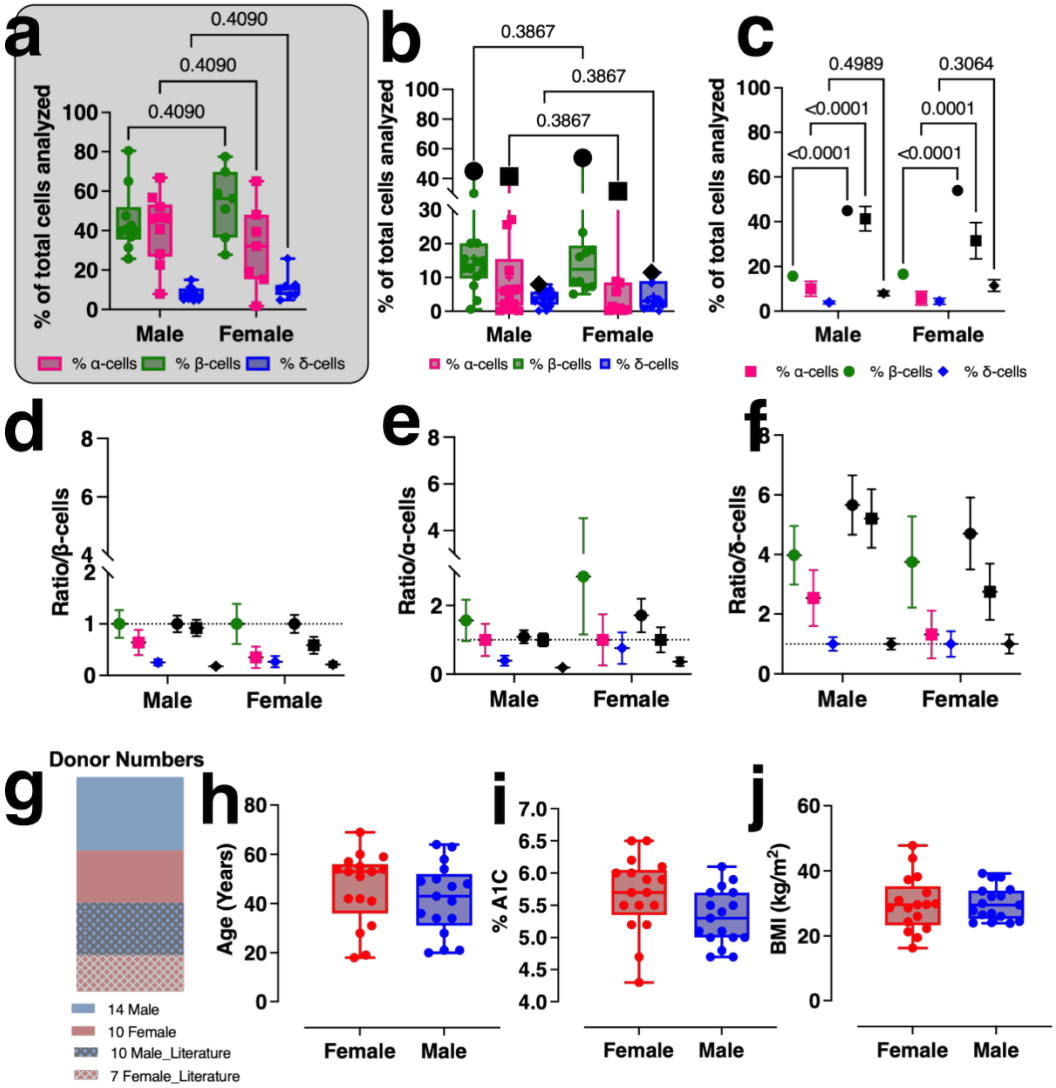

Appendix Figure 2: Comparison of this study's FACS results with available literature.

(**a**) adapted from Wang et al., visualizing % of α-cells (pink), β-cells (green), and δ-cells (blue) of total endocrine cells analyzed by single cell mass cytometry (cyTOF) for both male and female healthy donors. (**b**) Percentage of α-cells (pink), β-cells (green), and δ-cells (blue) of total cells analyzed by FACS in the present study. The mean literature value for each cell type is depicted in black. (**c**) Percentage of α-cells (pink), β-cells (green), and δ-cells (blue) for all cells analyzed by FACS vs. cyTOF (literature). Literature values follow the same symbol association but are labeled black. (**d-f**) Ratio of cells expressed as /β-cells (**d**), /α-cells (**e**), and /δ-cells (**f**) for healthy male and female donors evaluated in this study, and in comparison to literature results (following the same shape association but colored black). (**g**) Pie chart of the number of healthy male (blue) and female (orange) donors analyzed. Literature-derived donors follow the same color coding but are patterned. (**h-j**) Distribution of age, A1c, and BMI, respectively, for female (red) and male (blue) donors. Statistical analysis was done by two-way ANOVA with a Benjamini-Hochberg correction for multiple comparisons. P-values are indicated for each comparison; $p < 0.05$ was considered the cutoff for statistical significance. Error bars represent the SEM.

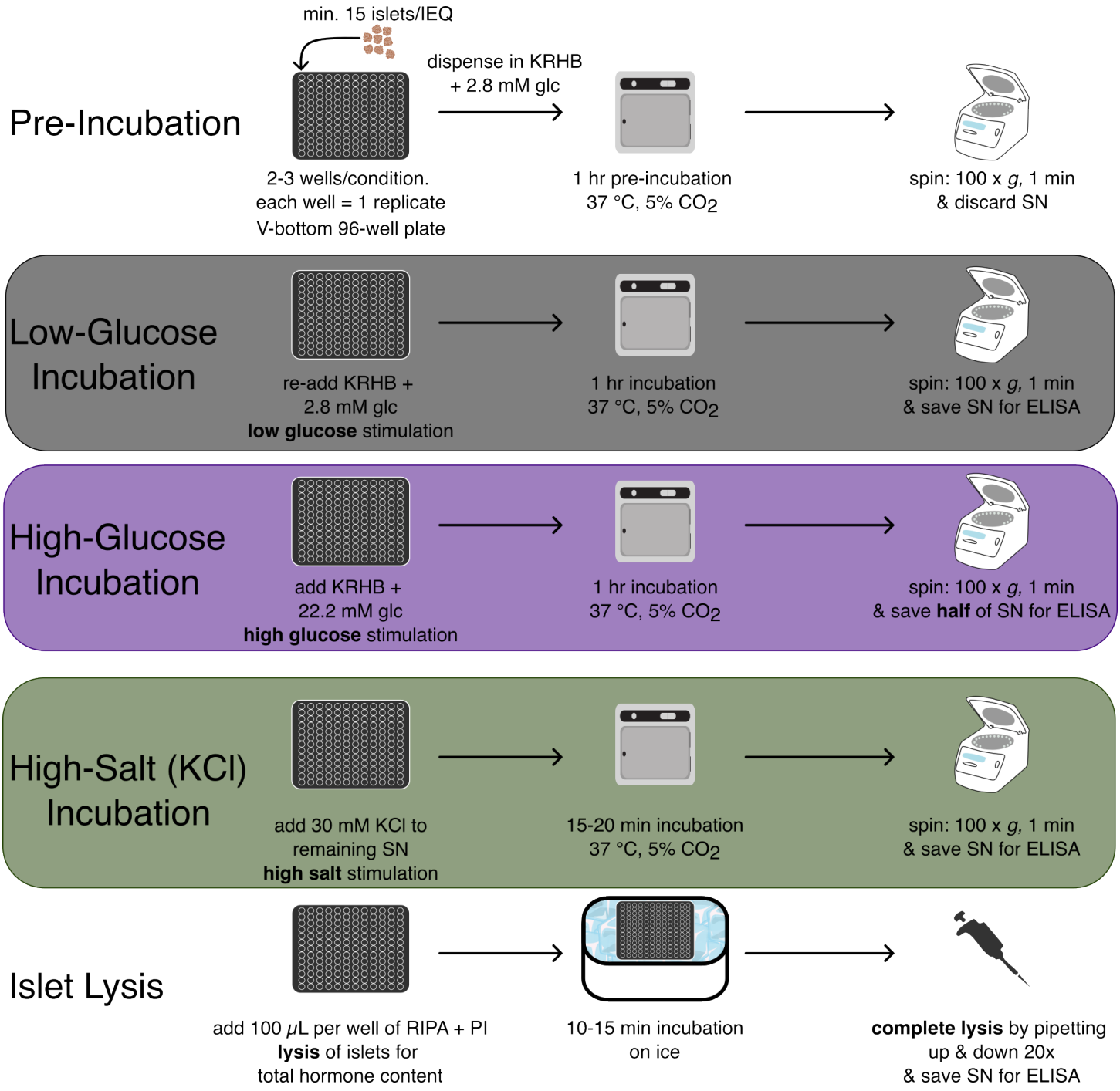

Appendix Figure 3: Overview of the glucose-stimulated hormone secretion (GSHS) assay workflow.

To evaluate native and pseudo-islet functionality, a minimum of 15 islet equivalents (IEQ) per sample were manually picked and transferred to a V-bottom 96-well plate. The conical well shape facilitated gentle handling by allowing islets to settle at the bottom, minimizing loss during wash and buffer exchange steps. Each condition was assessed in 2–3 technical replicates. Following transfer, islets were pre-incubated for 1 hour in Krebs-Ringer HEPES buffer (KRHB) containing 2.8 mM glucose to equilibrate to the assay environment. After pre-incubation, plates were centrifuged (1 min, 100 × g), and the supernatant (SN) was discarded. The assay was then carried out in three sequential stimulation steps: 1) Low-glucose stimulation (black panel): Islets were incubated in KRHB + 2.8 mM glucose for 1 hour at 37 °C and 5% CO_2. After centrifugation, the SN was collected for ELISA. 2) High-glucose stimulation (purple panel): Islets were then incubated in KRHB + 22.2 mM glucose under the same conditions. After 1 hour, half the SN was collected for ELISA. 3) High-potassium depolarization (green panel): KCl was added to the remaining SN to a final concentration of 30 mM. Islets were incubated for an additional 15–20 minutes at 37 °C, then spun down, and the SN was collected. To assess total hormone content, islets were lysed in RIPA buffer supplemented with protease inhibitor cocktail (PI) on ice for 10–15 minutes. Lysis was completed by pipetting up and down 20 times. The resulting lysate was saved for total hormone content ELISA analysis. All supernatant and lysate samples were stored at 4 °C and processed within 7 days using PROMEGA Lumit ELISA kits for insulin and glucagon.

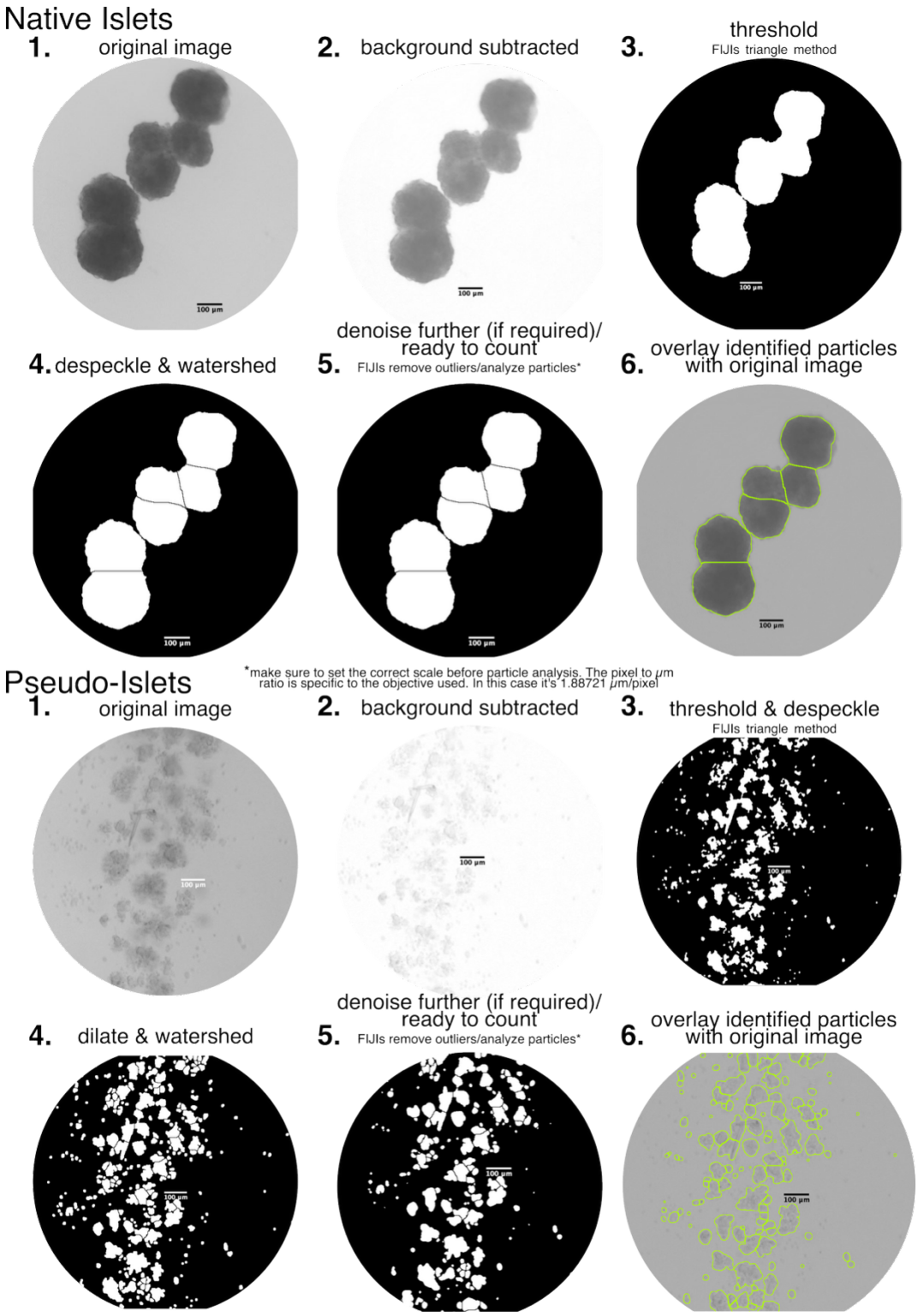

Appendix Figure 4: Step-by-step image analysis pipeline in FIJI to quantify native and pseudo-islets.

Native and pseudo-islets were cultured in ultra-low attachment 6-well plates and imaged using a Keyence EPI fluorescence microscope. 1) Original image: Brightfield images capturing the entire well. 2) Background subtraction: FIJIs rolling ball algorithm was applied (radius = 100 px for native islets; 20 px for pseudo-islets) to enhance contrast. 3) Thresholding and despeckling: The Triangle method was used for thresholding, followed by despeckling to reduce background noise. 4) Preprocessing for segmentation: “watershed” was used to separate adjacent native islets. For pseudo-islets, a “dilate” step preceded “watershed” to close internal gaps. 5) Denoising and particle analysis: Outliers were removed, and particle analysis was performed after image scale calibration to count and measure islet-like structures. 6) Validation via overlay: Detected particles were overlaid on the original image to confirm accurate segmentation. Zoomed-in views are shown with a 100 μm scale bar for reference.

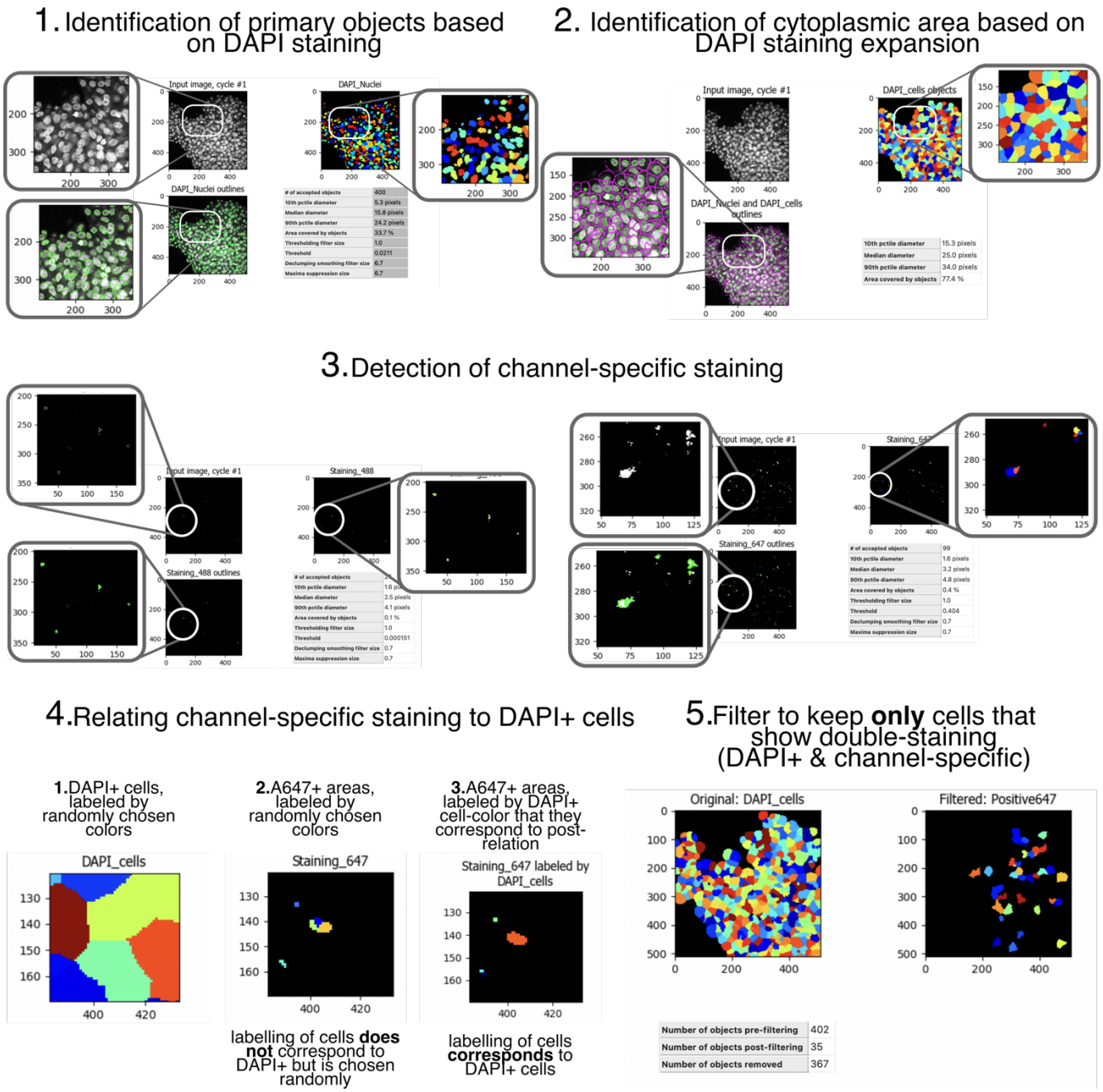

Appendix Figure 5: Overview of the CellProfiler pipeline used to quantify GCGR and GLP-1R expressing cells in native and pseudo-islets.

To assess GCGR and GLP-1R expression in human donor-derived native and pseudo-islets, islets were PFA-fixed and immunostained for insulin (559 nm), glucagon receptor (GCGR, 488 nm), and GLP-1 receptor (GLP-1R, 647 nm). Nuclei were stained with DAPI (405 nm). Confocal z-stack images were acquired using a 60× oil objective to capture the 3D structure of each islet. Pre-processing: Images were pre-processed in FIJI. This included channel splitting and brightness/contrast adjustment to match the DAPI channel. For each islet, every 2nd or 3rd plane from the z-stack (depending on islet size) was selected. Grayscale images were saved for each z-plane and for each color combination: 405+488+559, 405+488+647, and 405+559+647. CellProfiler analysis steps: 1) Primary object identification: Nuclei were identified using the DAPI (405 nm) channel staining. 2) Cytoplasmic expansion: A cytoplasmic area was approximated by expanding each nucleus by 15 pixels. 3) Channel-Specific Signal detection: Receptor-specific signal (*e.g.,* 488 nm for GCGR, 559 nm for insulin, and 647 nm for GLP-1R) was detected in the corresponding channels. Examples are shown for 488 nm and 647 nm. 4) Relating objects: Staining-positive areas were mapped to DAPI+ nuclei to assign expression to individual cells. 5) Filtering: Only cells with both a DAPI+ nucleus and detectable receptor signal were retained for analysis; all unmatched objects were excluded. Each color combination was analyzed using a dedicated CellProfiler pipeline. Cell detection was visually verified before steps 3–5 to ensure accurate segmentation and signal attribution.